

MARTIN MERANER

A PHOTONIC QUANTUM INTERFACE BETWEEN  
TRAPPED IONS AND THE TELECOM C-BAND



A PHOTONIC QUANTUM INTERFACE BETWEEN TRAPPED IONS  
AND THE TELECOM C-BAND

MARTIN MERANER

Thesis submitted to the  
Fakultät für Mathematik, Informatik und Physik  
of the Leopold-Franzens-Universität Innsbruck  
in partial fulfillment of the requirements for the degree of

Doctor of Philosophy  
(Physics)

Carried out under supervision of o. Univ.-Prof. Dr. Rainer Blatt  
and Ass. Prof. Dr. Benjamin P. Lanyon  
at the Institut für Quantenoptik und Quanteninformation - öAW , Innsbruck

05 2022

Martin Meraner: *A photonic quantum interface between trapped ions and the telecom C-band*, © 05 2022

*Those who are not shocked when they first come across  
quantum theory cannot possibly have understood it.*

Niels Bohr



## ABSTRACT

---

There is currently a world-wide research initiative to develop light-matter quantum networks. Such networks consist of distributed matter-based nodes which are linked up with light and would offer powerful approaches to computing, sensing and communicating. Using light travelling in optical fibres to link up quantum matter would be an effective way to realise intercity-scale quantum networks. Optical fibres have the lowest transmission losses at the telecom C-band centre wavelength of 1550 nm, making this the optimum wavelength for photons in long-distance quantum networks. However, most matter-based systems do not interact directly with telecom photons.

In this thesis I present the development, characterisation and application of a telecom C-band interface for one of the most powerful examples of quantum matter: trapped ionized atoms. Specifically, the interface converts 854 nm photons from the  $^{40}\text{Ca}^+$  ion to 1550 nm, via the process of optical difference frequency generation in waveguide-integrated LiNb crystals.

As a key result I show that entanglement between a trapped ion and an emitted photon is preserved both through the telecom conversion process and the subsequent distribution of the photon over 100 km of optical fibre: orders of magnitude further than the previous state of the art for matter-photon entanglement. The presented results are an important step towards the realisation of light-matter quantum networks on the inter-city scale.

## ZUSAMMENFASSUNG

---

Derzeit gibt es eine weltweite Forschungsinitiative zur Entwicklung von Quantennetzwerken mithilfe von Licht und Materie. Diese Netzwerke bestehen verteilten Knoten aus Materie, die mit Licht verbunden werden und würden leistungsstarke Ansätze für das Rechnen, Erfassen und Kommunizieren bieten. Die Verbindung von Quantenmaterie mit Hilfe von Licht in Glasfaserleitungen wäre ein wirksamer Weg zur Realisierung von Quantennetzen in innerstädtischen Größenordnungen. Optische Fasern haben die geringsten Übertragungsverluste bei einer Wellenlänge von 1550 nm, welche inmitten des optischen C-Bandes der Telekommunikation liegt. Über große Entfernungen ist dies somit die optimale Wellenlänge für Photonen in Quantennetzen. Die meisten auf Materie basierenden Systeme interagieren jedoch nicht direkt mit Photonen im Telekommunikationsband.

In dieser Arbeit stelle ich die Entwicklung, Charakterisierung und Anwendung einer Schnittstelle zwischen dem C-Band der Telekommunikation und einem der vielversprechendsten Systeme für Quantenmaterie vor: gefangene ionisierte Atome. Diese Schnittstelle wandelt 854 nm Photonen des  $^{40}\text{Ca}^+$  Ions in 1550 nm Photonen mithilfe der optischen Differenzfrequenzerzeugung in wellenleiterintegrierten LiNb-Kristallen um.

Als Schlüsselergebnis zeige ich, dass die Verschränkung zwischen einem gefangenen Ion und einem emittierten Photon sowohl durch die Frequenzkonvertierung zum C-Band, als auch durch den anschließenden Transfer des Photons über 100 km Glasfaserleitung erhalten bleibt. Diese Distanz übersteigt den bisherige Stand der Technik für Materie-Photonen-Verschränkung um Größenordnungen. Die in dieser Arbeit präsentierten Ergebnisse sind wichtig für die Realisierung von Quantennetzwerken zwischen Licht und Materie im innerstädtischen Maßstab.

## PUBLICATIONS

---

Publications relevant to the Thesis:

- V. Krutyanskiy, **M. Meraner**, J. Schupp, and B. P. Lanyon. "Polarisation-preserving photon frequency conversion from a trapped-ion-compatible wavelength to the telecom C-band." In: *Applied Physics B* 123.9 (2017), p. 228. DOI: [10.1007/s00340-017-6806-8](https://doi.org/10.1007/s00340-017-6806-8).
- **M. Meraner\***, A. Mazloom\*, V. Krutyanskiy\*, V. Krcmarsky, J. Schupp, D. A. Fioretto, P. Sekatski, T. E. Northup, N. Sangouard, and B. P. Lanyon. "Indistinguishable photons from a trapped-ion quantum network node." In: *Phys. Rev. A* 102.5 (2020), p. 052614. DOI: [10.1103/PhysRevA.102.052614](https://doi.org/10.1103/PhysRevA.102.052614).
- V. Krutyanskiy\*, **M. Meraner\***, J. Schupp\*, V. Krcmarsky, H. Hainzer, and B. P. Lanyon. "Light-matter entanglement over 50 km of optical fibre." In: *npj Quantum Information* 5.1 (2019), p. 72. DOI: [10.1038/s41534-019-0186-3](https://doi.org/10.1038/s41534-019-0186-3).
- J. Schupp, V. Krcmarsky, V. Krutyanskiy, **M. Meraner**, T. E. Northup, and B. Lanyon. "Interface between Trapped-Ion Qubits and Traveling Photons with Close-to-Optimal Efficiency." In: *PRX Quantum* 2.2 (2021), p. 020331. DOI: [10.1103/PRXQuantum](https://doi.org/10.1103/PRXQuantum).

\* These authors contributed equally



## ACKNOWLEDGEMENTS

---

I could only manage this work in cooperation with many different people. Therefore, in the following I would like to express my gratitude to all professors, colleagues, friends and relatives who have supported me with their help, effort and patience.

First of all, I want to thank Rainer, who gave me the opportunity to carry out my doctoral studies in his working group. Big thanks to my supervisor Ben, who gave me the big opportunity to work in his team and develop a new experiment. Here I also want to thank the whole Team, which worked from the beginning together with me on this experiment: Josef, Viktor, and Vojta. It was both an amazing but also sometimes a hard time together. I also want to thank all newer experimental team members for their help.

I not only received help from members of the small experimental team but also from the big ion-trapping group led by Rainer. I had fruitful discussions with nearly all members of this group especially at group events like the BBQ or the group retreat in Obergurgl. As a representative of this group I want to thank again Rainer and Thomas Monz, who are the glue of this group, which sticks all group members better together.

Also I received a lot of help outside of the Blatt-group like from the photonic team or from Gerhard Kirchmair personally. As an example I want to mention our card playing group, which made my lunch breaks unforgettable. Big thanks to the "Königsrufer" Lukas, Axl, Klemens (all Blatt), Marian (Ultracold) and Arne (Angewandte). I hope, we will continue this tradition even when all of us finally finish their studies.

Alle Wissenschaftler wären aufgeschmissen ohne die Hilfe von allen administrativen und technischen Mitarbeitern. In meinem Fall hatte ich wirklich viele helfende Hände und ich möchte mich besonders bei Patricia Moser (UIBK) und Elisabeth (IQOQI) bedanken. Danke an Wolfgang Kratz (RIP), Wolfgang Kuen (beide UIBK) und Gerhard Hendl (IQOQI), die mir bei allen Fragen zur Elektrik geholfen haben. Andreas Strasser, Bernhard Öttl, Stefan Haslwanter (alle IQOQI) und Armin Sailer unterstützten mich immer tatkräftig bei mechanischen Angelegenheiten.

Zuletzt möchte ich mich bei meiner Familie bedanken. Danke an meine Eltern, Roland und Maria, die mich sowohl psychisch als auch finanziell während meiner gesamten Studienzeit unterstützt haben. Meinen Geschwistern, Marlene und Matthias, die vergebungslos versuchen, keine physikalischen Themen neben mir anzusprechen. Vielen Dank an meine Oma, Omi und Opa, der leider meine Sponson nicht mehr miterleben darf, in mir aber schon als Kind einen Wissenschaftler

gesehen hat. Danke an meinen besten Freund David Peer, der rein technisch zwar nicht wirklich zur Familie gehört, aber mich schon seit meiner Kindheit begleitet und mich sicherlich technisch geprägt hat — viel Glück für deinen PhD über Künstliche Intelligenz.

Der Letzte und auch größte Dank gilt meiner Frau Sandra, auf deren Unterstützung und Hilfe ich immer zählen konnte. Auch während schlechten und schweren Zeiten hattest du immer mindestens ein aufmerksames Ohr für mich und ich konnte immer auf deinen Rat vertrauen.

# CONTENTS

---

## I INTRODUCTION AND BACKGROUND

<b>1 Introduction</b>	<b>3</b>
1.1 Quantum networks . . . . .	3
1.2 Motivation to go to telecom-wavelengths . . . . .	4
1.3 Trapped ions as qubits . . . . .	5
1.4 Thesis description: key questions . . . . .	6
1.5 Reading guide . . . . .	7
<b>2 Background</b>	<b>9</b>
2.1 Qubits and quantum networks . . . . .	9
2.1.1 Stationary and flying qubits . . . . .	9
2.1.2 State characterization . . . . .	10
2.1.3 State reconstruction . . . . .	12
2.2 Photon conversion by difference frequency generation	14
2.2.1 Principles of nonlinear optics . . . . .	14
2.2.2 Efficiency . . . . .	16
2.2.3 Noise sources . . . . .	18
2.3 Choice of ion species and transition . . . . .	20

## II SETUP, EXPERIMENTS AND RESULTS

<b>3 Core setup and key methods</b>	<b>25</b>
3.1 Principle of the experiment . . . . .	25
3.2 Ion trap, optical cavity and vacuum chamber . . . . .	25
3.3 Conversion crystals . . . . .	29
3.4 Single photon detectors . . . . .	30
3.5 854 nm photon generation . . . . .	33
3.5.1 Single photons via a cavity-mediated Raman process . . . . .	33
3.5.2 Ion-photon entanglement via a bichromatic cavity-mediated Raman process . . . . .	34
<b>4 Polarisation-preserving photon frequency conversion</b>	<b>37</b>
4.1 Introduction . . . . .	38
4.2 Polarisation-dependent conversion scheme . . . . .	39
4.2.1 Experimental details . . . . .	39
4.2.2 Results . . . . .	41
4.3 Polarisation-preserving conversion . . . . .	47
4.3.1 Experimental details . . . . .	47
4.3.2 Results . . . . .	48
4.4 Future applications: long-distance transmission. . . . .	49
4.5 Fibre-coupled waveguides . . . . .	51

4.6	Conclusion and Discussion . . . . .	54
<b>5</b>	<b>Telecom-wavelength ion-photon entanglement</b>	<b>57</b>
5.1	Introduction . . . . .	57
5.2	Experimental details and methods . . . . .	59
5.2.1	Overview of the experimental setup . . . . .	59
5.2.2	Pulse sequence for 50 km experiment . . . . .	66
5.2.3	State characterisation . . . . .	68
5.3	Results . . . . .	69
5.3.1	Setup efficiency for the 50 km distanced entangling experiment . . . . .	69
5.3.2	Results for 50 km ion - telecom-photon entanglement . . . . .	71
5.3.3	Decoherence of the ion-qubit state . . . . .	73
5.4	Results with improved setup . . . . .	74
5.4.1	Setup improvements . . . . .	75
5.4.2	Results for ion - telecom-photon entanglement with the improved system . . . . .	75
5.4.3	Results for 100 km light-matter entanglement in the improved setup . . . . .	76
5.5	Discussion . . . . .	79
<b>6</b>	<b>Second order correlation function of converted photons</b>	<b>83</b>
6.1	Introduction . . . . .	83
6.2	Experimental setup . . . . .	85
6.3	Experimental sequence . . . . .	85
6.4	Data analysis and results . . . . .	86
6.5	Time dependant analysis of the $g^{(2)}$ function . . . . .	87
6.5.1	Contributions to $g^{(2)}(0) \neq 0$ . . . . .	88
6.5.2	Measured rates . . . . .	89
6.5.3	Comparison of the measured and modelled $g^{(2)}$ function . . . . .	90
6.6	Discussion and conclusion . . . . .	92
<b>7</b>	<b>Indistinguishability of converted photons</b>	<b>95</b>
7.1	Abstract . . . . .	95
7.2	Introduction . . . . .	96
7.3	Experimental details and model . . . . .	97
7.3.1	Summary of the theory . . . . .	97
7.3.2	Experimental setup . . . . .	98
7.3.3	Telecom delay line efficiency and added noise . . . . .	103
7.3.4	Photon generation sequence . . . . .	104
7.4	Results . . . . .	105
7.5	Discussion . . . . .	109
<b>8</b>	<b>Quantum memory</b>	<b>113</b>
8.1	Abstract . . . . .	113

8.2	Introduction and motivation . . . . .	113
8.3	Overview of the experiment . . . . .	114
8.4	Setup and new hardware . . . . .	116
8.5	Experimental sequence . . . . .	116
8.6	Results and discussion . . . . .	118
8.7	Conclusion and outlook . . . . .	122
<b>9</b>	<b>Conclusion and outlook</b>	<b>125</b>
<b>a</b>	<b>Appendix</b>	<b>129</b>
A.1	PulseBox . . . . .	129
A.2	Conditional logic boards . . . . .	129
A.3	Stanford chips layout . . . . .	133
A.4	Temperature stabilization of nonlinear crystals . . . . .	135
A.5	Indistinguishability of converted photons: Data analysis	138
	<b>Bibliography</b>	<b>141</b>



Part I

INTRODUCTION AND BACKGROUND



## INTRODUCTION

---

Earth's earliest organisms have already shared information about species, gender and intent, which is basically already communication [1]. This communication took place via chemical signals. It took millions of years of evolution until the hominids started to communicate with gestures and noises to share knowledge and information with each other. The ability to communicate led to a gradual improvement in a range of key human skills, including the coordination of hunting teams. It's not completely clear when technologies are developed that allow communication over distances longer than a voice can carry. About 8000 years ago, drums were used in Africa to communicate over several kilometres. The first indications of writing in China are estimated to be 7000 years old. The post system was developed in Persia around 500-550 BC. The first optical telegraphs are mentioned already in the Greek tragedies *Orestia* in 458 BC [2]. In 17<sup>th</sup> century Europe, modern optical telegraphy was used for communication. The electric Morse telegraph was developed in 1774. After the telegraph, communication technology developed much faster: telephone, television, mobile phones and, in 1991, the world wide web. All of these technologies are constantly being developed to achieve faster rates of information flow.

Over the last few decades fundamentally new approaches to communication have begun to emerge out of the research field of quantum information science. In this field, information is encoded and processed in the quantum states of the physical information carriers, such as single atoms, photons or macroscopic oscillating currents in superconducting circuits. Quantum information offers fundamentally new possibilities for communication. The field of quantum information science is currently working on the development of a new type of information network, the so-called quantum network [3-5]. Such a quantum network can be used, as described in [6], for distributed sensing, timekeeping, cryptography or scaling up quantum computers. Quantum information has the potential for another revolution in communications technology via the realisation of quantum networks.

### 1.1 QUANTUM NETWORKS

A network is a set of nodes that are interconnected via links through which information can be transmitted. In a 'classical' network the nodes are used for the storage and processing of classical information, which is typically encoded into digital bits. The links enable the trans-

mission of bits of information between the nodes. Popular examples for classical networks are the global internet or local area networks (LANs), in which classical computers are connected with laser light in optical fibres. In *quantum networks* the nodes are used for the storage and processing of quantum information in *quantum bits (qubits)* encoded into quantum matter such as arrays of single atoms. The links in quantum networks are for transmitting information encoded into flying qubits, like photons travelling in optical fibres. In his paper ‘The quantum internet’ [3] H. J. Kimble describes the tools required for the realization of light-matter quantum networks. For example, to connect matter qubits in the nodes with flying qubits, quantum interconnects are required, which convert quantum states from matter to light and vice versa. Quantum networks have a myriad of known applications in a wide range of fields, many of which are being actively developed over distances from the meter scale for scalable quantum computing [7] to the global scale [6, 8].

One key functionality of a quantum network is the distribution of entanglement between its nodes. Before the start of my PhD, entanglement between two atoms in traps a few ten meters apart had been achieved with 780 nm photons [9], between two ions in traps a few meters apart with 369.5 nm photons [10] and between two nitrogen-vacancy centres 1.3 km apart with 637 nm photons [11]. During my PhD three NV-centres were entangled in a three-node network spaced over a few meters [12]. For all of those experiments, the photons are sent over optical fibres. Those key results in light-matter quantum networking set the context for my thesis: entanglement between matter has been achieved over up to 1 km. For trapped ions, entanglement has been achieved over a few meters.

## 1.2 MOTIVATION TO GO TO TELECOM-WAVELENGTHS

Using optical fibres as links in quantum networks is a powerful approach to realising land-based light-matter quantum networks across cities and between them. Such fibre-based networks could be complemented in future with free-space satellite links [13]. The attenuation in optical fibres at the wavelengths of photons used in the landmark quantum networking experiments referenced immediately above (780 nm, 637 nm, 369.5 nm) limit internode distances in quantum networks to a few km at most. For example, the current best optical fibres for 780 nm have an attenuation of  $\sim 3$  dB/km, which would result in a transmission of 1% after 7 km. It would be far better to use photons at 1550 nm (inside the telecom C-band), which suffer minimal loss in optical fibre of  $\sim 0.2$  dB/km allowing for 1% transmission over 100 km. To take advantage of this low loss wavelength, one either has to develop matter based systems that naturally interact with telecom photons [14] or develop an interface to convert the photon frequency.

The technique of changing the frequency of a single photon exists and is known as quantum frequency conversion (QFC). QFC is based on a nonlinear optic process and was first demonstrated in 1961 [15]. Before the start of my PhD, QFC of photons from quantum matter to a telecom wavelength was achieved with quantum dots [16] but had not been achieved using photons from trapped atoms or ions. During the time in which the work carried out in this thesis was done, we [17] and others [18, 19] achieved it for ions and others for photons from trapped atoms [20].

Besides minimising photon loss, and the ability to exploit the existing telecom fibre network, another benefit of using telecom C-band photons for quantum communication is to establish this frequency as a standard for communication between different quantum systems. Different examples of quantum matter have different strengths which could be combined using a common photonic frequency standard to form hybrid systems with greater capabilities than the individuals alone [21]. In order to connect these different system, with different natural photonic wavelengths, either a photon conversion adapter to bridge each pairwise combination has to be developed, or every system develops an adapter to a standard like the telecom C-band.

### 1.3 TRAPPED IONS AS QUBITS

Trapped ions are particularly powerful systems to enable quantum networking and the envisioned applications. For example, a complete set of tools for deterministic universal manipulation of quantum information encoded into registers of ten or more trapped ion qubits is readily available and of a quality near fault tolerant thresholds [22–24], as required for arbitrary distance quantum networking via the quantum repeater approach [25, 26]. Key quantum networking functionalities have been demonstrated between ions over a few meters, including remote state teleportation [27] and multi-ion protocols [28]. Trapped ions are also some of the most sensitive measurement probes yet developed. For example, many ion species, including the one used in this work, contain optical atomic clock transitions and therefore entangling them over distance enables the ideas presented in [8] and [29] to be explored.

The distance over which trapped ions can be entangled using photons at the directly-compatible wavelengths is strongly limited by photon loss in optical guides. For example, the photons at 369.5 nm that were used to entangle the two remote  $^{171}\text{Yb}^+$  ions in [10] suffer a loss of approximately 50 dB/km in optical fibre. The photons at 493 nm, used to entangle two remote  $^{138}\text{Ba}^+$  ions in [30], suffer around 15 dB/km in optical fibre. The photons at 854 nm, used to entangle a  $^{40}\text{Ca}^+$  ion with a travelling photon in [31], suffer fibre losses of only

$\sim 3$  dB/km. While the 854 nm photons suffer the least, internode distances are still limited to a few kilometres at best.

#### 1.4 THESIS DESCRIPTION: KEY QUESTIONS

The principle goal of my PhD work is to develop a photonic interface that enables the quantum states of trapped atomic ions to be interfaced with the quantum states of photons at 1550 nm. The following key questions are discussed in this thesis:

1. **Efficiency.** While conversion to telecom will reduce the subsequent photon loss rate per unit length in optical fibre, the conversion process itself will inevitably introduce photon loss. With what probability does the photonic interface convert a single photon at its input to a single telecom photon at its output? What are the limits to this probability in the systems that we develop and what are the future prospects for improvement?
2. **Added noise through conversion.** The photonic interface is expected to add unwanted photons to the output mode, thereby adding noise to the information transmitted in future quantum network links. What are the added photon noise rates, what is their physical origin and what are the prospects to further reduce them?
3. **Preservation of single photon character.** To what extent does the photonic converter change the single photon character of our trapped-ion photon source? Can the single photon characteristics be fully described by the added photon noise rates?
4. **Preservation of the photonic qubit state.** The photonic interface should preserve quantum information encoded into the photon. How faithfully does the photonic interface preserve the degree(s) of freedom used to encode a qubit?
5. **Preservation of photon indistinguishability.** Key functionalities of quantum networks require photons that are indistinguishable: there is no way to tell one from another. As such, the extent to which the photonic interface introduces distinguishing information into the photons should be assessed, understood and minimised.
6. **Entanglement between telecom-photon and ion.** Can we use the photonic interface to achieve entanglement between a telecom C-Band photon and an ion? Here, the performance of both the photonic interface and that of the trapped-ion photon source are critical.
7. **Distribution of light-matter entanglement over tens of kilometres.** Can we distribute a photon, entangled with an ion, over tens

of kilometres, as potentially enabled by the telecom wavelength? The distribution of entanglement is even more challenging compared to the previous task of observing it immediately after the photonic interface. For example, the long fibre adds both significant losses, which limits the data collection rate, and can cause errors in the photonic qubit as it travels. Moreover, the qubit encoded in the ion must survive for the photon travel time over tens of kilometres. Can we observe ion-photon entanglement after tens of kilometres of optical fibre and hundreds of microseconds of photon travel time?

## 1.5 READING GUIDE

Chapter 2 presents a summary of some of the key background theories and concepts behind the experimental results in this thesis. Specifically, after briefly introducing qubits and quantum state characterisation, the relevant theory of nonlinear optics is presented and used to derive an expression for photon conversion efficiency via difference frequency generation. Finally, our choice of ion species and transition is justified.

Chapter 3 presents the core parts of our experimental setup and key experimental methods. First, a rough outline of the complete experiment is shown, followed by the description of the single building blocks: the ion trap with an integrated optical cavity, the conversion crystals and our single photon detectors. Finally, the photon generation process is described.

Chapter 4 presents our single-photon frequency converter and its characterisation using attenuated laser light. In particular, the device efficiency is characterised and the extent to which the converter preserves the polarisation of the converted photonic qubit. In Chapter 5 I present the observation of ion-photon entanglement over up to 100 km, which is the main result of this thesis.

Chapter 6 reports on a study of how well the photon converter preserves the single photon character of our trapped-ion photon source. The degree of preservation is assessed by measuring the second order correlation function of the light before and after conversion.

Chapter 7 reports on our study of the indistinguishability of our converted photons, which is assessed by a Hong-Ou-Mandel interference of two subsequently-generated photons from the same trapped ion.

Chapter 8 presents preliminary results from an ongoing project in our group in which we aim to demonstrate the key functionalities of a telecom quantum repeater node. Finally, Chapter 9 summarizes the achieved results and gives an outlook towards future experiments and suggestions for further improvements.



## BACKGROUND

In this chapter the key background theory and concepts required to understand this thesis are given. Section 2.1 describes the basics of quantum bits and quantum networks. Section 2.2 introduces nonlinear optics and derives an expression for the efficiency of single photon frequency conversion via difference frequency generation. Finally, section 2.1 explains our choice to convert 854 nm photons from trapped  $^{40}\text{Ca}^+$  to the telecom C band.

## 2.1 QUBITS AND QUANTUM NETWORKS

The smallest information unit in quantum information is the quantum bit (qubit) [32], a two-level quantum-mechanical system. The qubit can be described by two orthogonal state vectors  $|0\rangle$  and  $|1\rangle$ . These basis states are defined as

$$|0\rangle = \begin{pmatrix} 1 \\ 0 \end{pmatrix}, \quad |1\rangle = \begin{pmatrix} 0 \\ 1 \end{pmatrix}. \quad (2.1)$$

An arbitrary pure state of a qubit can be written as

$$|\psi\rangle = \cos(\theta) |0\rangle + e^{i\phi} \sin(\theta) |1\rangle, \quad (2.2)$$

with two real parameters  $\theta, \phi \in \mathbb{R}$ . Therefore, the state  $|\psi\rangle$  is normalised, meaning  $\langle\psi|\psi\rangle = 1$ , where  $\langle\psi|$  stands for the vector dual of  $|\psi\rangle$ .

## 2.1.1 Stationary and flying qubits

Quantum networks consist of remote quantum nodes that are linked together with quantum channels [3]. While quantum nodes are stationary and therefore matter based, flying photons transmit quantum information between the nodes. There are many different options for the matter-based stationary qubits, including trapped neutral atoms, superconducting circuits, atomic ensembles and trapped atomic ions [33]. In this thesis, the electronic states of trapped atomic ions are used as stationary qubits [34], specially those of  $^{40}\text{Ca}^+$  [35]. A qubit is encoded into two states of the single outer valence electron in  $^{40}\text{Ca}^+$ . Different electronic states are used to encode the qubit in different chapters of this thesis.

For flying qubits, quantum information can be stored for example in the polarization or the time bin of a single photon [36]. In this thesis, I

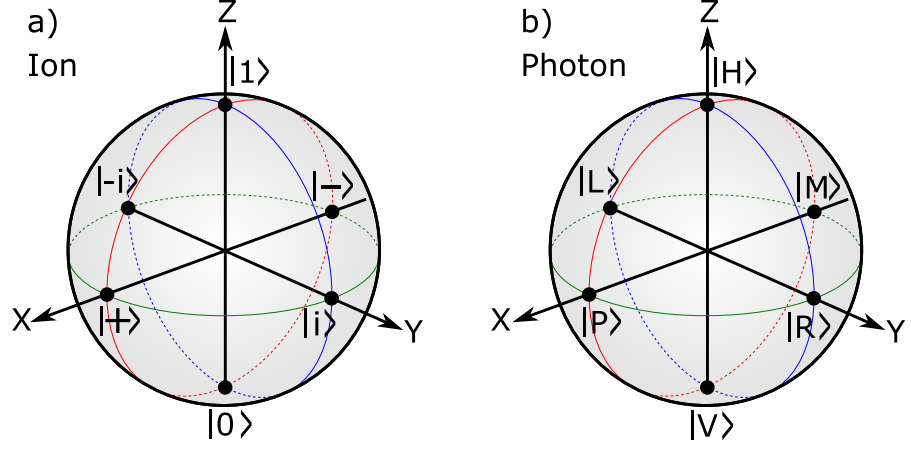


Figure 2.1: **Bloch sphere for the qubits used in the thesis:** a) A trapped-ion qubit, where the logical states  $|0\rangle$  and  $|1\rangle$  are encoded into two different electronic states of the single outer valence electron. Often a ground state  $|g\rangle$  is defined as  $|0\rangle$  and an excited state  $|e\rangle$  as  $|1\rangle$ . The logical states  $|\pm\rangle$  are defined as  $\frac{1}{\sqrt{2}}(|0\rangle \pm |1\rangle)$  and  $|\pm i\rangle = \frac{1}{\sqrt{2}}(|0\rangle \pm i|1\rangle)$ . b) The Bloch sphere and the notation used in this thesis for polarisation encoded photon qubits. This thesis uses for the diagonal  $|P\rangle = \frac{1}{\sqrt{2}}(|H\rangle + |V\rangle)$  and anti-diagonal polarization  $|M\rangle = \frac{1}{\sqrt{2}}(|H\rangle - |V\rangle)$  instead of the often used labels  $|D\rangle$  and  $|A\rangle$  in order to avoid confusion between the electronic D state of the ion and diagonally polarized photons. Right-handed circular polarization is defined as  $|R\rangle = \frac{1}{\sqrt{2}}(|H\rangle + i|V\rangle)$ , left-handed circular polarization is defined as  $|L\rangle = \frac{1}{\sqrt{2}}(|H\rangle - i|V\rangle)$ .

report on experiments where qubits are encoded into the polarisation of the photon. We define vertically-polarized photons  $|V\rangle$  as  $|0\rangle$  and horizontally-polarized photons  $|H\rangle$  as  $|1\rangle$ . For the notation used in this thesis to describe different superposition states of our trapped-ion qubits and of our photonic polarisation qubits, please see Figure 2.1.

### 2.1.2 State characterization

A more general formalism than the state vector for describing the state of an open quantum system is the density operator  $\rho$ . The density operator for the state in equation 2.2 is [32]

$$\rho_{\text{pure}} = |\psi\rangle\langle\psi| = \begin{pmatrix} \cos(\theta)^2 & e^{-i\phi} \cos(\theta) \sin(\theta) \\ e^{i\phi} \cos(\theta) \sin(\theta) & \sin(\theta)^2 \end{pmatrix}. \quad (2.3)$$

The density matrix allows for the class of states

$$\rho = \sum_i p_i |\psi_i\rangle\langle\psi_i|, \quad (2.4)$$

where the probabilities  $p_j$  are normalized ( $\sum_i p_j = 1$ ). These states include pure states (as equation 2.3, where  $p_1 = 1$ ) and mixed states ( $p_1 \neq 1$ ).

Using the Pauli operators,

$$\sigma_x = \begin{pmatrix} 0 & 1 \\ 1 & 0 \end{pmatrix}, \sigma_y = \begin{pmatrix} 0 & -i \\ i & 0 \end{pmatrix}, \sigma_z = \begin{pmatrix} 1 & 0 \\ 0 & -1 \end{pmatrix}, \quad (2.5)$$

the density matrix of a single qubit can be expand to [32]

$$\rho = \frac{1}{2}(\text{Tr}(\rho) I + \text{Tr}(\sigma_x \rho) \sigma_x + \text{Tr}(\sigma_y \rho) \sigma_y + \text{Tr}(\sigma_z \rho) \sigma_z), \quad (2.6)$$

with  $I$  the identity and  $\text{Tr}(\cdot)$  the trace operator. Note that  $\text{Tr}(\sigma_i \rho)$  is the mean value for the observable  $\sigma_i$ , thereby connecting the density matrix to the outcomes of measurements in the laboratory.

In this thesis, we characterise the density matrices that we make in the lab with the following parameters.

### *Purity*

The purity  $\gamma$  of a quantum state is defined as:

$$\gamma = \text{Tr}(\rho^2), \quad (2.7)$$

where  $0 \leq \gamma \leq 1$  is a real number. The upper bound for the purity is given by a pure state with  $\gamma = 1$  (see eq. 2.3), the lower bound for  $n$  qubits is given by  $2^{-n}$ , known as a fully mixed state. In this thesis we aim to produce pure states. Significant deviations from a pure state indicates imperfections in our experiments (see section 5.8).

### *Concurrence*

The concurrence  $C$  provides a way of quantifying how much entanglement there is in a two-qubit state [37, 38]. The concurrence is defined as

$$C(\rho) = \max\{0, \lambda_4 - \lambda_3 - \lambda_2 - \lambda_1\}, \quad (2.8)$$

where  $0 \leq C \leq 1$  with  $\lambda_i$  the square roots of the eigenvalues, in decreasing order, of the matrix product  $\rho \tilde{\rho}$ , where  $\tilde{\rho}$  is defined as  $\tilde{\rho} = (\sigma_y \otimes \sigma_y) \rho^* (\sigma_y \otimes \sigma_y)$ . Any two qubit state for which  $C > 0$  is entangled. The upper bound of the concurrence is  $C(\rho) = 1$ , which is achieved e. g. by the Bell states

$$|\Phi^\pm\rangle = \frac{1}{\sqrt{2}}(|00\rangle \pm |11\rangle) \quad (2.9)$$

$$|\Psi^\pm\rangle = \frac{1}{\sqrt{2}}(|01\rangle \pm |10\rangle). \quad (2.10)$$

### Fidelity

The fidelity  $F$  of two quantum states,  $\rho$  and  $\sigma$ , quantifies how close they are to each other [39]. The fidelity is given by

$$F(\rho, \sigma) = \left( \text{Tr} \left( \sqrt{\sqrt{\rho} \sigma \sqrt{\rho}} \right) \right)^2, \quad (2.11)$$

where  $0 \leq F \leq 1$ . The case  $F = 1$  is for identical states. The case  $F = 0$  is for orthogonal states.

#### 2.1.3 State reconstruction

As shown in equation 2.6, the density matrix can be written as a function of expectation values of the Pauli operators. Therefore, an unknown quantum state can be reconstructed by experimentally estimating the expectation values of the observables  $\sigma_x$ ,  $\sigma_y$  and  $\sigma_z$ .

Each Pauli operator can be written as a sum of projectors into its eigenstates, e. g.  $\sigma_z = |0\rangle\langle 0| - |1\rangle\langle 1|$ . Therefore, equation 2.6 equals

$$\rho = \frac{1}{2} \left( \mathbb{1} + \frac{P_+ - P_-}{P_+ + P_-} \sigma_x + \frac{P_i - P_{-i}}{P_i + P_{-i}} \sigma_y + \frac{P_1 - P_0}{P_1 + P_0} \sigma_z \right), \quad (2.12)$$

where  $P_j$  are the probabilities to measure the quantum state in the corresponding base.

The probabilities in equation 2.12 can't be measured in the lab with absolute precision, since it would require an infinite number of measurements. However, the expectation values and their uncertainties can be estimated from finite measurement results in the lab. Consider making  $N$  projective measurements of one particular observable and obtaining one specific outcome  $n_j$  times. This leads to an estimated probability  $p_j = n_j/N$  with a uncertainty  $\Delta p_j$  of

$$\Delta p_j = \sqrt{\frac{p_j(1-p_j)}{N}}. \quad (2.13)$$

In order to measure other observables, single qubit rotations can transform the measurement into the corresponding basis. Even though each probability in Equation 2.12 can be estimated, the state calculated by inverting Equation 2.12 most likely isn't a physical state, due to the finite uncertainties. The next step is to find the probabilities  $P_j$  from the measured estimation  $p_j$  with the uncertainties  $\Delta p_j$ , which corresponds to a physical state that is most likely to have produced the measured results. We use the maximum likelihood method [40] to find the most likely physical solution from the measured data.

In order to get uncertainties in the outcome, a Monte-Carlo simulation is performed. Here, multiple randomized new 'noisy' probability estimates are created from the measured probability estimates  $p_j$  using

the corresponding uncertainties  $\Delta p_j$  [41]. For each 'noisy' dataset, the maximum likelihood method finds the most likely physical state to have generated the data. Out of these multiple physical states, the desired state parameters (e. g. , purity, fidelity and concurrence) can be calculated. The standard deviation of all results is used as the measurement uncertainty.

In the work carried out in this thesis, the logical state of the ion-qubit is measured using the electron shelving technique [42, 43]. This technique allows the states  $|g\rangle$  (bright, fluorescing) and  $|e\rangle$  (dark, not fluorescing) to be distinguished, corresponding to a projective measurement in the  $\sigma_z$  basis. In order to measure the remaining two Pauli observables, single qubit rotations are performed before the electron shelving measurement. These rotations are done using a laser pulse that is resonant to the qubit transition. In comparison to the measurement of photons in this thesis, the measurement of the ion state is deterministic in the sense that either the outcome  $|0\rangle$  or  $|1\rangle$  is obtained. That is, the probability of a third outcome like 'ion is lost' or 'electron went to a third manifold' is negligible. As such, the sum of probabilities for obtaining a  $|0\rangle$  and  $|1\rangle$  outcome is 1.

For photonic polarisation qubit states, the single photons are sent on a polarising beam splitter (PBS), which transmits  $|H\rangle$  and reflects  $|V\rangle$ , which corresponds to a projective measurement in the  $\sigma_z$  basis. In order to measure the remaining two bases, single qubit rotations have to be performed on the photon. These rotations are done using a quarter- and half-waveplate before the PBS. Unlike the electron shelving technique, due to the comparatively significant probability of photon loss in optical elements, not every measurement leads to a successful experimental outcome. As such, the sum of probabilities for obtaining e. g.  $|H\rangle$  and  $|V\rangle$  outcome is not 1 but the total detection efficiency  $\nu_{\text{tot},j}$ . With two single photon detectors and knowing the total measured detection efficiencies for all projections  $\nu_{\text{tot},j}$ , the orthogonal states can be measured together. Then the estimated state probability is given by  $p_j = n_j / (N\nu_{\text{tot},j})$  with an uncertainty  $\Delta p_j$  of

$$\Delta p_j = \sqrt{\frac{p_j(1 - p_j)}{N\nu_{\text{tot},j}}}. \quad (2.14)$$

In order to reconstruct the joint state of an ion qubit and a photon qubit, different measurements have to be made in total 9 (or 18, with only one photon detector) combinations of Pauli bases. The methods described were used to reconstruct the states for the ion-photon entanglement experiments in Chapter 5 and 8.

## 2.2 PHOTON CONVERSION BY DIFFERENCE FREQUENCY GENERATION

The discovery of the second-harmonic generation (SHG) [15] is often taken as the beginning of the field of nonlinear optics. The term *nonlinear* comes from the nonlinear response of the polarization density  $\vec{P}$  to the electric field  $\vec{E}$  of the light. Unlike the linear optical response of materials to light, the nonlinear response allows for light-light interaction. Here, one light field modifies the properties of the medium, which in turn modifies the properties of the other light field (and vice versa).

Materials with optical nonlinearities allow for the generation of light fields which are different in frequency compared to the input light fields. This so called frequency conversion can be used for many applications, like creating laser light at frequencies that are difficult to obtain directly from lasers [44], or measuring light at frequencies that lie outside the bandwidth of a given detector [45]. The use of optical nonlinearities to achieve the frequency conversion of single photons ('quantum frequency conversion' QFC) was proposed by [46] and first demonstrated by [47].

In this section introduces the theory of nonlinear optics which underpins our approach for single photon frequency conversion. Section 2.2.1 details the second order nonlinearity of the dielectric polarization. Section 2.2.2 presents a model of the efficiency of single photon frequency conversion via difference frequency generation, ending with a summary of the desirable properties of a photon converter for quantum networks. The theoretical models are mainly adopted from [48–50].

### 2.2.1 Principles of nonlinear optics

Light propagating in a non-magnetic material with no free charges and no free currents can be described by the following modified Maxwell equations:

$$\nabla \cdot \vec{D} = 0 \quad (2.15)$$

$$\nabla \cdot \vec{H} = 0 \quad (2.16)$$

$$\nabla \times \vec{E} = -\frac{\partial \mu \vec{H}}{\partial t} \quad (2.17)$$

$$\nabla \times \vec{H} = \frac{\partial \vec{D}}{\partial t}, \quad (2.18)$$

with the displacement field  $\vec{D}$ , the magnetizing field  $\vec{H}$ , the electric field  $\vec{E}$  and the permeability  $\mu$ . The displacement field  $\vec{D}$  is given by

$$\vec{D} = \epsilon_0 \vec{E} + \vec{P}. \quad (2.19)$$

The polarization density (or simply polarization)  $\vec{P}$  can be expressed as a power series:

$$\begin{aligned}\vec{P} &= \epsilon_0\chi^{(1)}\vec{E} + \epsilon_0\chi^{(2)}\vec{E}^2 + \epsilon_0\chi^{(3)}\vec{E}^3 + \dots \\ &= P^{(1)} + P^{(2)} + P^{(3)} + \dots ,\end{aligned}\quad (2.20)$$

with  $\epsilon_0$  the electric constant and  $\chi^{(k)}$  the  $k^{\text{th}}$  order of the electric susceptibility. While linear optics approximate the polarization only with the first term, that is linear in the electric field, nonlinear optics refers to the other, higher-order, terms. In this thesis we are primarily concerned with the second order nonlinearity. The second order polarisation is given by

$$P^{(2)} = \epsilon_0\chi^{(2)}\vec{E}^2 . \quad (2.21)$$

For the case of two transverse electromagnetic (TEM) input laser light fields into the nonlinear material with the wave number  $k_j$ , which propagate along the  $z$ -axis, the electric field can be described as

$$\vec{E} = \vec{E}_1 e^{-i\omega_1 t} + \vec{E}_2 e^{-i\omega_2 t} + c.c. , \quad (2.22)$$

with  $E_j = A_j(z)e^{ik_j z}$ , where  $A_j(z)$  describes the amplitude of the  $j^{\text{th}}$  field along the  $z$ -axis. Substituting 2.22 into 2.21 yields

$$\begin{aligned}P^{(2)} &= \epsilon_0\chi^{(2)}[\vec{E}_1^2 e^{-2i\omega_1 t} + \vec{E}_2^2 e^{-2i\omega_2 t} + 2\vec{E}_1\vec{E}_2 e^{-i(\omega_1+\omega_2)t} \\ &\quad + 2\vec{E}_1\vec{E}_2^* e^{-i(\omega_1-\omega_2)t} + c.c.] + 2\epsilon_0\chi^{(2)}[\vec{E}_1\vec{E}_1^* + \vec{E}_2\vec{E}_2^*] .\end{aligned}\quad (2.23)$$

The complex amplitudes of the frequency components of this sum represent different types of second order polarizations:

$$P^{(2)}(2\omega_1) = \epsilon_0\chi^{(2)}\vec{E}_1^2 \quad (\text{SHG}), \quad (2.24)$$

$$P^{(2)}(2\omega_2) = \epsilon_0\chi^{(2)}\vec{E}_2^2 \quad (\text{SHG}), \quad (2.25)$$

$$P^{(2)}(\omega_1 + \omega_2) = 2\epsilon_0\chi^{(2)}\vec{E}_1\vec{E}_2 \quad (\text{SFG}), \quad (2.26)$$

$$P^{(2)}(\omega_1 - \omega_2) = 2\epsilon_0\chi^{(2)}\vec{E}_1\vec{E}_2^* \quad (\text{DFG}), \quad (2.27)$$

$$P^{(2)}(0) = 2\epsilon_0\chi^{(2)}(\vec{E}_1\vec{E}_1^* + \vec{E}_2\vec{E}_2^*) \quad (\text{OR}). \quad (2.28)$$

Where second harmonic generation (SHG) doubles the original frequency, sum frequency generation (SFG) outputs a frequency equal to the sum of the two input fields and difference frequency generation (DFG) outputs a frequency equal to the difference between the two input fields. Equation 2.28 described the process of optical rectification (OR). For the following calculations we concentrate on DFG.

## 2.2.2 Efficiency

Combining the Maxwell equations 2.17 with 2.19 leads to

$$\nabla \times \nabla \times \vec{E} + \frac{1}{c^2} \frac{\partial^2 \vec{E}}{\partial t^2} = -\frac{1}{\epsilon_0 c^2} \frac{\partial^2 \vec{P}}{\partial t^2}. \quad (2.29)$$

Next we substitute  $\vec{P}$  with the sum of the linear term  $P^{(1)} = \epsilon_0 \chi^{(1)} \vec{E}$  and the nonlinear term  $P^{(2)}$  and make the approximation<sup>1</sup>  $\nabla \times \nabla \times \vec{E} \approx -\nabla^2 \vec{E}$ , yielding

$$\nabla^2 \vec{E} - \frac{n^2}{c^2} \frac{\partial^2 \vec{E}}{\partial t^2} = \frac{1}{\epsilon_0 c^2} \frac{\partial P^{(2)}}{\partial t^2}. \quad (2.30)$$

Since DFG is a three-wave mixing process, three different light fields are involved. While the frequencies of the two input light fields  $j = 1, 2$  are free parameters, for  $j = 3$  the output frequency  $\omega_3 = \omega_1 - \omega_2$  is fixed. Using the DFG solution for  $P^{(2)}$  (Equation 2.27) and the fact that the amplitude of the output electric field vector  $A_3$  varies as a function of the position  $z$ , yields

$$\frac{d^2 A_3}{dz^2} + i2k_3 \frac{dA_3}{dz} = \frac{2\omega_3^2 \chi^{(2)}}{c^2} A_1 A_2^* e^{i(k_1 - k_2 - k_3)z}. \quad (2.31)$$

The second order electric susceptibility  $\chi^{(2)}$  is, in general a tensor that describes the electric field polarisation as a function of the direction of propagation through a material. However, in our case where the propagation and polarisation directions are fixed, we make the substitution  $\chi^{(2)} = 2d_{eff}$  where  $d_{eff}$  is a real number known as the effective nonlinear constant. Next, we use the standard 'slow varying amplitude approximation' [51]. This approximation assumes a slow variation of the electric field amplitude in space and time compared to the frequencies and wavelengths of the laser fields. Therefore, ( $|\frac{d^2 A_3}{dz^2}| \ll |k_3 \frac{dA_3}{dz}|$ ) can be assumed. Using this approximation and repeating the calculation 2.2.2 for all three waves, three coupled wave equations can be formed:

$$\begin{aligned} \frac{dA_1}{dz} &= i\gamma_1 A_2 A_3 e^{-i\Delta k z}, \\ \frac{dA_2}{dz} &= i\gamma_2 A_1 A_3^* e^{i\Delta k z}, \\ \frac{dA_3}{dz} &= i\gamma_3 A_1 A_2^* e^{i\Delta k z}, \end{aligned} \quad (2.32)$$

with  $\gamma_j = \frac{2\omega_j d_{eff}}{cn_j}$  and  $\Delta k = k_1 - k_2 - k_3$ .  $n_j$  is the refractive index and  $c$  the vacuum speed of light.

<sup>1</sup> This approximation applies, when the beams propagate along a principle axis of the crystal.

In this thesis we want to convert single photons. Therefore two fields are single photons—the single photon input and the frequency-converted single photon output—while the third field is a ‘pump’ laser field. We assign  $A_1$  for the electric field amplitude of the input single photon beam,  $A_2$  for the electric field amplitude of the pump laser and  $A_3$  for the electric field amplitude of the converted single photon beam at our target frequency. Since  $A_2 \gg A_1$ , only a minor part of the pump laser field gets converted. Therefore, we assume a constant amplitude of the pump field inside the nonlinear material, yielding

$$\frac{dA_2}{dz} = 0. \quad (2.33)$$

Let’s assume  $\Delta k = 0$ , known as phase matching. Phase matching can be approximated using the processes of quasi-phase matching, which is described in more detail in [48, 52]. With these assumptions, the equations 2.32 reduce to

$$\frac{dA_1}{dz} = -j\gamma_1 A_2^* A_3, \quad (2.34)$$

$$\frac{dA_3}{dz} = -j\gamma_3 A_1 A_2. \quad (2.35)$$

Combining these equations yields

$$\frac{d^2 A_1}{dz^2} = -\gamma_1 \gamma_3 |A_2|^2 A_3 = -K^2 \cdot A_1, \quad (2.36)$$

with  $K = \sqrt{\gamma_1 \gamma_3 |A_2|^2}$ . While two fields ( $A_1$  and  $A_2$ ) are coupled into the nonlinear material, the third field ( $A_3$ ) will be created inside the material. This leads to the boundary condition of  $A_3(0) = 0$ , meaning there is no laser field of the converted single photon beam at the input ( $z = 0$ ) of the nonlinear material. After using this boundary condition, the solution of 2.36 is

$$A_3(z) = \sqrt{\frac{\gamma_3}{\gamma_1}} e^{i\phi_2} A_1(0) \sin(Kz), \quad (2.37)$$

with  $\phi_2$  the phase between the pump laser and the single photon input.

Now we want to express these light fields in terms of a measurable value: the optical power. The optical power of the light field is defined as  $P_j = \int_F I_j dA$ , with  $F$  the mode area and  $I_j = 2n_j \epsilon_0 c |A_j|^2$  the light intensity. We define the conversion efficiency  $\eta$  of a nonlinear material with length  $L$  as the fraction of the number of converted photons  $N_3$  to the number of input photons  $N_1$  using  $N_j = P_j / \hbar \omega_j$ :

$$\eta(P_2) = \frac{N_3}{N_1} = \frac{P_3(L)}{P_1(0)} \frac{\omega_1}{\omega_3} = \sin^2(\sqrt{\eta_{nor}} P_2 L), \quad (2.38)$$

using  $\eta_{nor} = \frac{\gamma_1 \gamma_3}{2n_2 \epsilon_0 c}$ . The derivation of 2.38 has assumed perfect overlap of the optical modes in the nonlinear material. The effect of imperfect

spatial mode matching can be modelled by adding a spatial beam overlap factor ( $\nu$ ) [53], where  $0 \leq \nu \leq 1$ :

$$\eta(P_2) = \nu^2 \sin^2(\sqrt{\tilde{\eta}_{nor}} P_2 L) \quad (2.39)$$

and  $\tilde{\eta}_{nor} = \frac{\nu^2 \gamma_1 \gamma_3}{2n_2 \epsilon_0 c}$ .

Equation 2.39 shows the dependency of the conversion efficiency on the pump power  $P_2$ . The pump power required to achieve maximum conversion efficiency is

$$P_{2,\max} = \frac{\pi^2}{4L^2 \tilde{\eta}_{nor}}. \quad (2.40)$$

In Chapter 4 we experimentally measure the dependency of the conversion efficiency on the pump power and compare it to the model 2.39.

### 2.2.3 Noise sources

Single photon conversion does not only output the wanted photons from the single photon source at the target frequency, but also unwanted photons at the same target frequency. In this thesis these photons are called 'added noise photons'. Three physical processes that can produce added noise photons in single photon conversion are: spontaneous parametric down-conversion (SPDC), Stokes Raman scattering and anti-Stokes Raman scattering. Overviews of these processes are now given.

#### *Spontaneous parametric down-conversion of the pump laser*

SPDC is a nonlinear process in which one photon with higher energy (referred to as a pump photon) splits into two photons of lower energy (the signal and idler photons). Unlike the second order nonlinear conversion processes described in Section 2.2, SPDC happens with only one input light field and is stimulated by vacuum fluctuations. The pump photons split into two photons while the energy is preserved ( $\omega_1 + \omega_2 = \omega_p$ , with  $\omega_p$  the frequency of the pump laser) [54, 55]. Some experiments use SPDC to create entangled photon pairs [56, 57], while in our experiment SPDC of our strong pump laser is an unwanted effect which creates added noise photons. Together with energy preservation, SPDC also has to preserve the momentum. Ideal quasi-phase matching of a nonlinear material enhances conversion efficiency at specific wavelengths. However, imperfections in the quasi-matching (imperfect 'poling periods') has proven to produce a white noise spectrum of SPDC photons with wavelengths longer than the pump photons [58].

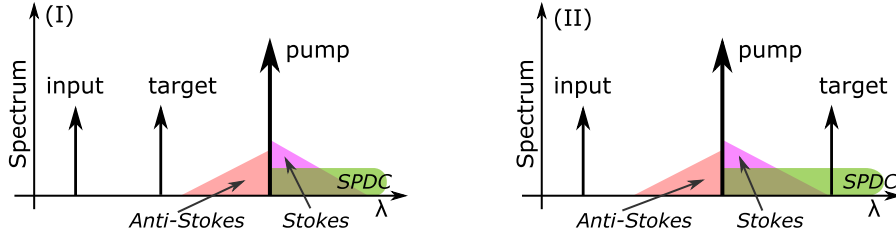


Figure 2.2: **Sketch of the noise distributions affecting difference frequency generation in two regimes. (I) The long pump wavelength regime.** Here, the pump wavelength is longer than the target wavelength. The target wavelength overlaps only with anti-Stokes Raman scattered noise from the strong pump. **(II) The short pump wavelength regime.** Here, the pump wavelength is shorter than the target wavelength. This leads to an overlap of target wavelength with SPDC noise and Stokes Raman scattering noise. While the Stokes and anti-Stokes noise goes down with higher wavelength difference to the pump, the SPDC noise stays constant over the spectra. To avoid SPDC noise within the target wavelength, the long-pump wavelength regime is used.

### *Stokes and anti-Stokes Raman scattering of the pump laser*

Raman scattering in general is inelastic scattering of photons with molecules or crystals. The photon scattering process changes the vibrational energy of the crystal and the photon energy. While for Stokes Raman scattering the photon energy decreases, a anti-Stokes Raman scattering event increases the energy of the photon.

The characteristic Raman spectrum for common nonlinear materials is a well known property [59]. Even at energy shifts greater than  $1000 \text{ cm}^{-1}$  from the input field, one still sees a measurable amount of scattered photons. In [60] the authors study this phenomena and could see Stokes scattering at the single photon level further away than expected in works before [61].

The ratio between the rate of Stokes scattered photons  $R_S$  and the rate of anti-Stokes Raman scattered photons  $R_{aS}$  follows a Boltzmann distribution [60, 62]

$$\frac{R_{aS}}{R_S} = \left( \frac{\omega_p + \Delta\omega}{\omega_p - \Delta\omega} \right)^4 e^{\frac{-\hbar\Delta\omega}{k_B T}}, \quad (2.41)$$

with  $\Delta\omega$  the Raman scattering frequency shift,  $k_B$  the Boltzmann constant and  $T$  the temperature. Equation 2.41 shows that the fraction of anti-Stokes scattering decreases exponentially as the temperature is reduced linearly.

### *Long- and short-pump wavelength regime*

We now consider the effects of the aforementioned noise processes on single photon frequency conversion via difference frequency generation. Two distinct regimes can be identified. The regime where the

pump laser has lower energy than that of the target output photon is known as the 'long pump wavelength regime'. The regime where the pump laser has higher energy than that of the target output photon is known the 'short pump wavelength regime'. As depicted in Figure 2.2, in the long-pump wavelength regime the target wavelength overlaps with anti-Stokes Raman scattered noise from the pump laser, while in the short-pump wavelength regime the target wavelength overlaps with Stokes Raman scattered and SPDC noise from the pump laser. Once concludes that the long pump wavelength regime should yield significantly lower added noise photons at the target wavelength. For single-step photon conversion to the telecom C-band wavelength of 1550 nm, long-pump wavelength conversion requires an initial input photon wavelength over 775 nm.

### 2.3 CHOICE OF ION SPECIES AND TRANSITION

This section explains why the 854 nm single photon transition in  $^{40}\text{Ca}^+$  is an excellent candidate for conversion to the telecom C-band. When selecting an ion species and internal transition suitable for telecom photon conversion we first restrict ourselves to ions species in which quantum logic has been demonstrated. Next we consider only electric dipole transitions due to their strong coupling to optical fields, in comparison to higher order transitions. Given the wavelength of the remaining candidate transitions, one can calculate the pump laser wavelength needed to convert, in a single difference frequency step, to any target wavelength.

Next, to avoid SPDC noise we restrict conversion processes to those in the long-pump wavelength regime (see Section 2.2.3). As a final, softer, restriction to our transition choice we want to keep the wavelength ratio of the input photon to the pump laser below two. We picked a ratio of 2 as an approximate cutoff, noting that the following papers [16, 63] have achieved tens of percent conversion efficiency with ratios below this value. For higher ratios we expect a reduced conversion efficiency due to difficulties in in-coupling and guiding such disparate wavelengths into the same waveguide.

Within the described constraints, Figure 2.3 shows possible frequency conversions that can be realised with trapped ions using a single step conversion process. One sees that the 854 nm transition in  $\text{Ca}^+$  is the ideal choice for conversion to 1550 nm.  $^{40}\text{Ca}^+$  is also a very good candidate for quantum computing [22, 35, 64–66] and already single photons at 854 nm where produced and these photons have been collected from this species in free space [67] and using an optical cavity [31]. Other options are possible for more than one step conversion or via four-wave mixing [68].

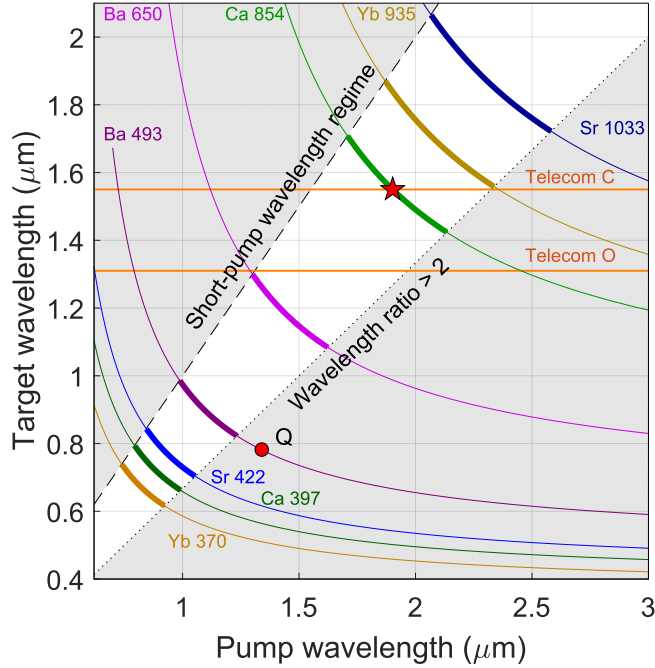


Figure 2.3: **Possible one-step three-wave mixing conversion processes for established single-photon transitions in various trapped-ion species.** The pump laser wavelength required to convert various input photon wavelengths (written in nm on the plot) to any given target photon wavelength is shown. The upper grey shaded area indicates the short-pump wavelength regime, where the target wavelength is contaminated by SPDC noise from the pump. The lower grey shaded area indicates where the ratio between the input photon wavelength and the pump laser wavelength is higher than two. This regime makes the coupling of the light fields into the conversion waveguide challenging and therefore we expect a less efficient conversion. The red star indicates the point where the 854 nm transition from  $^{40}\text{Ca}^+$  is converted to 1550 nm, the telecom C-band, using a pump laser at 1902 nm. The 935 nm transition in Yb is another candidate, although the ratio of wavelengths represents a challenge. The red dot marked with Q indicates the experiment lead by Q. Quraishi in [21], where they convert 493 nm photons from Barium to 780 nm resonant with a  $^{87}\text{Rb}$  atomic ensemble. This result was achieved in 2019, during my thesis. The end-to-end conversion efficiency of  $\sim 19\%$  was mainly limited by the coupling efficiency into the PPLN waveguide of  $\sim 30\%$ , which is consistent with our concerns of ratios above 2.



## Part II

### SETUP, EXPERIMENTS AND RESULTS



## CORE SETUP AND KEY METHODS

## 3.1 PRINCIPLE OF THE EXPERIMENT

Figure 3.1 shows the four main parts of the experimental setup used in this thesis. First, the ion-cavity system.  $^{40}\text{Ca}^+$ , trapped in a linear Paul trap and placed into the centre of a cavity is used as a single 854 nm photon source. Second, a QFC system converts the 854 nm photons to 1550 nm. For the conversion process, difference frequency generation (DFG) is used, as described theoretically in Section 2.2. Third, the converted 1550 nm photons are coupled into a fibre spool, of varying lengths. Finally, after travelling through the fibre spool, the photons are spectrally filtered and detected.

In the ongoing chapter details of each part of the setup are given. Section 3.2 presents the ion-cavity system. Section 3.5 describes the cavity-mediated Raman transition, which is used to produce photons from the ion. Details and performance of the conversion setup are shown in Section 3.3. Different filter and detector setups were used in the experiments reported in this thesis. The relevant details are given in the methods of each individual experiment. The details of all the photon detectors used in this thesis can be found in Section 3.4.

## 3.2 ION TRAP, OPTICAL CAVITY AND VACUUM CHAMBER

Our cavity-integrated ion-trap system system was designed and constructed during the time of my PhD work at the Innsbruck IQOQI building. The design is based on that of the system at the nearby University of Innsbruck that was used in [31]. The common design elements are a 20 mm long near-concentric optical cavity with a 3D linear-Paul ion trap hanging inside it. The trap is rigidly attached

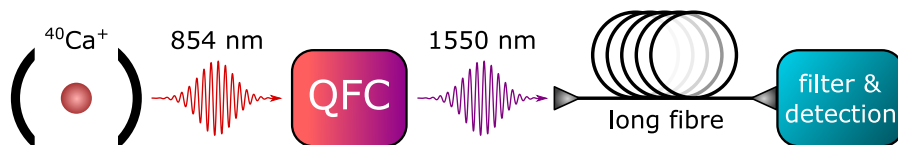


Figure 3.1: **Overview of our experimental systems for long distance light-matter entanglement:** A calcium ion, placed inside a optical cavity produces an 854 nm photon. The photon is polarisation-entangled with a qubit encoded into the electronic state of the ion. The photon is converted via quantum frequency conversion (QFC) to 1550 nm, the telecom C-band. After travelling over an optical fibre up to 100 km long, the photon gets filtered and detected.

to the top of the vacuum chamber. The cavity is attached, via translation stages, to the bottom of the vacuum chamber. Full details on the new cavity-integrated ion-trap system will be presented in the upcoming PhD theses of Josef Schupp [69] and Vojtech Krcmarsky [70]. An overview is given now.

### *Ion trap*

We use a 3D radio-frequency linear Paul trap with a DC endcap to ion separation of 2.5 mm and ion to blade minimum distance of 0.8 mm. The trap electrodes are made of titanium, coated with gold and are mounted on sapphire holders. The ion trap hangs from the top of the vacuum chamber, as shown in Figure 3.2. The ion-string axis is vertical. The trap drive frequency used for experiments in this thesis is 23.4 MHz. The radial secular frequencies are  $\omega_x \approx \omega_y = 2\pi \times 2.0$  MHz, split by approximately 10 kHz and the axial frequency is  $\omega_z = 2\pi \times 0.927$  MHz. Atoms are loaded from a resistively heated atomic oven and ionised via a two photon process involving 375 nm and 422 nm laser light. The orientations of the cavity-ion-trap system in respect to the laser light fields are shown in Figure 3.3.

### *Cavity parameters*

The cavity used for the experiments in this thesis was mainly designed and built by Josef Schupp. A detailed description on how it was built and characterized will be given in his thesis [69] and is summarised in our paper [71]. The optical cavity is near-concentric with a length  $l = 19.9057 \pm 0.0003$  mm and radii of curvature  $ROC = 9.9841 \pm 0.0007$  mm, determined from simultaneous measurements of the free spectral range (FSR) and higher-order TEM mode spacing (assuming identical mirror geometries) [69, 72]. From this we calculate an expected cavity waist of  $\omega_0 = 12.31 \pm 0.07$   $\mu\text{m}$  and a maximum ion-cavity coupling rate of  $g_{\text{max}} = 2\pi \cdot 1.53 \pm 0.01$  MHz.

The polishing of the mirror substrates was done by Perkins Precision Development, Boulder (Colorado). The coating was done by Advanced Thin Films (Boulder). The transmissions  $T_{1,2}$  of our cavity mirrors were measured [69] by applying the method described in [73], yielding  $T_1 = 2.2 \pm 0.3$  ppm,  $T_2 = 97 \pm 4$  ppm, such that the combined mirror losses from scattering and absorption  $L_{1+2} = 17 \pm 5$  ppm. At a wavelength of 854 nm, the finesse of the TEM<sub>00</sub> mode is  $\mathcal{F} = \frac{2\pi}{\mathcal{L}} = 54(1) \times 10^3$ , with the total cavity losses  $\mathcal{L} = T_1 + T_2 + L_{1+2} = 116 \pm 2$  ppm, determined from measurements of the cavity ringdown time  $\tau_C = \frac{\mathcal{F}}{\pi} \cdot \frac{l}{c_0}$ , with  $c_0$  the speed of light in vacuum. From the cavity ringdown time one can calculate the cavity linewidth  $2\kappa = 1/\tau_C = 2\pi \cdot 140 \pm 3$  kHz,  $\kappa$  being the half-width at half maximum.

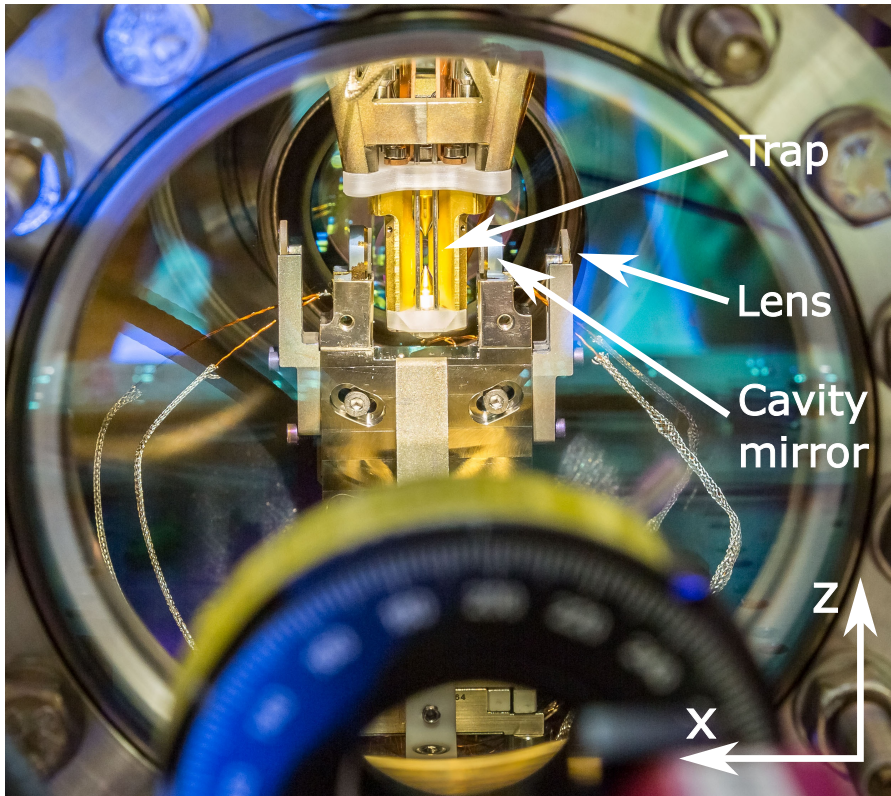


Figure 3.2: **Photograph of the cavity-ion-trap system:** The trap is hanging from the top flange of the vacuum chamber (not shown) into the centre of the two cavity mirrors. The cavity mirrors are mounted on the bottom flange of the vacuum chamber and are surrounded by two collimating lenses. This picture was shot by David Jordan.

The probability that a photon inside the cavity exits through mirror  $T_2$  (designated output mirror) is  $P_{\text{out}}^{\text{max}} = T_2 / (T_1 + T_2 + L_{1+2}) = 0.83 \pm 0.03$ .  $P_{\text{out}}^{\text{max}}$  is the maximum photon collection probability from the ion in our system (with the current mirrors). The ion-cavity system at the University has  $P_{\text{out}}^{\text{max}} = 0.16$  [31].

The cavity length is stabilised via the Pound-Drever-Hall (PDH) method [74] to a laser at 806 nm with a linewidth on the order of 1 kHz [75]. The 806 nm wavelength lies far from any transition in  $^{40}\text{Ca}^+$  to minimise AC Stark shifts on the ionic transitions. The cavity is locked to a  $\text{TEM}_{01}$  mode, allowing a single ion to be placed in the central intensity minimum to further minimise AC Stark shifts.

The cavity waist is centred on the ion via course tuning of a 3D piezo stick-slip translation-stage system (Attocube). Before experiments, photon detection efficiency is optimised by placing the ion in a cavity anti-node via fine tuning of the cavity position along its axis by applying a small bias voltage to the corresponding piezo stage.

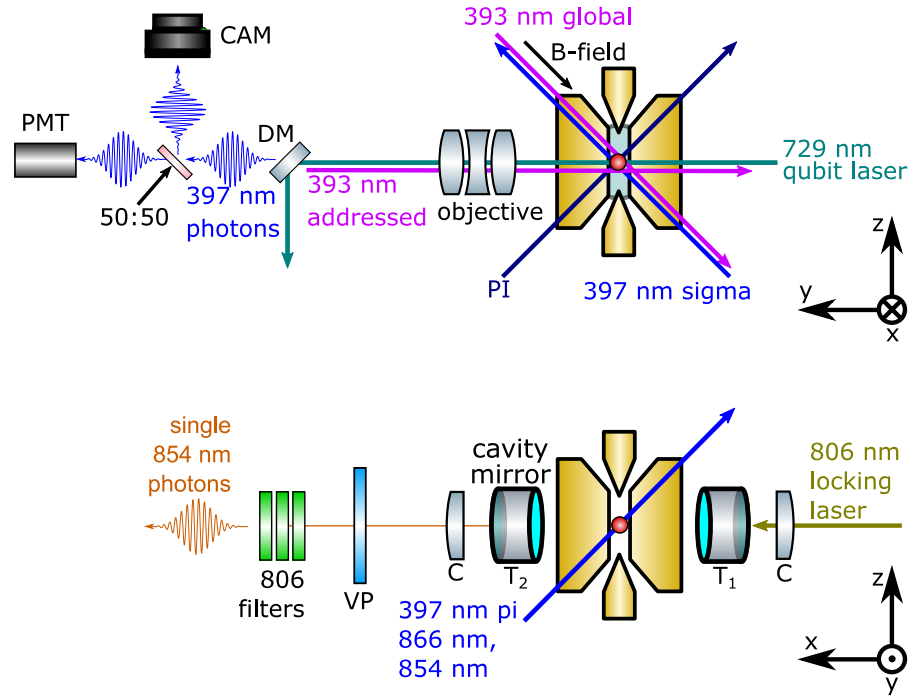


Figure 3.3: **Orientations of the cavity-ion-trap system.** The atomic ions (red sphere) are centred in both a 3D radio-frequency linear Paul trap (gold coated electrodes) and an optical cavity with transmissions of  $T_{1,2}$ . Along the cavity axis (top), showing: the  $\sim 4.229$  Gauss DC magnetic field (quantisation axis) generated by rings of permanent magnets and the circularly-polarized Raman laser for generating 854 nm cavity photons. Photo-ionization (PI) laser for a two step ionization of calcium at 422 nm and 375 nm. The photons produced by the electron-shelving method [42, 43] are collected with an objective and filtered from the 729 nm qubit laser before detected with a photo-multiplier tube (PMT) and a camera (CAM: ANDOR iXon Ultra). Two different 393 nm Raman drive laser beams used in the photon generation process (CMRT) are available: the global Raman drive laser (393 nm global) is used for most experiments with one ion, the later developed addressed Raman drive laser (393 nm addresses) can address single ions in a multi-ion string. Following a Raman pulse, an 854 nm cavity photon exits the cavity via the left mirror (transmission  $T_2$ ). The photon then passes the following elements: in-vacuum collimating lens (C); vacuum chamber viewport (VP); 3 filters to remove the 806 nm laser light to which cavity length is continuously and actively stabilised.

Some key challenges that were overcome to realise our cavity parameters are now briefly described. First, the super polishing of the surfaces of such tightly curved (10 mm ROC) mirror substrates seems not to be a commercially available process as standard and we are therefore grateful to Perkins Precision, Boulder, who did it as a custom job, achieving an RMS roughness of  $1 \pm 0.2 \text{ \AA}$  and 1.5 ppm scattering losses on a test piece from the batch measured by Perkins Precision. Second, mirror coating via ion beam sputtering was performed by

Advanced Thin Films. Detailed information on the mirror coatings can be found in [69]. Third, the observed birefringence of cavities built using these mirrors could be minimised by rotating mirror pairs with respect to each other, leading to a sub-linewidth ( $2 \cdot \kappa$ ) splitting of  $14 \pm 2$  kHz in the final cavity (measured by Josef Schupp using the method of [76]). The fourth step involved a multi-stage procedure to glue the mirrors into position to achieve the near-concentric cavity. The mirrors are glued into metal rings, in turn glued to single axis piezos for cavity-length stabilisation, in turn glued to a rigid metal spacer spanning the cavity length: the only tunable parameter once glued is the cavity length over the range of the piezos. The fifth and final key step was for the cavity to survive the ion-trap chamber vacuum baking process, meaning that the finesse stays constant before and after the baking. The Vacuum setup was baked at  $80^\circ\text{C}$  for approximately 2 weeks and was led by fellow PhD student Vojtech Krcmarsky, as well as chamber assembly. The temperature for the baking is limited by the glass transition temperature of the cavity glue. Before the bake the cavity finesse was measured to be  $59(1) \times 10^3$ . No measurable drop of the finesse directly after the the bake was measured. After the cavity has been in vacuum for a few weeks, the finesse dropped to  $54(1) \times 10^3$ .

### 3.3 CONVERSION CRYSTALS

For most of the experiments described in this thesis, two  $\text{LiNbO}_3$  crystals ('chips') with integrated waveguides are used, each with a length of 48 mm. Each crystal contains 12 individual ridge waveguides ( $\text{LiNbO}_3$  layer on  $\text{LiTaO}_3$  substrate) milled out along its length. The chips were fabricated by NTT electronics. While each chip has 12 individual waveguides, a single guide in any one chip is used for each experiment. The two waveguides used have slightly different dimensions. The first waveguide in the beam path<sup>1</sup>, used for the polarization maintaining scheme in Section 4.3, has a width of  $12.1 \mu\text{m}$  and a height of  $11.0 \mu\text{m}$ , given from the manufacturers data sheet. Its poling period of  $22.375 \mu\text{m}$  results in an estimated phase matching temperature of  $38^\circ\text{C}$ , as provided by the datasheet. The second waveguide in the beam path<sup>2</sup> has a width of  $12.4 \mu\text{m}$  and a height of  $11.1 \mu\text{m}$ , given from the manufacturers data sheet. Its poling period of  $22.375 \mu\text{m}$  results into a estimated phase matching temperature of  $36^\circ\text{C}$ . The waveguides are single mode for 1550 nm and 1902 nm, multimode for 854 nm and are anti-reflection coated for all those wavelengths on each facet ( $R \leq 1\%$ ). The conversion process is phase matched when all three optical fields have the same linear polarisation; the orthogonal polarisation is supported in the guide but remains unconverted. The

<sup>1</sup> Chip: S/N 3636474, group G1, waveguide WG1

<sup>2</sup> Chip: S/N 3636475, group G1, waveguide WG1

chips are delivered already glued onto an oven system. This oven system contains of a Peltier-element<sup>3</sup> for heating and cooling and a thermistor (10 k $\Omega$  at 25°C). Using with a PID-controller, a feedback loop to control the crystal temperature to a given set temperature was built. More details about the feedback loop can be found in Section A.4 of the appendix.

The fibre-coupled conversion chip, used in Section 4.5, was produced at Stanford University in the group of Martin Feyer by Carsten Langrock. The layout of this chip can be found in the Section A.3 of the appendix. The design of the oven used for the temperature stabilization of this fibre-coupled device which was designed and built within the work of this thesis, can be found in Section A.4 of the appendix. In total we got 4 different devices from Stanford with 32 waveguides on each. Since the devices are fibre-coupled, only one waveguide per chip is used. The fibre-coupled device used in the experiment in Section 4.5 was temperature stabilized at 74.4°C. The fibre-coupled devices, unlike the ridged waveguides from NTT, are buried waveguides and they convert and guide only one polarization.

### 3.4 SINGLE PHOTON DETECTORS

For 854 nm photons, we have two fibre-coupled avalanche photo diodes (APD) and two fibre-coupled superconducting nanowire single-photon detectors (SNSPD). The APDs are Laser Components COUNT-10C-FC. The SNSPDs are Scontel FCOPRS-CCR-2TW75+2SW85. The corresponding efficiencies and dark count rates are shown in table 3.1. The SNSPDs were only available towards the end of my PhD thesis, hence not all experiments were carried out with them.

854 nm Detector	APD 1	APD 2	SNSPD 1	SNSPD 2
Efficiency in %	40	40	87	88
Dark count rate	10	10	0.3(1)	0.5(1)

Table 3.1: Efficiency and dark count rate for 854 nm single photon detectors. APDs: Laser Components COUNT-10C-FC. SNSPDs: Scontel FCOPRS-CCR-2TW75+2SW85. The values for the APDs are given by the manufacturers specification sheet, the numbers for the SNSPDs are directly measured by a Scontel representative in the lab after the installation using a calibrated single photon source.

---

<sup>3</sup> FerroTec 9501/023/040B

For the detection of 1550 nm photons we have one fibre-coupled solid state detector (ID Quantique ID230 FR-SMF) and two fibre-coupled SNSPDs (Scontel FCOPRS-CCR-2TW75+2SW85). The corresponding efficiencies and dark count rates are shown in table 3.2.

1550 nm Detector	Solid state	SNSPD 1	SNSPD 2
Efficiency in %	10	74	75
Dark count rate	1.9(2)	0.6(1)	0.6(1)

Table 3.2: Efficiency and Dark count rate for 1550 nm single photon detectors. Solid state: ID Quantique ID230 FR-SMF. SNSPDs: Scontel FCOPRS-CCR-2TW75+2SW85. The efficiency of the solid state detector is given by the manufacturer, the efficiencies for the SNSPDs are measured by a Scontel representative the lab using a calibrated single photon source. The dark count rates are measured by a Scontel representative in the lab by blocking the detector input.

The detectors produce an electronic output pulse to signal the detection of a photon. These pulses are recorded with a time tagging module (Swabian Instruments, Time Tagger 20). The time tagging module has 8 different input ports and perform a range of different functions on the inputs. The two main functions used in this thesis are now described.

First, the most general function is the direct recording of the events (input pulses) including the time stamps and the channels. This function is used when the absolute photon arrival time is needed e. g. for reconstructing the temporal photon wavepacket. The recording of the time stamps is also used when the recorded data has to be post processed e. g. combined with the ion state detection data. Since this method needs post processing, live view of the measured data is difficult.

The second function can be easily displayed live and is called *count between*. This function counts the electric pulses from the photon detectors between a start and a stop flag, which is defined by one of the input ports of the detector. In our experiments, those flags are sent from the PulseBox that controls our experiment overall (see Section A.1 of the appendix). A rising edge of this channel starts the counting, a falling edge stops the counting. We start and stop the counting for each photon generation attempt around the estimated photon arrival time at the detectors. Since we produce single photons, the counts during this time frame are either 0 (attempt was not successful) or 1 (attempt was successful). The rare events, where together with a successful attempt a noise photon happened are ignored. The number of the detected photons during these time frames are sent to the control PC where they are recorded and displayed. Since the *count between* method can be easily implemented and displayed almost in real time

while scanning experimental parameters, it is mostly used for setting up the experiment and optimizing the sequence parameters.

For all the experimental data shown in this thesis, the recording of the time stamps was used.

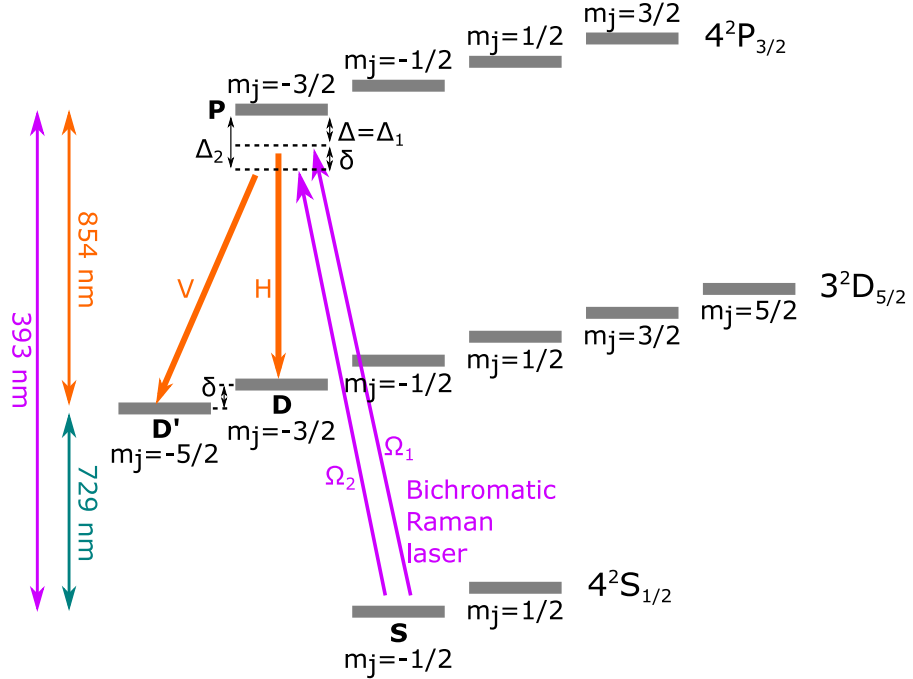


Figure 3.4: **Level scheme of  $^{40}\text{Ca}^+$  and photon generation scheme.** In this figure, the levels in  $^{40}\text{Ca}^+$  are displayed that are used in our experiments to produce single 854 nm photons with a bichromatic cavity-mediated Raman transition. Following optical pumping, the ion (single outer valence electron) is in the state  $|S\rangle = |4^2S_{1/2, m_j=-1/2}\rangle$ . Photons are generated via cavity-mediated Raman transitions (CMRT). In case of  $\Omega_2 = 0$ , the 393 nm Raman laser pulse leads to the generation of a horizontally-polarized  $|H\rangle$  photon in the optical cavity and the electron ends up in the state  $|D\rangle = |3^2D_{5/2, m_j=-3/2}\rangle$ . In the case of  $\Omega_1 = 0$  a vertically-polarized  $|V\rangle$  photon is generated in the optical cavity and the electron ends up in the state  $|D'\rangle = |3^2D_{5/2, m_j=-5/2}\rangle$ . Here H stands for the linear polarization along the B-field quantisation axis ( $\pi$ -photons). The V polarization stands for the orthogonal linear polarization, produced by the projection of the  $\sigma$ -polarized photons into the plane perpendicular to the cavity direction (and perpendicular to the B-field quantisation axis). The overall detuning is set to  $\Delta_1/2\pi = 403 \pm 5$  MHz. The D-state Zeeman splitting in our setup is  $\delta/2\pi = 7.107(1)$  MHz. During a bichromatic CMRT both detuned Raman laser are driving the corresponding transition with the same strength, ideally ending up in an entangled ion-photon state of  $\frac{1}{\sqrt{2}}(|D, H\rangle + |D', V\rangle)$

### 3.5 854 NM PHOTON GENERATION

In Section 3.5.1 an overview of our method for producing single 854 nm photons from  $^{40}\text{Ca}^+$  via a cavity is provided. Section 3.5.2 will extend this method to produce single photons which are entangled via their polarisation with the final electronic state of the ion. More detailed theoretical models of the techniques presented in this section are shown in [31, 69, 71, 77].

#### 3.5.1 *Single photons via a cavity-mediated Raman process*

Our photon generation scheme is based on a cavity-mediated Raman transition (CMRT) [78, 79]. For photons not entangled with the ion, the CMRT couples the initial state  $|S\rangle |0\rangle = |4^2S_{J=1/2}, m_j = -1/2\rangle |0\rangle$ , where the second ket vector describes the cavity photon number, to the metastable final state  $|D'\rangle |1\rangle = |3^2D_{J=5/2}, m_j = -5/2\rangle |1\rangle$  via the intermediate excited state  $|P\rangle |0\rangle = |4^2P_{J=3/2}, m_j = 3/2\rangle |0\rangle$ . The three atomic states are shown within the energy level scheme in Figure 3.4. States  $|P\rangle$  and  $|D'\rangle$  have finite lifetimes of 6.9 ns and 1.1 s, respectively.

A circularly-polarised drive laser ( $1 \times 10^2$  Hz linewidth [75]) addresses the  $|S\rangle \leftrightarrow |P\rangle$  dipole transition at 393 nm with a detuning  $\Delta_2/2\pi = 410(5)$  MHz and a Rabi frequency  $\Omega_2$ . The cavity is detuned by the same amount from the 854 nm  $|D'\rangle \leftrightarrow |P\rangle$  dipole transition, and its length is actively stabilised via the Pound-Drever-Hall method to a laser at 806 nm wavelength, as described in [69]. Both this laser and the drive laser are stabilised to a common in-vacuum reference cavity with a drift rate of 720 Hz/hr [75].

The maximum ion-cavity coupling strength on the  $|D'\rangle \leftrightarrow |P\rangle$  transition was measured to be  $g_{\text{exp}}/2\pi = 1.25(1) \times \zeta$  MHz [69], where the geometric factor  $\zeta \leq 1$  is the projection of the cavity polarisation onto the atomic dipole moment. The relationship between  $g_{\text{max}}$  (Section 3.2) and  $g_{\text{exp}}$  is given by the equation  $g_{\text{exp}} = g_{\text{max}} \times CG \times \eta$  where  $CG$  is the Clebsch Gordan coefficient of the  $D' - P$  transition. Note that the coupling strength  $g$  of the cavity is given by properties of the cavity (length and mode area at the ion), the relevant spontaneous atomic decay rate and the projection of the cavity polarization onto the atomic dipole moment. Further details can be found in the Appendix of [71] and in [69]. A 4.23 G magnetic field, set by rings of permanent magnets, is aligned perpendicular to the cavity axis and parallel to the propagation direction of the drive field. The atomic quantisation axis is chosen to be parallel to the magnetic field axis, and photon polarisation along this axis is denoted horizontal ( $H$ ). The polarisation of the photon generated in the cavity is vertical ( $V$ ), as determined by the projection of the  $|g\rangle \leftrightarrow |e\rangle$  dipole moment onto the plane perpendicular to the cavity axis, corresponding to  $\zeta = \sqrt{0.5}$  and  $g_{\text{exp}}/2\pi = 0.88(1)$  MHz. The effective coupling strength of the

CMRT is  $\Omega_{eff} = g\Omega_2/(2\Delta_2)$ . The CMRT competes with spontaneous decay with an effective rate  $\gamma_{eff} = [\Omega_2/(2\Delta_2)]^2\gamma$ , where  $\gamma = 11.49(3)$  MHz is the decay rate of  $|e\rangle$  [80]. For the second order correlation experiment in Section 6 we used the described CMRT to produce single vertically-polarized photons. For the Hong-Ou-Mandel experiment in Section 7 we used different transitions to produce either horizontally or vertically-polarized photons.

### 3.5.2 Ion-photon entanglement via a bichromatic cavity-mediated Raman process

The CMRT in Section 3.5.1 produces single photons with a defined polarization. For producing photons where the polarization of the photon is entangled with the electronic state of the ion, a bichromatic CMRT is used, which was first demonstrated in [31].

For the bichromatic CMRT the drive laser contains two co-propagating frequencies. While one drive laser frequency has a detuning  $\Delta_1/2\pi = 403 \pm 5$  MHz from  $|P\rangle$  and generates a horizontally-polarized photon and the electron ends up in  $|D\rangle = |3^2D_{J=5/2}, m_j = -3/2\rangle$ , the second drive laser frequency has a detuning  $\Delta_2 = \Delta_1 + \delta_{393}$  (with  $\delta_{393} = \delta$  the detuning between  $|D\rangle$  and  $|D'\rangle$ ) and generates a vertically-polarized photon and the electron ends up in  $|D'\rangle$ . When both transitions occur with the same probability, the state  $|S, 0\rangle$  evolves to  $\frac{1}{\sqrt{2}}(|D, H\rangle + |D', V\rangle)$ , which is a maximum entangled state where the phase is set by the relative phases of the laser fields involved in generating and characterising the state [31].

Section 5 of this thesis uses the bichromatic CMRT to produce entangled ion - photon pairs. In Section 8 this technique was used to demonstrate parts of a quantum repeater.

The state readout of the ion-qubit in our experiment is performed via the standard electron shelving technique as summarised in Section 2.1.3. This method is able to distinguish between ground states ( $|S\rangle$ ) and excited states ( $|D\rangle$  and  $|D'\rangle$ ). After CMRT, the ion stays in a superposition between the two excited states and therefore can't be read out directly. First, we map the electron population from  $|D'\rangle$  to the  $|S\rangle$  via a 729 nm  $\pi$  pulse (Figure 3.4). Now the standard electron shelving technique can be used to perform state detection. The aforementioned process implements a projective measurement into the eigenstates of the  $\sigma_z$  basis (Pauli spin-1/2 operator). To perform measurements in other bases e.g  $\sigma_x$  ( $\sigma_y$ ), as required for full quantum state tomography, an additional 729 nm  $\pi/2$  pulse on the  $|S\rangle$  to  $|D\rangle$  transition with a 0 ( $\pi/2$ ) phase is applied after the  $\pi$  pulse and before the electron shelving, to rotate the ion-qubit measurement basis. In order to produce an ion-photon state whose phase does not depend on the detection time of the photon, the frequency difference of the two used 729 nm laser pulses ( $|S\rangle \leftrightarrow |D\rangle$  and  $|S\rangle \leftrightarrow |D'\rangle$ ) and the frequency difference

of the two tones of the bichromatic Raman pulse  $\delta_{393}$  should equal the detuning  $\delta$  between  $|D\rangle$  and  $|D'\rangle$ :  $\delta = \delta_{393} = \delta_{729}$ .



## POLARISATION-PRESERVING PHOTON FREQUENCY CONVERSION

---

This chapter includes the setup and results of a polarization maintaining frequency converter, which converts light resonant with the 854 nm transition of  $^{40}\text{Ca}^+$  to the 1550 nm telecom C-band. The main results are published in [Appl. Phys. B 123, 228 \(2017\) \[17\]](#) and the authors are Victor Krutyanskiy (VKru), Martin Meraner (MM), Josef Schupp (JS) and Ben Lanyon (BPL). VKru and MM designed and built the conversion setup. JS built the 854 nm laser setup. Experimental data taking was done by VKru and MM. Data analysis and interpretation was done by VKru, JS, MM and BPL. All authors contributed to the paper writing. The project was conceived and supervised by BPL.

This chapter presents both an extended discussion of the work that is summarized in [17] and additional experimental measurements regarding limitations of the total efficiency and characterization of fibre coupled frequency converters designed and built by the group of Martin Fejer in Stanford. At time of writing those results were unpublished. Experimental data were taking by Vojtech Krcmarsky and Martin Meraner.

In this chapter, experiments that demonstrate photon conversion from  $\lambda_s = 854$  nm ( $s =$  signal) to  $\lambda_t = 1550$  nm ( $t =$  target, Telecom C-band), via difference-frequency generation (DFG) in a waveguide-integrated  $\chi^{(2)}$  crystal, using a strong pump laser at  $\lambda_p = 1902$  nm are presented. The 854 nm laser light is the wavelength of the  $|D\rangle$  to  $|P\rangle$  transition of  $^{40}\text{Ca}^+$  ions. For the experiments in this chapter we use attenuated laser light to simulate single photons.

The content of this chapter is now described, the significant majority of which is taken directly from our paper [17]. Section 4.1 contains a general introduction to the project. Section 4.2 presents a polarisation-dependant telecom conversion scheme for 854-nm light. Here, the achieved conversion efficiency is shown and the underlying limits are studied. Additionally, the photon noise generated by the conversion process is presented. Section 4.2 includes Figure 4.3 and an associated discussion, which were not published as part of [17]. Section 4.3 presents a polarisation-independent conversion scheme allowing translation of a polarisation qubit from 854 nm to 1550 nm. The con-

version efficiency of a fibre-coupled device and its advantages and disadvantages are shown in Section 4.5. This section is entirely new and was not published in [17]. Finally in Section 4.6 this chapter is summarized and ideas on further improvements are presented.

#### 4.1 INTRODUCTION

There is a current multi-disciplinary research initiative to develop light-matter quantum networks [3]; remote nodes, consisting of precisely-controllable quantum matter in which quantum information is stored and processed, that are interconnected with quantum light, such as single photons. These networks, envisaged over distances from table-top to intercontinental, could enable a range of new science and technology, including scalable quantum computing [7], secure communication [81] and enhanced sensing [82].

Given the great success in encoding, manipulating, storing and reading-out quantum information in their electronic states, trapped atomic ions represent a powerful platform with which to build, or integrate into, the nodes of quantum networks [26, 83]. Indeed, an elementary quantum network consisting of ions in two traps a few meters apart, has been entangled via travelling ultraviolet photons [10]. A challenge is that most readily-accessible photonic transitions in trapped ions lie at wavelengths that suffer significant absorption loss in materials for manipulating and guiding light, thereby limiting the internode networking distance. Another challenge is that ionic transitions are fixed and narrowband, such that, except in rare cases [84], they cannot be interfaced with other examples of quantum matter to enable new ion-hybrid quantum systems [85]. Note that frequency-distinguishable quantum systems can be linked via their photons, though at the cost of reducing the efficiency of making that link [86].

The aforementioned challenges could be overcome using quantum frequency conversion (QFC) [47, 87]; a nonlinear optical process in which a photon of one frequency is converted to another, whilst preserving all the quantum and classical photon properties. QFC of single photons has recently been studied in a variety of contexts [60, 88–92] and is typically achieved using three-wave mixing in a second-order nonlinear ( $\chi^{(2)}$ ) crystal. It has been shown that QFC can preserve a broad range of photon properties, including first- and second-order coherence, and pre-existing photon-photon entanglement [87, 93, 94]. QFC could therefore act as a quantum photonic adapter for trapped ions, allowing their high-energy photonic transitions to be interfaced with the lower-energy photons better suited for long-distance travel through optical fibres, or with other forms of quantum matter.

Interfacing trapped ions with the telecom wavelengths of 1310 nm (O band) or 1550 nm (C band) is particularly appealing: these wavelengths suffer minimal transmission losses (0.32 and 0.18 dB/km, respectively

for SMF-28 Ultra fibre) through optical fibres and a broad range of established technologies and infrastructure for their manipulation and transmission exist. The telecom wavelengths are therefore an ideal choice for a universal standard for light-matter quantum networks, allowing similar and dissimilar quantum matter to interface over both short and long distances.

Telecom frequency conversion of photons connected to several examples of quantum matter has recently been demonstrated, including quantum dots [16, 95–97], cold gas atomic ensembles [98–100] and solid-state ensembles [101]. Applying QFC to trapped ions is challenging. The comparatively low rate and efficiency with which photons have been collected from / absorbed by an ion demands a highly efficient and low noise conversion process. Readily accessible photonic transitions in ions also lie in the ultraviolet or visible regime, which suffer high absorption and strong dispersion in nonlinear crystals. Furthermore, direct (single step) conversion of those photons to telecom in the so called ‘long pump wavelength regime’ is not possible, leading to additional noise processes during conversion [60]. Nevertheless, significant progress has been made in overcoming these challenges [102–104]. In [104], for example, the authors convert attenuated laser light at 369.5 nm (a transition in  $\text{Yb}^+$ ) to 1311 nm, achieving a waveguide efficiency of  $\sim 5\%$  (including coupling losses) and a total efficiency for fibre-coupled output photons of 0.4%.

## 4.2 POLARISATION-DEPENDENT CONVERSION SCHEME

### 4.2.1 *Experimental details*

A summary of the experimental setup is now provided, which is further detailed in Figure 4.1. For the pump we use a 1902 nm Tm-doped fibre laser (AdValue Photonics AP-SF1) and for the 854 nm input a diode laser (Toptica DL pro). The diode laser is stabilised to within a few MHz of the ionic transition using a wavemeter lock (High Finesse WSU10). Both signal and pump are delivered to the photon conversion setup using polarisation-maintaining single-mode optical fibre, spatially overlapped using a dichroic mirror and free-space coupled into a ridge waveguide (see Section 3.3) via an aspheric lens. A second asphere at the waveguide output collimates the output fields, which are then sent to various filtering and analysis stages. The chip is temperature-stabilised (see Section A.4 of the appendix) and a waveguide is chosen with a quasi-phase matching temperature of  $38^\circ\text{C}$ . The spectral acceptance bandwidth of the phase matched conversion process centred at 854 nm is measured to be  $\sim 0.2$  nm

(82 GHz)<sup>1</sup>, which agrees with theoretical calculations based on refractive indices of bulk LiNbO<sub>3</sub> at the corresponding wavelengths [105]. Note that this acceptance bandwidth for photon conversion is orders of magnitude broader than 854 nm photons from the ion and from our narrowband laser source, and does not therefore act as a filter. The temperature bandwidth (FWHM) of the phase matched conversion process is measured to be  $2.4 \pm 0.2$  °C. For the temperature bandwidth the conversion efficiency for different temperatures of the waveguide was recorded and the full-width half-maximum (FWHM) of the converted telecom light was calculated.

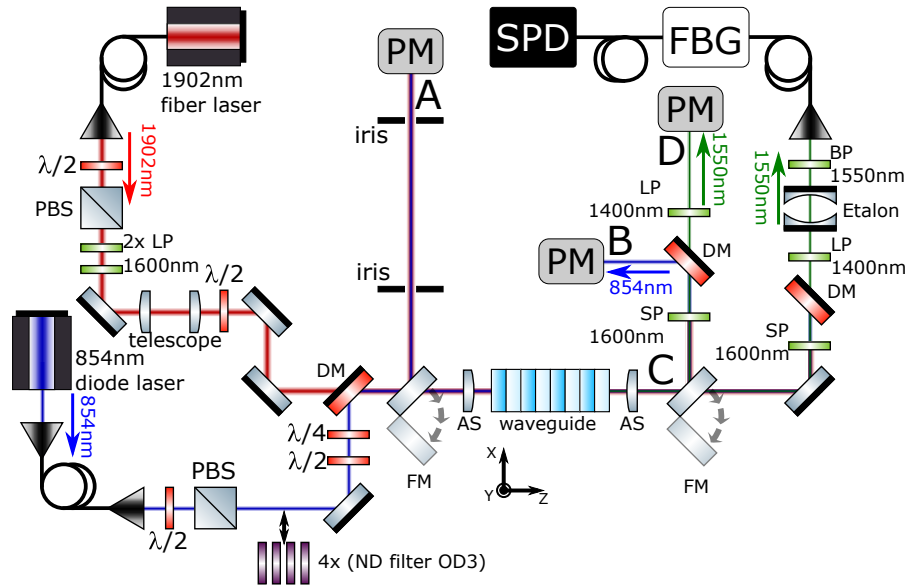


Figure 4.1: Setup for polarisation-dependent frequency conversion from 854 nm to 1550 nm. LP 1600 nm – longpass filters (Edmund Optics 84-680); DM – dichroic mirror (Layertec 103472, highly reflective for 854 nm, transmissive for 1550 and 1902 nm); FM – gold flip mirror; AS – 11mm asphere lenses (Thorlabs A220<sup>TM</sup>) positioned by XYZ translation stage; SP 1600 nm – shortpass filter (Edmund Optics 84-656, OD<sub>5</sub> at 1902 nm); LP 1400 – longpass filter (Thorlabs FELH1400) prevents detecting second harmonic of pump; BP 1550 nm – bandpass filter (Thorlabs FB-1550, 63% transmission, OD<sub>5</sub>); Etalon – air-spaced Fabry-Pérot cavity (SLS optics): 250 MHz linewidth, 12.5 GHz free spectrum range, peak transmission 95% at 1550 nm, extinction 10<sup>3</sup>; FBG – fibre Bragg grating filter (Advanced Optical Solutions): bandwidth 15 pm (2 GHz), transmission 60% at 1550 nm, extinction 10<sup>3</sup>; PM – power meters; SPD – avalanche photo diode based single telecom photon detector .

<sup>1</sup> The spectral acceptance bandwidth was measured by detuning the 854 nm diode laser whilst recording the converted 1550 nm output power. The presented bandwidth is the FWHM

## 4.2.2 Results

### 4.2.2.1 Efficiency

We begin by sending 315  $\mu\text{W}$  of 854 nm laser light to the waveguide, optimising the in-coupling to maximise the population of the lowest order (fundamental) mode using a beam profiler<sup>2</sup> at the output. Using an optical power meter<sup>3</sup> the input 854 nm power is measured at point A (see Figure 4.1),  $P_{854}^A$ , the output at point B,  $P_{854}^B$  and the transmission at 854 nm is quantified as  $T_{854}^{B/A} = P_{854}^B / P_{854}^A$ . For zero pump power, we find  $T_{854}^{B/A} = 0.73 \pm 0.01$ .

The known relevant optical losses at 854 nm between points A and B are: two uncoated aspheres (measured transmission  $T_a = 0.93$  each); shortpass filter (measured transmission  $T_{sp} = 0.96 \pm 0.03$ ); dichroic mirror (reflection  $R_d = 0.99$ ). When considering these losses we find a waveguide transmission of  $T_{854}^{waveguide} = T_{854}^{A/B} / (T_a^2 T_{sp} R_d) = 0.89 \pm 0.04$ , that now contains losses only due to waveguide in-coupling and propagation. The input (output) 1902 nm pump power is measured at point A (C), yielding a pump transmission of  $T_{1902}^{C/A} = 0.57 \pm 0.01$ . The output 1550 nm power  $P_{1550}^D$  is measured at point D.

In the following we report on investigations of the system conversion efficiency as a function of the pump laser power. For the pump laser power we use the value measured at point C ( $P_{1902}^C$ ), which is after the waveguide and last aspheric lens. This power, which we call the out-coupled pump power from now on, gives a lower bound on the pump power inside the waveguide. The actual pump power inside the guide is higher. The expected transmission of 1902 nm through the uncoated output asphere is 0.92 (twice 4% reflection due to the un-coated air-glass interface), meaning that a better estimate for the pump power at the output facet of the waveguide is a factor  $1/0.92$  higher than  $P_{1902}^C$ . For the attenuation in a  $\text{LiNbO}_3$  waveguide the manufacturer gives an upper bound of 0.2 dB/cm for all used wavelengths. Using an 0.2 dB/cm for the 1902 nm attenuation, one expects a transmission of 0.8 through the waveguide - yielding our best estimate for the in-coupled pump power of  $1/(0.8 \times 0.92) \times P_{1902}^C$ .

Figure 4.2 presents the measured conversion efficiency, quantified by  $\eta_{classical}^{D/A} = P_{1550}^D / P_{854}^A \times 1550/854$  (equivalent to ratio of photon numbers), as a function of output pump power  $P_{1902}^C$ . The depletion of the 854 nm signal is also shown, quantified by the transmission at 854 nm  $T_{854}^{B/A}$ . The results show a maximum conversion efficiency  $0.46 \pm 0.01$  for an out-coupled pump power of 200 mW.

When removing the known relevant losses in optics around the waveguide at 854 nm and 1550 nm, one obtains a maximum achieved external classical waveguide conversion efficiency of  $\eta_{class}^{waveguide} =$

<sup>2</sup> Beam profiler: Spiricon Pyrocam IIIHR

<sup>3</sup> Power meter: Thorlabs PM100D + S130VC

$0.59 \pm 0.03$ , which still contains losses due to in-coupling into the waveguide and waveguide propagation losses <sup>4</sup>.

Assuming that the waveguide transmission losses are equal at 854 nm and 1550 nm,  $0.89 \pm 0.04$  is the maximum conversion efficiency, limited by the transmission loss through the waveguide. The value that we obtain,  $\eta_{class}^{waveguide}$ , is  $0.30 \pm 0.05$  lower than this maximum. Figure 4.2 shows that, at the point of maximum conversion efficiency, a fraction  $0.22 \pm 0.01$  of unconverted 854 nm light remains at the waveguide output (when accounting for known passive optical losses). One sees, therefore, that the majority of ‘missing conversion efficiency’ lies in unconverted 854 nm light.

In the case of perfect phase matching and no losses, the DFG process for three optical modes in a waveguide allows for complete depletion (conversion) of the signal wave. However, the situation is more complicated when several spatial (or axial [106]) modes are involved. Indeed, our waveguides are multimode at 854 nm and a fraction of 854 nm populates higher-order modes due to imperfect mode matching at the input. The different modes have different effective refractive indices than the fundamental mode and are not, therefore, simultaneously phase matched. As a consequence, the conversion efficiency of higher order modes is weak and they remain largely unconverted.

The population of 854 nm in higher-order spatial modes of the waveguide can be seen in beam profile measurements at the output of the waveguide. We measured the beam profile of the out-coupled 854 nm laser by replacing the power meter at point B with an infrared beam profiler<sup>5</sup>. Two different measurements are taken. First, while no pump laser field is coupled into the waveguide. Second, while the optimal pump power is coupled into the waveguide to provide maximum achievable conversion efficiency, leaving behind the remaining unconverted 854 nm beam. The filters after the waveguide and before the beam profiler allows to display the 854 nm beam only. Figure 4.3a)b) shows the two recorded measurements of the out-coupled 854 nm beam without and with conversion. The converted part of the 854 nm beam can be calculated by subtracting the unconverted beam from the total beam, which is shown in Figure 4.3c). In the case of optimum conversion, the remaining unconverted 854 nm light is distributed into high order spatial modes. Improved mode matching of the input 854 nm light into the fundamental waveguide mode is therefore expected to increase the conversion efficiency. However, since the achieved conversion efficiency is already high enough to perform long distance quantum networking, this mode matching was not performed or further investigated.

<sup>4</sup>  $0.59 = 0.46 / (0.93 \cdot 0.93 \cdot 0.96 \cdot 0.94 \cdot 0.995)$ , where the denominator contains transmissions at the relevant wavelength for: in-coupling asphere; out-coupling asphere; shortpass filter; dichroic mirror; longpass filter.

<sup>5</sup> Infrared beam profiler: Spiricon Pyrocam IIIHR

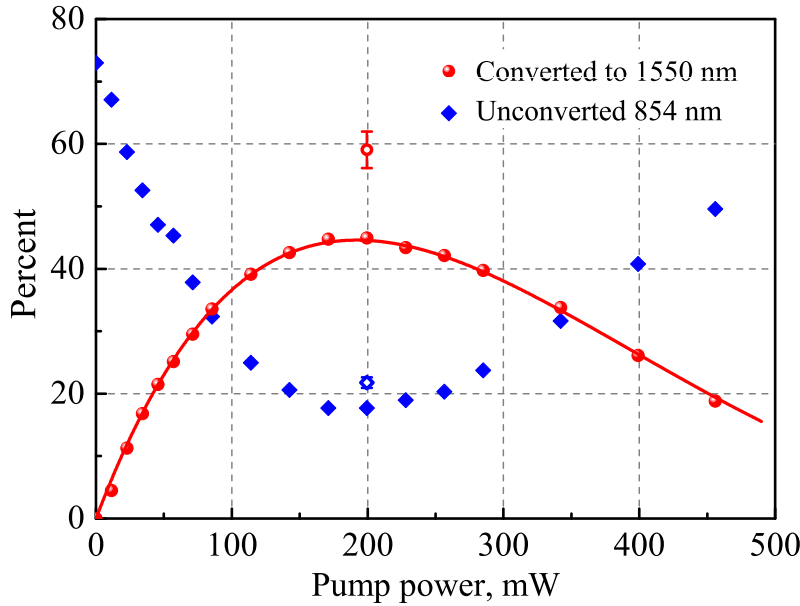


Figure 4.2: Conversion efficiency, of 315  $\mu\text{W}$  of 854 nm laser light to 1550 nm, as a function of out-coupled pump power. Solid red spheres: conversion efficiency to 1550 nm  $\eta_{\text{classical}}^{A/B}$ . Unfilled red circle: waveguide conversion efficiency to 1550 nm  $\eta_{\text{classical}}^{\text{waveguide}}$ , after accounting for known passive optical losses. Solid red line: theoretical fit by the function  $\eta = A \cdot \sin^2(\sqrt{\eta_{\text{nor}}} P_p L)$  with fitting parameters  $A = 0.45$ ,  $\eta_{\text{nor}} = 0.56 \text{W}^{-1} \text{cm}^{-2}$ . Filled blue diamonds: fraction of remaining 854 nm light  $T_{854}^{B/A}$  after the waveguide. Unfilled blue diamond: fraction of remaining 854 nm light after the waveguide, when accounting for known passive optical losses. Visible error bars stem from uncertainty in passive loss of optical elements. The out-coupled pump power was measured after the waveguide and the aspheric lens at point C of Figure 4.1.

We conclude from this experiment that a waveguide conversion efficiency of  $0.59 \pm 0.03$  was achieved, limited by the unintentional excitation of higher-order waveguide modes at 854 nm. An increased efficiency should be possible by exploring methods to reduce higher-order mode excitation, such as more careful mode matching between the Gaussian free-space mode and the elliptical waveguide fundamental mode. Our efficiency is comparable to the highest values achieved in frequency conversion experiments performed to date [53, 60, 95, 107, 108].

#### 4.2.2.2 Noise at the single-photon level

Any way in which the strong pump laser field can introduce photons directly at the output telecom wavelength introduces noise that can dominate the single-photon QFC signal. We call the rate of such noise the noise photon rate (NPR) to distinguish it from the intrinsic detector dark count rate (DCR).

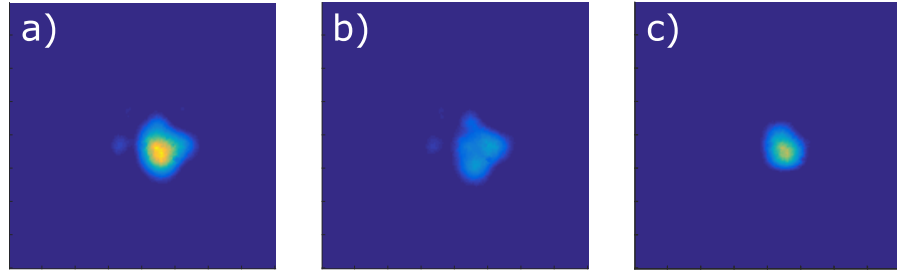


Figure 4.3: **Measured 854 nm beam profiles after the first waveguide:** a) 854 nm light field after the waveguide without conversion (no pump laser). b) Remaining unconverted 854 light field after the waveguide for optimal conversion (200 mW of out-coupled pump laser). c) Subtraction of the images in b) from the one in a). This corresponds to the depleted (converted) fraction of the 854 nm light. One sees that high order spatial modes are not converted. This data was taken with the Pyrocam IIIHR from Spiricon/ Ophir. The colour scale of the displayed data follows an arbitrary scale as the camera is not calibrated. This figure and the associated discussion was not part of [17].

At 200 mW (out-coupled), the pump photon flux in the waveguide is vast ( $2 \times 10^{18}$  Hz) such that even extremely weak processes in the waveguide, through which pump photons are converted directly to telecom, can overwhelm the output. The key process through which this happens on propagation through the crystal is anti-Stokes Raman scattering, where pump photons receive energy from phonons in the crystal (see Section 2.2.3). Anti-stokes Raman spectra for similar ridge waveguides to ours are presented in [109] and show that the large spectral separation between our 1902 nm pump and 1550 nm target is far from any Raman resonance peaks. Nevertheless, significant noise at single photon level has been observed at spectral separations well beyond that expected by theory [60], covering even the large spectral separation in our experiments.

We study the noise photons at the waveguide output for 200 mW out-coupled pump light only, using the analysis path with a photon detector in Figure 4.1. That analysis path consists of various removable filters and finally a single-mode-fibre-coupled, free-running InGaAs solid-state single photon detector (IDQuantique ID230 NIR). The detector is operated in a regime with the highest ratio of efficiency (10%, as specified) to dark counts ( $1.8 \pm 0.1$  counts/s), achieved with a deadtime of 20  $\mu$ s.

For room temperature operation and a 12 nm filtering bandwidth, we observe a total detector click rate of 1.4 kHz, which is completely dominated by noise photons. When accounting for our detector efficiency of 0.1, that noise rate corresponds to 14 kHz of photon noise in the filtering bandwidth before detection (Fig. 4.4). The NPR is seen to reduce with crystal temperature  $T$ , as one would expect for anti-Stokes Raman scattering, approximately following the phonon occupation

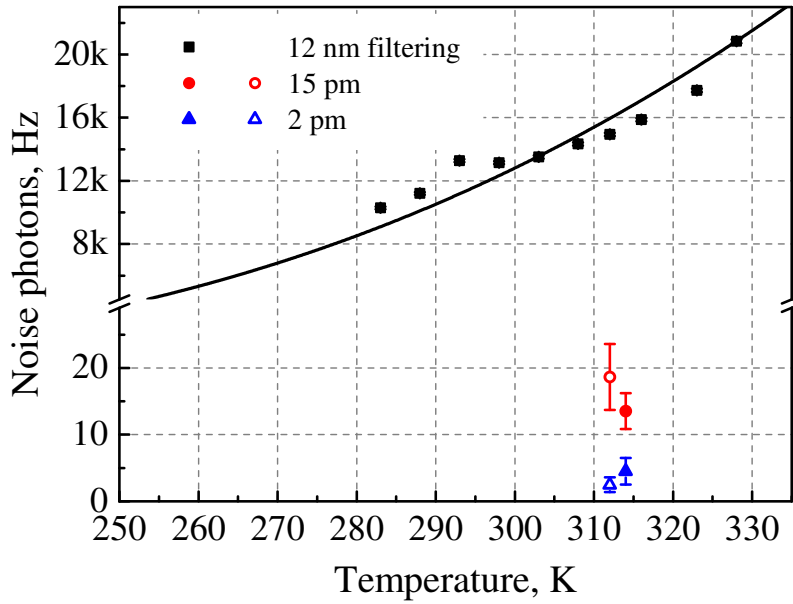


Figure 4.4: **1550 nm noise photons produced directly by interaction of the strong pump with the waveguide.** Plotted values are ten times the count rate of the single photon telecom detector, for 200 mW of out-coupled pump light of the waveguide alone (Figure 4.1). The factor of ten accounts for the 10% detector efficiency, yielding the total noise photons within the filtering bandwidth before detection. Rates are shown for three different filtering bandwidths centred at 1550 nm, as labelled, and for different temperatures of the waveguide. Filled points represent experimental data. Empty points show the count rate expected for the corresponding filtering bandwidth, when starting with the observed values for 12 nm bandwidth and assuming that the noise spectrum is white (points slightly shifted to the left for clarity). 12 nm (squares) and 15 pm (circles) filtering bandwidth values are normalised to total transmission efficiency of 2 pm bandwidth filtering stage (triangles), i. e. multiplied by factors 0.98 and 0.82 respectively, to allow for direct comparison. Solid line shows the fit by a Boltzmann distribution.

number given by the Boltzmann distribution  $\text{NPR} = Ae^{-\frac{\hbar\Delta\omega}{k} \cdot \frac{1}{T}}$ , where  $\Delta\omega$  is pump-target frequency difference;  $\hbar, k$  are Planck and Boltzmann constants,  $A$  is a fitting parameter. By extrapolation of the theoretical fit, operation at  $-50^\circ\text{C}$  could provide a total noise reduction by a factor of 9. This offers a way to reduce photon noise, without the need for narrowband filtering.

The NPR at the quasi-phase matching temperature is seen to reduce in proportion to the filtering bandwidth (Figure 4.4), consistent with the noise source being broadband and white. Using our narrowest filtering bandwidth of 2 pm at 1550 nm (250 MHz bandwidth, transmission  $0.26 \pm 0.01$  at 1550 nm), the NPR before detection is reduced to  $4 \pm 2$  Hz. Note, in Section 4.3 we employ a few picometer filtering stage with a greatly improved transmission at 1550 nm.

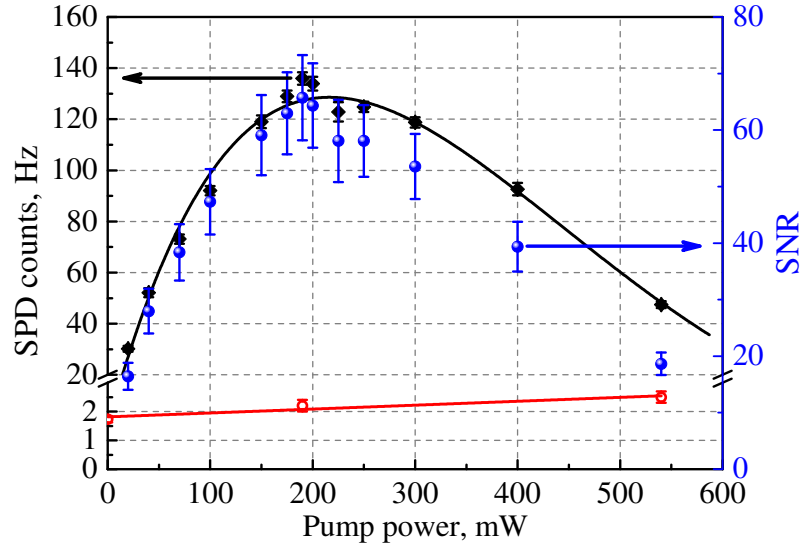


Figure 4.5: **Conversion efficiency, of single-photon-level 854 nm laser light to 1550 nm, as a function of pump power.** Black diamonds: telecom single photon detector count rate for an average of 10 kHz 854 nm photons at the waveguide input (signal). Black solid line: fit by function  $\eta = A \cdot \sin^2(\sqrt{\eta_{nor} P_p L})$  with fitting parameters  $A = 128.6$ ,  $\eta_{nor} = 0.50 \text{W}^{-1} \text{cm}^{-2}$ . Red circles: single photon detector count rate when the 854 nm input is blocked (noise), Red straight line: linear fit of noise. Blue spheres: signal to noise ratio. All errors bars represent one standard deviation and derive from Poissonian photon counting statistics. The out-coupled pump power was measured after the waveguide and the aspheric lens at point C of Figure 4.1.

#### 4.2.2.3 Efficiency and signal-to-noise ratio, at the single photon level

In order to determine a signal-to-noise ratio (SNR) one has to determine an appropriate signal: the rate of 854 nm photons one can expect to be available for converting in experiments involving a trapped  $^{40}\text{Ca}^+$  ion. Using calibrated neutral density filters, the input 854 nm laser power in our setup is attenuated to a value corresponding to an average photon rate of 10 kHz (2 fW) before the input aspheric lens, to replicate a trapped-ion source. Figure 4.5 presents the photon count rate of the 1550 nm detector as a function of pump power and for our 2 pm bandwidth telecom filter. At the peak conversion efficiency (again at around 200 mW pump)  $136 \pm 3$  Hz counts are recorded, corresponding to a total detected conversion efficiency of  $0.0136 \pm 0.0004$ . When removing the 0.10 efficiency of our detector this corresponds to a photon in/out conversion efficiency of  $\eta_{out/in} = 0.136$ : the probability that an incoming 854 nm photon is converted to a single-mode-fibre-coupled 1550 nm photon that has passed the filtering stage. This result is consistent with our classical light measurements, leading to an ex-

ternal waveguide conversion efficiency of  $0.62 \pm 0.03$  when removing the filtering losses.

Since the detected total noise rate is only a few Hz, the SNR profile shown in Figure 4.5 closely follows the conversion efficiency curve, peaking at  $66 \pm 6$  at 200 mW. A SNR  $> 1$  would therefore be possible for an input 854 nm photon rate 60 times lower than was used ( $\sim 160$  Hz) bringing QFC experiments using 854 nm photons from an ion within reach of existing experimental systems.

### 4.3 POLARISATION-PRESERVING CONVERSION

For applications in quantum networking, the conversion process should preserve any photonic degree of freedom used to encode quantum information. While the single-waveguide conversion scheme presented in Figure 4.1 is suitable for e.g. time-bin encoded photonic qubits, only one polarisation component is converted. Polarisation qubits are appealing as they are straightforward to manipulate, analyse and can be preserved through long optical fibres [110]. Furthermore, polarisation entanglement between ion and 854 nm photon, as well as state mapping to photonic polarisation have been achieved experimentally [31, 111].

#### 4.3.1 Experimental details

The total experimental schematic is shown in Figure 4.6. Our polarisation-preserving conversion scheme, which employs two independent waveguide crystals in series, is now briefly summarised. The conversion process in each waveguide is phase matched when all three optical fields have the same linear polarisation (vertical  $|V\rangle$ ); the orthogonal polarisation (horizontal,  $|H\rangle$ ) is supported in the guide but remains unconverted. Consider an arbitrary input 854 nm single-photon polarisation state  $\alpha |H_{854}\rangle + \beta |V_{854}\rangle$  and input classical pump polarisation state  $\delta |H_{pump}\rangle + \gamma |V_{pump}\rangle$ . The first waveguide in Figure 4.6 converts the component  $\beta |V_{854}\rangle$  to  $\beta |V_{1550}\rangle$  with an efficiency that depends on  $\gamma$ . Next, a Fresnel Rhomb (equivalent to a broadband waveplate) performs a flip operation on the polarisation of all three optical fields, converting e.g.  $|H\rangle$  to  $|V\rangle$  and vice versa. The second waveguide then converts the remaining 854 nm polarisation component, with an efficiency that depends on  $\delta$ . In the case of balanced conversion efficiency for each polarisation, and after renormalisation, the output telecom photon polarisation state is  $\alpha |V_{1550}\rangle + \beta |H_{1550}\rangle$ . In this setup we employ a filtering stage with a 4 pm bandwidth and transmission of 73% for fibre-coupled telecom output photons, afforded via a volume holographic grating. All the used equipment is listed in Figure 4.6. Note that interferometric path length stability between the waveguides is not required as all optical fields follow the same path. Any phase

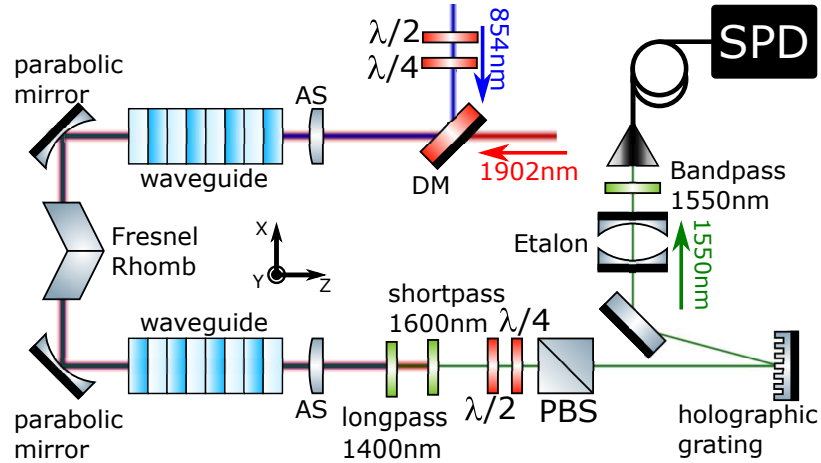


Figure 4.6: **Setup for polarisation-preserving frequency conversion from 854 nm to 1550 nm.** Beam paths for in-coupling fields before dichroic mirror (DM) are the same as in fig. 4.1. Gold parabolic mirrors are used for simultaneous focusing/collimation of all fields ( $F = 15$  mm, Thorlabs MPDooM9); holographic grating – volume Bragg grating, reflection bandwidth 0.2 nm (25 GHz), 95% reflection (OptiGrate); bandpass 1550 nm filter has 12 nm bandwidth and 95% transmission (Thorlabs FBH-1550). Shortpass, longpass and etalon filters are the same as used in Section 4.2. Aspheres and parabolic mirrors are placed on XYZ translation stages. The first waveguide rests on an X translation stage and the second on XZ stages. Each crystal is independently temperature stabilized for optimal phase matching. Waveplates in the 854 nm input path enable preparation of arbitrary input polarization states. Waveplates (plus polarizing beam splitter - PBS) in the 1550 nm output path enable the polarisation measurement basis to be changed arbitrarily.

difference acquired by different polarisation components in the setup is much smaller than the coherence length of both lasers used in this work as well as ion-produced photons in future work.

### 4.3.2 Results

#### 4.3.2.1 Efficiency and noise, at the single-photon level

To characterise the device, 854 nm laser light is injected with an average of 10 kHz photons to mimic the ion source. The power in each polarisation component of the pump is set to both maximise and balance the conversion efficiency for each polarisation component of the 854 nm light (approximately 200 mW of the relevant pump polarisation component in-coupled into each waveguide). When injecting V (H) polarised 854 nm light, telecom photons are detected at a rate of  $304 \pm 6$  Hz ( $302 \pm 6$  Hz) without polarisation analysis. This corresponds to a total efficiency of  $0.304 \pm 0.006$  ( $0.302 \pm 0.006$ ) when

removing detector inefficiency. That is, the probability of obtaining a fibre-coupled telecom output photon is  $\sim 0.30$  for both polarisations. The total measured (noise) count rate, when blocking the input 854 nm light, is  $7.6 \pm 0.4$  Hz, yielding a device signal to noise ratio of  $\sim 40$ . That noise count rate corresponds to a fibre-coupled telecom NPR of  $58 \pm 4$  Hz, when subtracting dark counts and removing detector inefficiency.

#### 4.3.2.2 Polarisation-preservation

To determine the extent to which the polarisation is preserved, as it is converted from 854 nm to 1550 nm, we perform process tomography [32]. Specifically, the 6 standard basis states for polarisation qubits are injected (horizontal, vertical, diagonal, antidiagonal, right- and left-circular) using waveplates in the 854 nm input path (fig. 4.6). For each input state, we project the output state successively onto each of the 6 basis states using waveplates and a polarizer in the 1550 output path, before single photon detection. From these measurements, the process matrix  $\chi_{ij}$  is reconstructed via an optimisation to find the most likely process to have generated the data (maximum likelihood estimation [112]). The process matrix describes the process  $\varepsilon$  applied to any input polarisation density matrix  $\rho$  via  $\varepsilon(\rho) = \sum_{ij} \chi_{ij} O_i \rho O_j^\dagger$ , where  $O_k$  are a set of operators which form a basis for the set of operators on the polarisation qubit state space. We choose the basis  $\{O_1, O_2, O_3, O_4\} = \{I, Z, X, -iY\}$ , corresponding to the identity and standard Pauli operators, respectively. To quantify polarisation-preservation, we maximise the  $\chi_{11}$  (identity) element of the reconstructed process matrix when allowing for arbitrary unitary operations (via a simple numerical search), obtaining a value of  $0.93 \pm 0.01$ : this is the minimum fidelity with which any input polarisation state is translated through the device and detected, up to a fixed known unitary operation, and is more than sufficient to preserve polarisation entanglement between ion and photon, as discussed in the following section. We find that a fidelity of  $0.95 \pm 0.01$  would be achieved when accounting for the measured NPR and DCR. The remaining infidelity is attributed to errors in the angular settings of waveplates by less than a degree.

## 4.4 FUTURE APPLICATIONS: LONG-DISTANCE TRANSMISSION.

In this section we consider future possibilities for long distance ion-photon entanglement based on current progress in trapped ions setups, commercial fibre technology and our photon converter and telecom detector presented above. Converting photons from 854 nm to 1550 nm offers a reduction in attenuation in optical fibre from 3 dB/km to 0.2 dB/km, respectively. When accounting for the finite 30% efficiency, one finds that our conversion system offers an improved rate of photon

transmission for all fiber lengths greater than 1.9 km. The advantage becomes profound for longer distances: over 50 km (100 km) of fiber, the transmission probability using our device would be 3% (0.3%), compared to  $1 \times 10^{-13}\%$  ( $1 \times 10^{-28}\%$ ) at 854 nm.

Using photons to distribute entanglement between remote network nodes is an important task in quantum networking. We are interested therefore in assessing the distance over which our conversion and detection setup could allow for entanglement to be detected between a photon and an ion. To answer this question, we consider the case where the ion emits 854 nm photons on demand, at a rate of 10 kHz and in the maximally entangled state  $(|g, H_{854nm}\rangle + |e, V_{854nm}\rangle) / \sqrt{2}$ , where  $g$  ( $e$ ) are orthogonal electronic states of the ion [31]. Next, we apply a modified version of the process matrix describing our converter to the photon part of the entangled state. The process matrix is modified in the sense that it is reconstructed from experimental data after subtracting detector dark counts, leaving imperfection due to photon noise. Photon noise is treated separately from dark counts at this point, since the former attenuate at the same rate as photons from the ion through a subsequent optical fibre, while detector dark counts do not. Finally, we apply a second process to the photon state which accounts for the 30% conversion efficiency, transmission probability through optical fibre of length  $L$ , detection efficiency (10%) and dark counts at 1.8 Hz (modelled by a depolarisation channel weighted in proportion to transmitted signal). Entanglement in the final ion-photon state is quantified by the negativity [113], although other measures give equivalent results. The result is that entanglement between ion and photon is present up until 84 km of optical fibre. Beyond this distance, detector dark counts overwhelm the (imperfect) entanglement in the converted ion-photon state. For reference, after 84 km, telecom photons from the conversion process should be detected at a rate of 6.3 Hz, compared with the dark counts of 1.8 Hz, yielding a SNR of  $(6.3+1.8)/1.8 = 4.5$  (photon noise is negligible).

The achievable distance for ion-photon entanglement in our setup could be significantly extended by considering only those detection events that occur when the ion could have generated a photon. A generation rate of 10 kHz for photons from the ion allows for 100  $\mu$ s per photon, of which less than 20  $\mu$ s consists of the photon wave packet itself [31]. The remaining 4/5 of the time is allocated for reinitialising the ion after each attempt, during which time counts at the detector can be ignored, allowing the dark counts to be reduced to  $1.8/5 = 0.4$  Hz. With such a reduced dark count rate, the maximum achievable distance for the observation of ion-photon entanglement in our setup is 122 km.

Note that, under ambient conditions the polarisation in a 25 km telecom fibre spool is known to be passively stable over timescales of several minutes [110]. To correct for polarisation rotations in long fibres

between remote locations, one could consider periodic calibrations with classical fields, or even calibrating continuously using classical fields in parallel with the quantum signal: exploiting the narrowband nature of trapped-ion networking photons for filtering.

Transmission of light-matter networking photons through optical fibres many tens of kilometres long poses an interesting problem: the photon travel time eventually becomes longer than the minimum time between photons set by the generation rate. In our example we considered a 10 kHz generation rate, corresponding to a photon every 100  $\mu\text{s}$ , whereas the travel time over 84 km (100 km) is 420  $\mu\text{s}$  (610  $\mu\text{s}$ ). With a single ionic-qubit in a trap, one must wait to see if a generated photon is detected after the fibre, before attempting to generate another photon, or entanglement with the first photon will typically be lost. For single ion qubit experiments, the maximum generation rate is therefore limited by the photon travel time. With multiple ionic qubits in a trap, however, one could envisage different ways to overcome the photon travel time limit. For example, after generating a photon with which it is entangled, the state of the ion could be swapped into one of a collection of co-trapped ions, freeing up the original ion to generate a new photon without destroying entanglement with the first photon. First-step experiments in this direction have recently been performed [28].

#### 4.5 FIBRE-COUPLED WAVEGUIDES

A challenging part in setting up and maintaining our bulk-optic conversion systems is the misalignment of the beam paths over time. The above described conversion system is built in a temperature stabilized lab and after peaking up all couplings the total device efficiency degrades approximately 10% after an hour. So the whole setup has to be peaked up at least once every working day. Direct fibre-coupling to a waveguide could provide more stability. Also setting up such a system is much easier, since no free-space waveguide coupling and beam overlapping has to be achieved. Fibre-coupled waveguides also need overall less space.

The group of Martin Fejer in Stanford designed, developed and shipped to us fibre-coupled conversion chips for conversion of 854 nm to 1550 nm via DFG. The chip has buried waveguides, achieved with a reverse-proton-exchange process [114]. Unlike the ridge waveguides used in the experiments reported in the previous sections, buried waveguides only guide one polarization. The design layout data sheet for the chips can be found in Appendix A.3. These chips have two single-mode input fibres, one for the signal (854 nm) and one for the pump (1902 nm). These fibres are glued to a micro-fabricated adiabatic tapered coupler. This coupler contains two single-mode waveguides for the input fields which are then adiabatically tapered into one single-

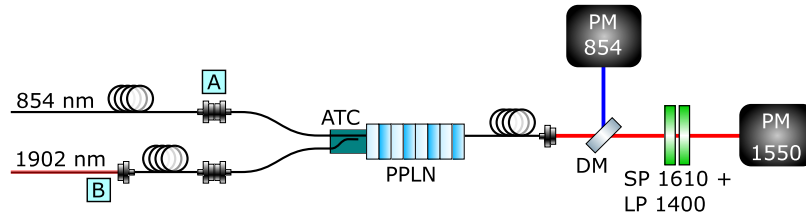


Figure 4.7: **Scheme for characterization of the fibre-coupled down conversion devices from our Stanford collaborators.** The fibre-coupled device has two input fibres, 854 nm (signal) and 1902 nm (pump), and one output fibre for the target light at 1550 nm. The 854 nm input is directly connected to a fibre-coupled diode laser. The 1902 nm light is fibre coupled and connected to the second input. An adiabatically tapered coupler (ATC) combines both light fields before they are coupled into the PPLN waveguide. The output fibre is connected to a collimator and split by a dichroic mirror (DM). The reflected 854 nm light can be directly measured. The transmitted 1550 nm light has to be filtered from the pump with a 1610 nm short pass (SP 1610) and a 1400 nm long pass (LP 1400).

mode waveguide, ready for injection into the conversion waveguide. The coupler is glued to the PPLN conversion chip, such that the single output waveguide mode of the taper couples into one of the PPLN waveguides. On the output facet a single-mode fibre for 1550 nm is glued directly.

As well as the conversion chips used in the previous sections, the Stanford chips have to be temperature stabilized to provide phase matching. Both a mount for the Stanford chips and a temperature stabilisation system which provides a temperature stability below  $0.1^\circ\text{C}$  using PID feedback controlled Peltier-elements were designed and built. More information and the design of this temperature controlling mount for the chips are given in Appendix A.4.

As mentioned before, due to the buried waveguides used in the Stanford chip design, only one polarization is guided through the waveguide. The polarization maintaining conversion scheme demonstrated in Section 4.3 works only when all polarizations are guided through the chip. Therefore, our polarization maintaining conversion scheme wouldn't work for the Stanford chips and another scheme would be needed. For these Stanford chips we only looked into the conversion of a fixed polarisation.

The experimental setup used to characterise the conversion efficiency is shown in Figure 4.7. The 854 nm input port of the fibre-coupled chip is connected with a fibre joiner to a fibre-coupled 854 nm laser, resonant with the  $|P\rangle$  to  $|D\rangle$  transition of  $^{40}\text{Ca}^+$ . The 1902 nm pump light from the fibre laser is fibre coupled and connected with a fibre joiner to the 1902 nm input of the fibre-coupled device. The output fibre of the chip is directly connected to a collimator. The free space output light is then separated on a dichroic mirror into a

854 nm path and a 1550 nm path. The reflected 854 nm light can be directly measured with a power meter since the dichroic mirror acts as a filter for 854 nm. A short pass at 1610 nm and a long pass at 1400 nm only transmits the out-coupled 1550 nm light in the transmitted path enabling direct measurement of the converted 1550 nm light with a power meter. The input power of the 854 nm light is  $45 \mu\text{W}$  at point A of Figure 4.7 directly before the input fibre joiner. The 1902 nm input was measured at point B before the input fibre coupling. The coupling efficiency of the 1902 nm light into the fibre was measured to be 80%. The out-coupling efficiency for the 1550 nm light from the fibre to free-space was measured to be 83% limited by a non-optimal collimator (60FC-4-M8-10). This coupler was not anti-reflection coated for 1550 nm light.

The measured conversion efficiency, as a function of the input pump power, for the chip C4 which has a length of 67 mm (data sheet Appendix A.3), is presented in Figure 4.8. The maximum conversion efficiency, measured for an 1902 nm pump power inside the input fibre of 360 mW, is  $0.44 \pm 0.01$ . Both Figure 4.8 and the maximum conversion efficiency have been corrected for the known coupling losses described in the previous paragraph. Under those conditions only  $1.3 \pm 0.3\%$  of the in-coupled 854 nm power was measured at the output. Meaning 98.7(3)%, which we call the signal depletion, of the in-coupled 854 nm light is either converted to 1550 nm or lost by transmission and coupling losses. This close to 100% signal depletion indicates a high spatial beam overlap of the two in-coupling beams. The signal depletion observed for the ridge waveguides (Section 4.2.2) was  $22 \pm 1\%$ , showing how much better the fibre-coupled chips perform in this parameter.

Despite the observed near-perfect signal depletion, the conversion efficiency of the fibre-coupled waveguides is maximally 44%. For the free-space coupled device in Section 4.2.2 we measured a conversion efficiency of  $0.46 \pm 0.01$ . We expect that the lower conversion efficiency compared to the signal depletion is caused by the coupling and transmission losses in the whole device. One important problem we found was temperature dependent coupling losses. Due to geometrical restrictions the oven heats the nonlinear crystal only, not the coupler. The set-temperature of around  $74.4 \text{ }^\circ\text{C}$  is much higher than room temperature. During operation the coupling losses change due to the heating of the coupler caused by the hotter crystal. This leads to a long settle time of a few hours until the conversion efficiency stabilises, which makes the optimization of the set-temperature hard. A new oven design, which heats both the crystal and the coupler would make the temperature adjustment easier.

The Stanford devices have not yet been used with single photons, since the free-space setup with ridge waveguides has similar efficiencies and offers a polarisation-insensitive process.

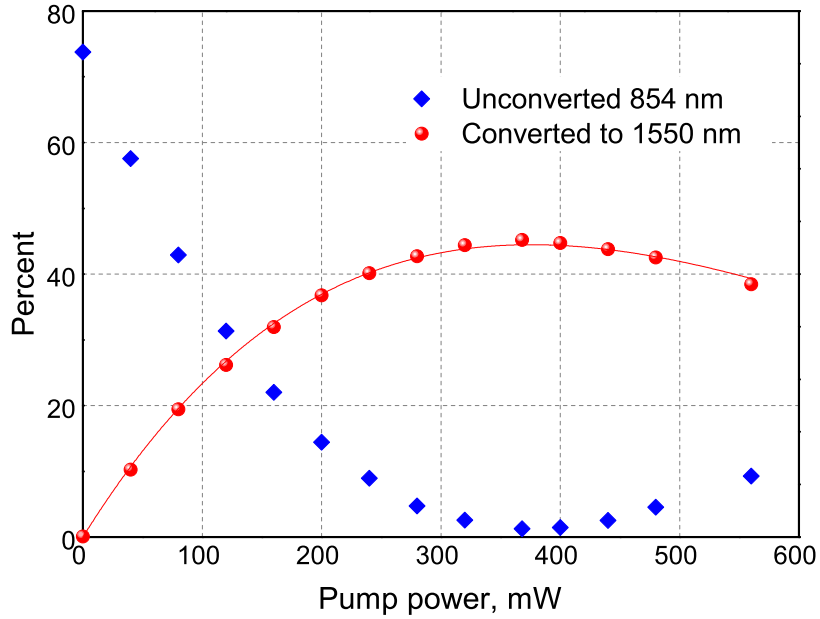


Figure 4.8: **Conversion efficiency of fibre-coupled Stanford conversion chip as a function of pump power.** Solid red spheres: conversion efficiency to 1550 nm. Solid red line: theoretical fit by the function  $\eta = A \cdot \sin^2(\sqrt{\eta_{nor} P_p L})$  (Equation 2.39) with fitting parameters  $A = 0.44$ ,  $\eta_{nor} = 0.15 \text{ W}^{-1} \text{ cm}^{-2}$ . Filled blue diamonds: fraction of remaining 854 nm light after the device.

#### 4.6 CONCLUSION AND DISCUSSION

We have demonstrated a polarisation-preserving photonic interface between the 854 nm transition in trapped  $\text{Ca}^+$  and the 1550 nm telecom C band. A total photon in to fibre-coupled telecom photon out efficiency of 30% was achieved, for a free-running photon noise rate of  $\sim 60$  Hz within our filtering bandwidth of 250 MHz. This highly efficient and low-noise converter will enable telecom conversion using existing trapped-ion sources of 854 nm single photons with a  $\text{SNR} > 1$ . In combination with near-future trapped-ion systems, our converter allows for the distribution of ion-photon entanglement over more than 100 km of optical fibre, opening up the possibility of building large-scale light-matter quantum networks. (see Chapter 5)

In principle, our device works equally as well in reverse: allowing 1550 nm photons to be converted to 854 nm via sum-frequency generation with the pump laser, which is used in Chapter 7.

For the experiments presented in this work it was not necessary to stabilise the frequency of the pump laser, since the conversion process bandwidth (several tens of GHz) is large compared to the frequency drift rate of our pump laser (few hundred MHz per hour). However, the spectral properties of the pump laser will be transferred onto the converted photon: whether that is important depends on the particular experiment that one wishes to perform with frequency converted

photons. For example, for the observation of ion-photon polarisation entanglement, frequency broadening of the converted photon should play no role. For entanglement swapping between remote nodes via one- or two-photon detection [83], frequency distinguishability between photons becomes important (see Chapter 7). For schemes where remote nodes absorb photons that have been frequency converted (e.g. conversion to telecom then back to 854 nm for absorption by a remote ion), special care may need to be taken to stabilise the pump laser frequency to minimise the spectral footprint on the photons. One could also consider using the temporal and spectral properties of the pump as a way to coherently modify those properties of the converted photons, to overcome bandwidth mismatches between remote quantum matter.

During the writing of [41] manuscript in 2018 we became aware of complimentary work to ours, in which polarisation-preserving conversion from 854 nm to 1310 nm (Telecom O band) was achieved using a single ridge waveguide scheme[94].



## TELECOM-WAVELENGTH ION-PHOTON ENTANGLEMENT

---

This chapter includes the observation of entanglement between an ion and a telecom-photon that travelled over 50 km of optical fibre. That result is published in [npj Quantum Inf 5, 72 \(2019\) \[41\]](#) and the authors are Martin Meraner (MM), Victor Krutyanskiy (VKru), Josef Schupp (JS), Vojtech Krcmarsky (VKrc), Helene Hainzer (HH) and Ben Lanyon (BPL). All authors contributed to the design, development and characterisation of the experimental systems. In particular, JS focused on the ion trap and optical cavity, MM on the photon conversion system, VKrc on the ion trap, HH on laser frequency stabilisation and VKru and BPL on all aspects. Experimental data taking was done by VKru, VKrc, MM and JS. Data analysis and interpretation was done by VKru, JS, MM and BPL. All authors contributed to the paper writing. The project was conceived and supervised by BPL.

This chapter presents both an extended discussion of the work that is summarized in [\[41\]](#) and new experimental results in which 100 km ion-photon entanglement is observed. At time of writing the 100 km results are unpublished. Experimental data taking was done by VKru, VKrc and MM. Specifically sections [5.1](#) to [5.3](#) are, except for minor modifications, taken directly from [\[41\]](#). Section [5.4](#) contains an as-yet-unpublished results obtained after several major improvements were made to our setup. Section [5.5](#) presents a conclusion to the chapter.

### 5.1 INTRODUCTION

Envisioned quantum networks [\[3\]](#) consist of distributed matter-based quantum nodes, for the storage, manipulation and application of quantum information, which are interconnected with photonic links to establish entanglement between the nodes. While the most ambitious form of a quantum network is a collection of remote quantum computers, far simpler networks with a handful of qubits at each node could already enable powerful applications in quantum enhanced distributed sensing, timekeeping, cryptography and multiparty protocols [\[6\]](#).

Entanglement has been achieved between two atoms in traps a few ten meters apart [9], between two ions in traps a few meters apart [10] and recently between two nitrogen-vacancy centres 1.3 km apart [11]. In these experiments, photon-matter entanglement is first generated, then detection of one or two photons heralds remote matter-matter entanglement (entanglement is “swapped” from matter-light to matter-matter).

A current goal is to significantly scale up the distance over which quantum matter can be entangled to a hundred kilometres or more, which are practical internode spacings to enable large-scale quantum networks. Some key challenges to entangling matter over such distances are now described. First, the aforementioned matter systems emit photons at wavelengths that are strongly absorbed in optical waveguides (such as optical fibre), limiting the internode distance to a few kilometers. For example, in the present work 854 nm photons are collected from a trapped atomic ion. While the  $\sim 3$  dB per km losses suffered by 854 nm photons through state-of-the-art optical fibre allows for few kilometre internode distances, transmission over 50 km of fibre would be  $10^{-15}$ . Single-photon quantum frequency conversion to the telecom C-band (1550 nm) would offer a powerful solution: this wavelength suffers the minimum fibre transmission losses ( $\sim 0.18$  dB per km, yielding 10 % transmission over 50 km) and is therefore an ideal choice for a standard interfacing wavelength for quantum networking. Photons from solid-state memories [115], cold gas memories [98, 116], quantum dots and nitrogen-vacancy centres [117] have been converted to telecom wavelengths. Frequency conversion of photons from ions has very recently been performed, including to the telecom C-band (without entanglement) [118], to the telecom O-band with entanglement over 80 m [18] and directly to an atomic Rubidium line at 780 nm [119]. The use of photon conversion to extend the distance over which light-matter and matter-matter entanglement can be distributed has not previously been achieved.

A second challenge to entangling matter over tens of kilometres is to preserve entanglement when such long photonic channels are involved. Uncontrolled decoherence processes that act on the photon as it travels along its path, and those that act on the quantum matter during the photon travel time, can easily destroy entanglement. For example, the entanglement-carrying photon signal can be overwhelmed by added photon noise from the photon frequency conversion process or dark counts of the photon detectors. The inter-node photon travel time also imposes a minimum coherence time for matter, which for e.g. 50 km of optical fibre is already significant at 250  $\mu\text{s}$  (and 500  $\mu\text{s}$  to allow for the classical signal of a successful herald to return). Moreover, quantum networking applications require distributed entanglement of a quality above certain thresholds, for which the required matter coherence times and photon signal to noise ratio are far more challenging.

A third challenge comes again from the photon travel time. The shortest time required to entangle remote matter (or indeed light) in two places is the light travel time between them. The 500  $\mu\text{s}$  wait time over 50 km of optical fibre yields a maximum attempt rate of only 2 kHz: one must wait 500  $\mu\text{s}$  to learn if an individual attempt to distribute remote entanglement has been successful. To achieve practical entanglement distribution rates in the face of such a restriction, one can work on achieving a high probability for individual attempts to succeed and (or) to run many attempts in parallel (as discussed later).

In this Chapter the achievement of entanglement between a trapped-ion qubit and a photon that travelled over first 50 km of optical fibre, and then an extension to 100 km using a improved setup are reported. These results are achieved by combining the ion-cavity system of Section 3.2 and the photon conversion system of Section 4.

The Chapter is organised as follows. In 5.2 a overview of the experimental setup and methods is given. In 5.3 the tomographically-reconstructed entangled state, of the ion qubit and photon polarisation qubit after 50 km, is presented and the achieved fidelity, efficiency and rate are analysed. Also, the ion qubit is shown to provide a quantum information storage time (coherence time) of more than 20 ms. Finally, in 5.4 improvements to the setup are described and the observation of 100 km ion-photon entanglement is presented

## 5.2 EXPERIMENTAL DETAILS AND METHODS

### 5.2.1 Overview of the experimental setup

The complete setup for the 50 km ion-photon entanglement experiment with every optical element is shown in Figure 5.1. As detailed in Section 3.2, our network node consists of a  $^{40}\text{Ca}^+$  ion in a radio-frequency linear Paul trap with an optical cavity that enhances photon collection on the 854 nm electronic dipole transition (see Figure 5.2). A Raman laser pulse at 393 nm triggers emission, by the ion, of a photon into the cavity via a bichromatic cavity-mediated Raman transition (CMRT) [31], as described in Section 3.5. Two indistinguishable processes are driven in the CMRT, each leading to the generation of a cavity photon and resulting in entanglement between photon polarisation and the electronic qubit state of the ion of the form  $1/\sqrt{2} (|D_{J=5/2, m_j=-5/2}, V\rangle + |D_{J=5/2, m_j=-3/2}, H\rangle)$ , with horizontal ( $H$ ) and vertical ( $V$ ) photon polarisation and two metastable Zeeman states of the ion ( $D_J, m_j$ ). The total measured probability of obtaining an on-demand free-space photon out of the ion vacuum chamber (entangled with the ion) is  $P_{out} = 0.5 \pm 0.1$ , as described in Section 5.3.1, enabled by the novel low-loss cavity in our setup.

The CMRT yields an entangled state with a frequency-degenerate photon qubit (the two polarisation components have the same fre-

quency to within the cavity linewidth [31]), providing a significant benefit for long distance networking: the phase of the light-matter entangled state does not depend on the time at which the photon detection event occurs at a given distance from the ion. Photon detection time fluctuates due to the intrinsic finite temporal extent of the photon wavepacket and in the case of optical path length changes, which could be significant over tens of kilometres of deployed optical fibre. Our photons are generated over several tens of microseconds, with a corresponding bandwidth of tens of kilohertz. This unusually narrow bandwidth allows for strong frequency filtering, which we exploit in the photon conversion process and could have further benefits in future deployed networks, e.g to enable co-propagating classical and quantum light. Furthermore, the corresponding photon coherence-length is potentially thousands of meters, allowing for essentially path-length-insensitive entanglement swapping between remote ions via Hong-Ou-Mandel interference [10, 120, 121].

Single-mode fibre-coupled photons from the ion are injected into a polarisation-preserving photon conversion system (previously characterised using classical light in Chapter 4). In summary, a  $\chi^{(2)}$  optical nonlinearity is used to realise difference frequency generation, whereby the energy of the 854 nm photon is reduced by that of a pump-laser photon at 1902 nm, yielding 1550 nm. Two commercially-available free-space and crossed PPLN ridge waveguide crystals are used, one to convert each polarisation, in a self-stable polarisation interferometer. The total fibre-coupled device conversion efficiency here is  $25 \pm 0.02 \%$ , for an added white noise of 40 photons/s, within the filtering bandwidth of 250 MHz centred at 1550 nm. As discussed in Section 2.3, the 854 nm line in  $^{40}\text{Ca}^+$  is almost unique amongst trapped-ion transitions in its potential for low-noise, highly-efficient single-step frequency conversion to the telecom C band.

Following conversion, the telecom photon is injected into a 50.47 km ‘SMF28’ single-mode fibre spool with 0.181 dB per km loss ( $10.4 \pm 0.5\%$  measured total transmission probability). The spool is not actively stabilised in any way, but stored inside a plastic box to reduce the amplitude of thermal and acoustic fluctuations present in the lab. Polarisation dynamics in an unspooled fibre could be actively controlled using methods developed in the field of quantum cryptography (e.g. [110]). Finally, free-space projective polarisation analysis is performed and the photon is detected using a telecom solid-state photon detector with an efficiency of  $0.10 \pm 0.01$  and free-running dark count rate of  $\sim 2$  counts per second (cps). Measurement of the ion-qubit state is performed conditional on the detection of a 50 km photon within a  $30 \mu\text{s}$  time window: the Zeeman ion qubit is mapped into the established  $^{40}\text{Ca}^+$  optical quadrupole clock qubit [35] via laser pulses at 729 nm, followed by standard fluorescence state detection.

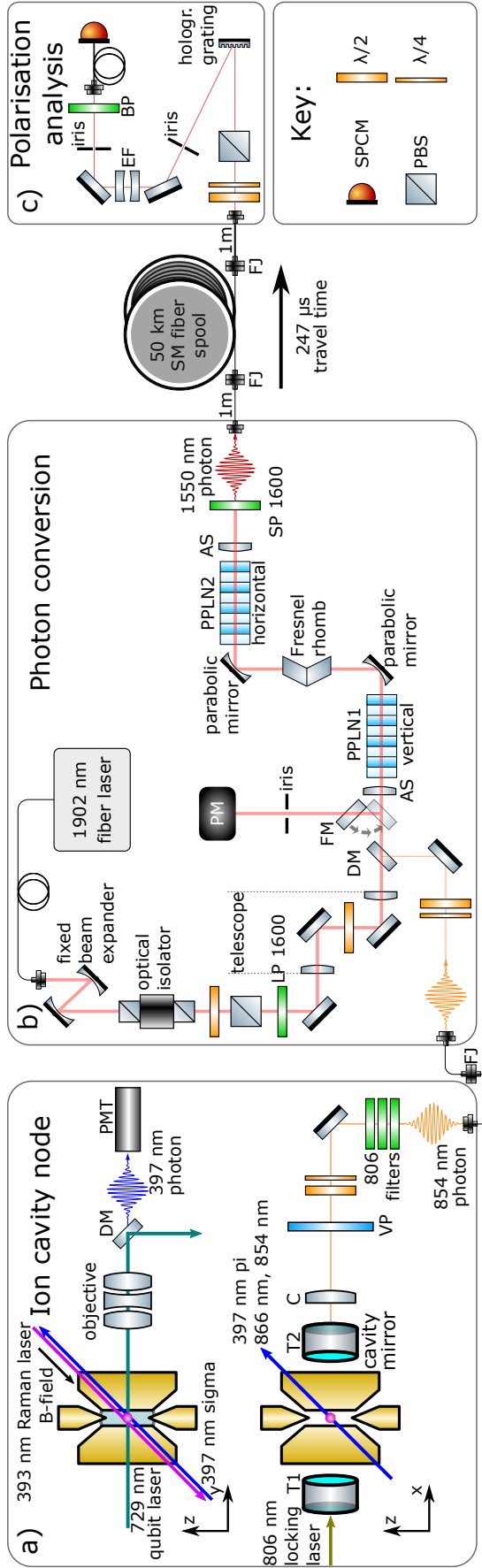


Figure 5.1: **Experimental setup for the 50 km ion-photon entanglement experiment.** All elements used for the experiments are shown in this diagram. Detailed description to the single parts can be found in the next figures. Figure 5.2 describes the ion cavity node, Figure 5.3 the conversion setup and Figure 5.4 the polarisation analysis. The used 50 km fibre spool (Corning SMF-28 ultra, Fiontec) is placed inside a cooling box to prevent temperature changes. For the 100 km entangling experiment in Section 5.4.3 we added a second 50 km spool, which was due to space limitations outside the cooling box.

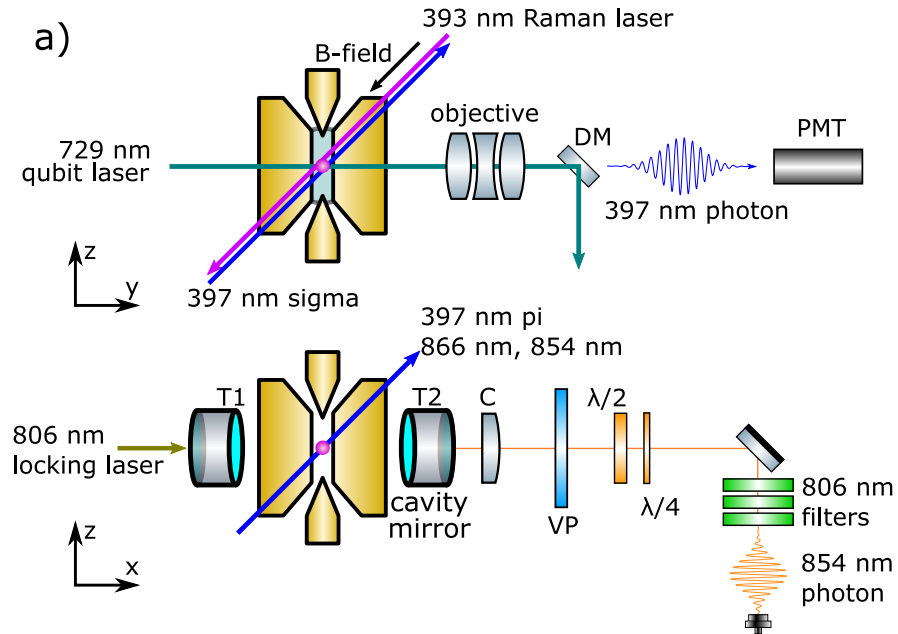


Figure 5.2: **a) Ion cavity node.** A single atomic ion (red sphere) in the centre of both a 3D radio-frequency (RF) linear Paul trap (gold electrodes) and an optical cavity. The two smaller electrodes are ‘end-caps’ held at DC voltage. The two larger electrodes are driven with RF, two additional larger electrodes exist but are not shown. Two cross sections are depicted: **Along the cavity axis (top)**, showing: the  $\approx 4$  Gauss DC magnetic field (quantisation axis) generated by rings of permanent magnets; the circularly-polarised Raman laser for generating 854 nm cavity photons; the 729 nm laser for ion-qubit manipulation and measurement (see Section 5.5); a custom objective (NA = 0.289,  $f = 66.8$  mm, lying in an inverted viewport) for collecting spontaneously scattered 397 nm photons for ion-qubit state detection (PMT: Photo multiplier tube). The circularly polarised 397 nm sigma beam is used for optical pumping. **Perpendicular to the cavity axis (bottom)**: Following a Raman pulse, an 854 nm cavity photon exits the cavity via the right mirror with transmission T2 with probability  $\geq 0.5 \pm 0.1$  (see Section 5.3.1). The photon then passes the following elements: in-vacuum collimating lens C; vacuum chamber viewport VP; waveplates (for polarisation analysis of 854 nm photon, see Section 5.3.2); 3 filters to remove the 806 nm laser light to which cavity length is continuously and actively stabilised (see Section 3.2). The 854 nm photon is then coupled into a single mode fibre (non-polarisation maintaining) leading to the photon conversion setup (total length 10 m with fibre-fibre joiner, FJ). The 397 nm pi beam is used for Doppler cooling and ion-qubit state detection.

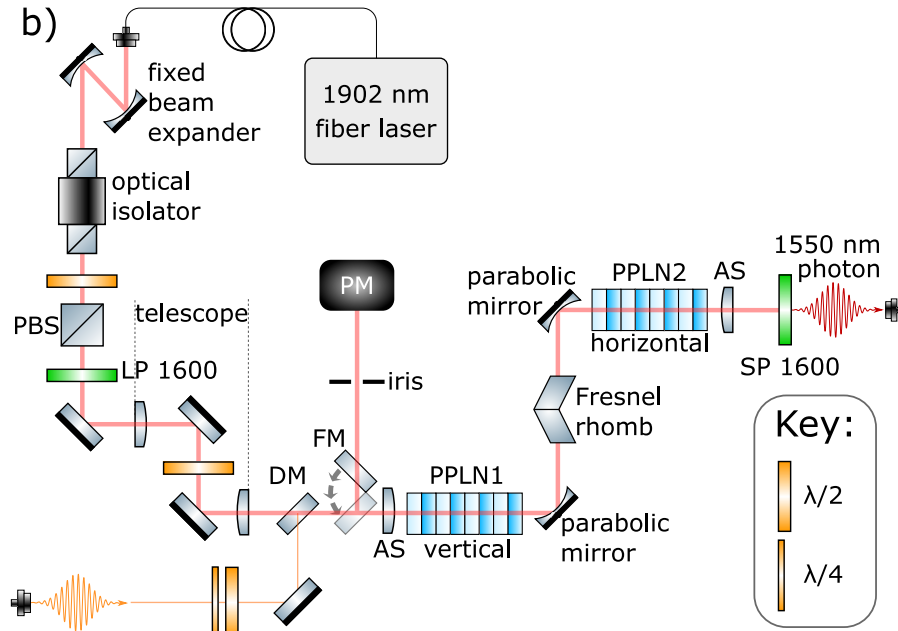


Figure 5.3: **b) Photon conversion.** The injected 854 nm photon passes waveplates (used for system setup with classical light) and is overlapped with 1 W of 1902 nm laser light (Tm-doped fibre laser, AdValue Photonics AP-SF1-1901.4-01-LP) on a dichroic mirror (DM) and free-space coupled into one of the ridge waveguides of temperature-stabilised PPLN<sub>1</sub> using an asphere (AS, 11 mm, positioned by an XYZ translation stage). The 1902 nm input path includes: beam expander to reduce the beam diameter so as to fit an optical isolator; waveplate and polariser to tune the power; longpass filter (LP 1600 nm) to reduce 1500 nm photons produced directly by the fibre laser; simple telescope to optimise the coupling efficiency to the waveguide. A flip mirror (FM) before PPLN<sub>1</sub>, and subsequent classical power meter (PM) allows for verifying spatial overlap of the 1902 nm and 854 nm fields (with classical 854 nm light). Gold parabolic mirrors are used to focus/collimate all fields ( $f = 15$  mm). A Fresnel rhomb is used to flip polarisation for subsequent conversion of the qubit's other polarisation component in PPLN<sub>2</sub>. SP 1600 nm: shortpass filter (OD<sub>5</sub> at 1902 nm).

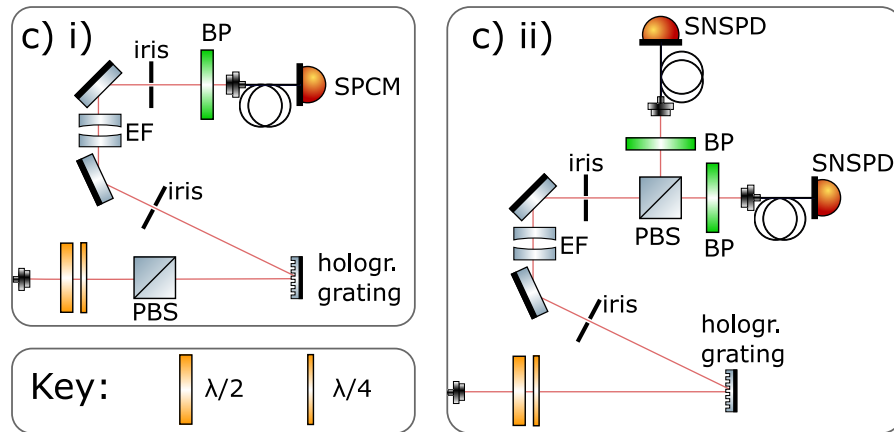


Figure 5.4: **c) i) Polarisation analysis for the results in Section 5.3.** Hologr. grating: volume holographic Bragg grating (reflection bandwidth 0.2 nm [25 GHz], 95% reflection); EF: air-spaced Fabry-Pérot cavity (250 MHz linewidth, 12.5 GHz free spectral range, peak transmission 95% at 1550 nm, extinction  $10^3$ ); BP: bandpass 1550 nm filter (12 nm bandwidth and 95% transmission). The total conversion efficiency given in the main text ( $25 \pm 0.02$  %) is the probability of getting a 1550 nm photon (from the ion) in the fibre immediately before the single photon counting module (SPCM, InGaAs ID230, IDQuantique), given a fibre-coupled 854 nm input photon in the input fibre to the conversion setup, in the case where the 50 km fibre spool is removed and the waveplates in the polarisation analysis are set to maximise subsequent PBS transmission. **c) ii) Polarisation analysis for the improved results in Section 5.4.3.** The filtering network is the same as in i). The PBS was moved after the narrow band filtering and both outputs of the PBS (transmission and reflection) are here analysed with superconducting nanowire single photon detectors (SNSPD's).

### 5.2.1.1 Polarisation maintaining single photon conversion setup

Details about the operation and characterisation of the conversion setup (using classical 854 nm laser light) can be found in Chapter 4 and [17]. Figure 5.3 provides more details about the pump laser path. The filtering network and the final filters employed are shown in Figure 5.4. Note that a long-pass filter, with 1440 nm cutoff, that was present in the first conversion experiment (Chapter 4) is now removed, since the 50 km fibre spool performs an equivalent task of attenuating weakly phased-matched frequency-doubled pump laser light. We now provide a short summary of the conversion setup for clarity.

Difference frequency generation (DFG) is used to convert a 854 nm photon to 1550 nm via a  $\chi^{(2)}$  nonlinearity in a 48 mm long PPLN ridge waveguide-integrated chips<sup>1</sup>  $(854 \text{ nm})^{-1} - (1902 \text{ nm})^{-1} \approx (1550 \text{ nm})^{-1}$ . Two chips are used in series to convert orthogonally-polarisation components of the 854 nm photon sequentially (while the ridge guides support all polarisations, they each convert only one polarisation component). Specifically, in our system, each waveguide converts the vertically-polarised components of the fields. The Fresnel rhomb between the chips (equivalent to a broadband half-waveplate) acts to rotate horizontal to vertical polarisations of all three fields, such that the second chip converts the orthogonal polarisation components to the first chip (see description in Chapter 4).

200 mW of vertically-polarised 1902 nm pump is required in each PPLN for maximum conversion efficiency. To achieve this we send in a total of  $\approx 1 \text{ W}$  of 1902 nm light at the input to PPLN<sub>1</sub>, with polarisation set to achieve a balanced and maximum conversion efficiency in each PPLN chip.

For extracting the single telecom photon at the output, a filter network consists of a short-pass (OD5 for 1902 nm, cutoff 1600 nm) for reducing the pump power, a volume holographic Bragg grating (bandwidth 0.2 nm) and an etalon (bandwidth 250 MHz) for reducing the 1550 nm noise photons from anti-Stokes Raman scattering, yielding 40 cps photon noise after the filtering network with optimal pump power.

In Chapter 4 and [17] results from a detailed study of the photon noise introduced by our photon convertor is presented. In summary, the dominant source of photon noise around 1550 nm is Anti-Stokes Raman (ASR) scattering of the pump laser: the process whereby pump laser photons at 1902 nm gain energy (get up-shifted to telecom) by scattering with existing phonons inside the conversion waveguide. The ASR scattering (added photon noise) in our converter is spectrally white at telecom and can thus be reduced by narrowing the output filtering bandwidth. With this setup we achieve  $4 \pm 2 \text{ Hz}$  added photon noise counts before detection for a filtering bandwidth of 250

---

<sup>1</sup> produced by NTT electronics

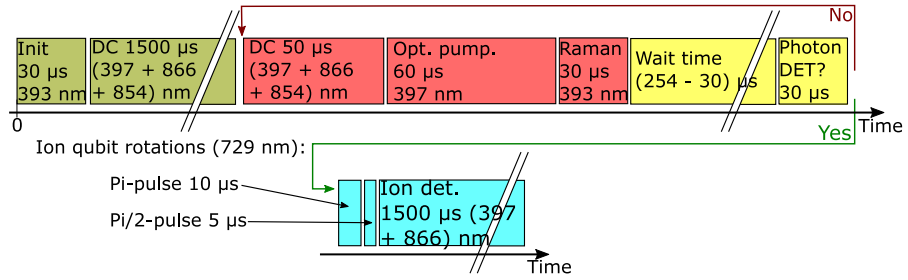


Figure 5.5: **Laser pulse sequence for the experiment.** The starting sequence (shown in green) consists of an initialisation laser pulse for intensity stabilisation (Init) and Doppler cooling (DC). The loop (shown in red and yellow) consists of additional Doppler cooling (DC), optical pumping, a (photon generation) Raman pulse, a wait time as the photon travels through the 50 km fibre to the detector and a 30  $\mu\text{s}$  detection window. If the photon detector clicks within this window, ion qubit manipulation and state detection (shown in blue) are performed, otherwise the loop repeats.

MHz, far from the ion-photon linewidth of 0.1 MHz (so narrower filtering would be possible without compromising the signal strength of the photon from the ion, but is unnecessary in the sense that the current noise rate does not compromise our ability to see ion-photon entanglement). Note that the low noise achieved in our system was enabled by careful choice of initial ion-photon wavelength, allowing for a broad spectral separation between pump laser wavelength and 1550 nm (and therefore minimal ASR noise at telecom). As discussed in section 5.3.2, imperfections introduced by the converter into the ion-photon entangled state are consistent (to within statistical uncertainty) with the expected (independently-measured) effects of detector dark counts and added photon noise. That is: no other source of error (e.g. imperfect polarisation preservation) could be distinguished within statistical uncertainty. For a detailed analysis of the polarisation preservation of the converter see Chapter 4 and [17].

### 5.2.2 Pulse sequence for 50 km experiment

A schematic figure of the experimental sequence is given in Figure 5.5, which will help to follow the coming explanation. First, a 30  $\mu\text{s}$  ‘initialisation’ laser pulse at 393 nm is applied, measured by a photodiode in transmission of the ion-trap chamber, which allows for intensity stabilisation of the subsequent 393 nm photon generation Raman pulse via a sample and hold system. The initialisation pulse is followed by a 1500  $\mu\text{s}$  Doppler cooling pulse. For the cases when the initialisation pulse produced a photon, an 854 nm laser pulse together with the Doppler cooling clears out the unwanted population from the  $D_{J=5/2}$  states.

Next, a loop starts in which single photons are generated (see Figure 5.5). This loop consists of an additional Doppler cooling pulse (50  $\mu\text{s}$ ), optical pumping to the  $S = S_{J=1/2, m_j=-1/2}$  state via circularly polarised 397 nm ‘sigma’ laser light (60  $\mu\text{s}$ ), and a 393 nm photon generation Raman pulse (30  $\mu\text{s}$ ). This is followed by a (247 – 30)  $\mu\text{s}$  wait time for the photon to travel through the 50 km fibre and a subsequent photon detection window. This sequence loops until a photon is detected or, due to programming constraints, a maximum of 40 repetitions is reached.

In the case of a photon detection (detector ‘click’), the state of the ion is measured. To perform an ion state measurement, the  $D' = D_{J=5/2, m_j=-5/2}$  electron population is first mapped to the  $S$  state via a 729 nm  $\pi$  pulse (Figure 3.4). That is, the D-manifold qubit is mapped into an optical qubit (with logical states  $S$  and  $D = D_{J=5/2, m_j=-3/2}$ ). In order to measure which of these states the electron is in, the standard electron shelving technique is used. We perform this measurement for a ‘detection time’ (397 nm photon collection time) of 1500  $\mu\text{s}$ , which is sufficient to distinguish bright (scattering) and dark (non-scattering) ions with an error of less than 1%. The aforementioned process implements a projective measurement into the eigenstates of the  $\sigma_z$  basis (Pauli spin-1/2 operator).

To perform measurements in other bases e.g  $\sigma_x$  ( $\sigma_y$ ), as required for full quantum state tomography, an additional  $\pi/2$  pulse on the  $S$  to  $D$  transition with a 0 ( $\pi/2$ ) phase is applied after the  $\pi$  pulse and before electron shelving is done, to rotate the ion-qubit measurement basis.

The 247  $\mu\text{s}$  photon travel time through our 50 km fibre spool limits the maximum attempt rate for generating a photon from the ion to 4 kHz (2 kHz if the fibre was stretched out away from our ion to force an additional delay for the classical signal ‘photon click’ to return). Until photon detection occurs, photon generation is (Raman laser pulses are) performed every 453  $\mu\text{s}$ , yielding an attempt rate of 2.2 kHz.

The most time consuming part in the sequence is the ion state detection (1500  $\mu\text{s}$ ). In our 50 km ion-photon entanglement experiment most of the attempts are unsuccessful. To avoid unnecessary ion state detections, which otherwise reduce the achievable repetition rate, state detection is performed only in the case of successful photon detection or the maximum number of 40 attempts is reached (due to programming constraints). This conditional measurement of the ion-state was realized with an FPGA-based logic board (“conditional logic board”) in combination with digital inputs from the PulseBox. The layout of the conditional logic board is described in detail in the appendix A.2. The basic function of the conditional logic board is to signal the PulseBox if a photon from the Raman pulse was detected. The initial electric pulse shape of the used detector<sup>2</sup> has typical lengths

---

2 ID Quantique ID230

of  $\sim 100$  ns and appears directly when the photon was measured. The PulseBox itself is only capable of reading out a value at a specific time after the Raman process.

The conditional logic board has one of its digital inputs connected to the output of the photon detector, which we call 'photon in' (for the experiments in 5.4.3 a second input was added). Two other digital inputs of the conditional logic board, the 'gate' and the 'reset', are each connected to a different digital output port of the PulseBox. The conditional logic board has only one digital output which is connected with a digital input of the PulseBox. The output of the conditional logic board remains at logical 0 (0 Volts), when no photon was detected and changes to logical 1 (3.3 Volts), when a photon is detected. After the read out by the PulseBox, this output is reset to logical 0. Specifically, an electronic pulse from the PulseBox to the 'reset' input of the conditional logic board triggers the reset. The 'gate' input allows the conditional logic board to react only on photon detection events that occur during a desired time window, which is set to be the expected photon arrival time. Due to programming constraints of the PulseBox, an upper bound of unsuccessful attempts of 40 was used in the 50 km experiment. Whenever that threshold was reached, the sequence proceeds with ion state detection. These unsuccessful measurements are ignored in later state analysis.

### 5.2.3 State characterisation

To reconstruct the ion-photon state, a full state tomography of the two-qubit system is performed. On the photon polarisation qubit side, the state is projected to one of 6 states (horizontal, vertical, diagonal, anti-diagonal, right circular and left circular) by waveplates and polariser. This is equivalent to performing projective measurements in three bases described by the Pauli spin-1/2 operators. For example, horizontal and vertical are the eigenstates of the Pauli  $\sigma_z$  operator. On the ion qubit side, measurement is performed in the three Pauli bases as described in Section 5.2.2.

For each of the 9 possible joint measurement bases (choice of photon basis and ion basis), the numbers of events corresponding to one of the four possible outcomes of these 2-qubit measurements are considered. We then divide the number of events recorded for each outcome by the total number of events recorded for the given basis (divide each number by the sum of four) and thus obtain estimates of the outcome probabilities. These probabilities are used to reconstruct the 2-qubit state density matrix by the Maximum Likelihood method described in [112]. The values of fidelity, concurrence and other measures are calculated from the reconstructed density matrix.

For statistical analysis (determining error bars in quantities derived from the reconstructed density matrix), the Monte-Carlo approach

was implemented [122]. Briefly, we numerically generate  $M = 200$  sets of 36 event numbers with Poissonian distribution and mean value equal to the experimental value for each of the 36 possible outcomes (9 measurements bases each with 4 outcomes). From these simulated event numbers we derive simulated outcome probabilities, the same way as we do for the experimental counts. Then we reconstruct  $M$  density matrices for this simulated data and for each one we calculate the quantities of interest (fidelity, concurrence). The error bars given in quantities represent one standard deviation in the widths of the distributions of these quantities over  $M$  simulated data sets. The final presented quantities are calculated from the density matrix that is reconstructed directly from the experimental data. The error bars are shown as centred on those values.

The fibre connections in the setup (short fibres and long fibre spool) rotate the photon-qubit state. We did not independently analyse the overall polarisation rotation caused by these fibres. Therefore, we do not detect Bell states, but rotated Bell states due to single qubit rotations. We quantify the state quality in terms of fidelity  $F^m$  defined as  $F^m = \left[ \text{Tr} \sqrt{\sqrt{\rho_{exp}} \rho_{max.ent.} \sqrt{\rho_{exp}}} \right]^2$ , where  $\rho_{exp}$  is the density matrix, reconstructed from the experiment data and  $\rho_{max.ent.}$  is the density matrix of the nearest maximally-entangled pure state. This nearest state is found by exposing a perfect Bell state to a single qubit unitary rotation and searching over the unitary parameters to find the ones that provide the best fidelity with the experimentally-obtained state. This unitary rotation doesn't effect the purity and concurrence. The density matrices presented in this chapter are obtained by applying the inverse of the obtained rotations to the experimentally-reconstructed state: bringing the state into the familiar Bell-state form.

## 5.3 RESULTS

### 5.3.1 Setup efficiency for the 50 km distanced entangling experiment

In this section information is presented on the efficiency with which photons are distributed in the 50 km experiment and the sources of photon loss. The total probability that a Raman photon generation pulse leads to a photon click after 50 km is  $5.3 \times 10^{-4}$  (after summing up the outcomes of all polarisation projections). Together with an attempt rate of 2.2 kHz this yields to a click rate of  $\sim 1$  cps.

The total probability of obtaining an on-demand free-space photon out of the ion vacuum chamber is  $P_{out} = 0.5 \pm 0.1$ . This value is inferred from the measured efficiency with which we detect single-mode fibre-coupled (ion-entangled) photons at 854 nm (before the conversion stage), after correcting for the measured 1st fibre-coupling stage efficiency and the known 854 nm photon detector efficiency. The uncertainty in  $P_{out}$  is dominated by the uncertainty in the 1<sup>st</sup> fibre-coupling

stage efficiency (see table 5.1), which could be reduced in future. The overall efficiency of the frequency-conversion setup, including spectral filtering, is  $0.25 \pm 0.02$ , measured with classical 854 nm light. For a detailed description see Chapter 4. A short overview of the contributing photon losses are summarised in table 5.1. Multiplying all the transmissions together leads to a total expected probability of detecting the photon after 50 km of  $(6.5 \pm 1.5) \times 10^{-4}$ , which is consistent to within one standard deviation with the measured value of  $5.3 \times 10^{-4}$ .

A total 50 km detection probability of 0.01 should be straightforward to achieve in the future. For example, superconducting nanowire telecom photon detectors with efficiencies of  $> 0.8$  and dark count rates of  $< 10$  cps (see 5.4.1) are commercially available. Since taking the data presented in this experiment, we have improved the 1st fibre-coupling stage efficiency to  $0.9 \pm 0.1$  and further improvements should be possible. These changes alone are sufficient to achieve a total 50 km efficiency above 0.01.

The efficiency  $P_{out}$  in our setup is limited by losses in our mirror coatings to  $P_{out}^{max} = 0.73 \pm 0.03$ . Numerical simulations show that it should be possible to reach this value in our experiment [123] (that is, the probability of the ion emitting into the cavity mode could be near 100%) and recent experiments with our system show that  $P_{out} \approx 0.7$  is possible by cooling the ion close to the axial-mode ground state (and thereby enhancing the coupling strength of the cavity-mediated Raman transition, in comparison to the detrimental  $P_{3/2}$ -state spontaneous scattering rate). In [71] we obtain a single ion-entangled photon at the cavity output with a probability of  $P_{out} = 0.69(3)$ . The performance of our system is shown to saturate the upper limit to photon-collection probability from a quantum emitter in a cavity, set by the emitter's electronic structure and by the cavity parameters.

Finally, the achieved photon conversion stage efficiency is predominantly limited by unwanted excitation of higher-order spatial modes in the involved PPLN ridge waveguides [17]. A total device efficiency of 0.5 should be within reach with more careful attention to coupling into the guides and minimising other passive optical losses (e. g. avoiding unnecessary fiber joints). Combining all of the aforementioned improvements would lead to a total 50 km detection probability of nearly 0.03, close to the 50 km fibre transmission of 0.1.

Note that lower loss telecom fibres than the one used here are available (0.16 dB/km, Corning SMF-28 ULL) with a corresponding 50 km transmission of 0.16 and any improvement in fibre technology will further increase that value.

Location in the photon path	Efficiency
On demand photon out of cavity $P_{\text{out}}$	$0.5 \pm 0.1$
1 <sup>st</sup> single-mode fibre coupling	$0.5 \pm 0.1$
Telecom conversion stage (& filtering)	$0.25 \pm 0.02$
50 km fibre transmission	$0.104 \pm 0.005$
Telecom photon detector efficiency	$0.10 \pm 0.01$
Expected 50 km detection probability	$(6.5 \pm 1.6) \times 10^{-4}$

Table 5.1: Photon losses in our 50 km photon distribution experiment. See Figure 5.1 for the respective locations in the experimental setup.

### 5.3.2 Results for 50 km ion - telecom-photon entanglement

For quantification of the state, quantum state tomography was performed to reconstruct the two-qubit state (as described in 5.2.3). Figure 5.6 shows the measured wavepacket and the reconstructed density matrix after the 50 km fibre spool. The earliest measured photons from the wavepacket arrive 247  $\mu\text{s}$  after the beginning of the Raman-pulse, which corresponds to the travel time of light through a 50 km long optical fibre. A strongly entangled ion-photon state is observed over 50 km, quantified by a concurrence [38]  $C=0.73 \pm 0.05$  a purity  $\gamma = 0.75 \pm 0.4$  and state fidelity  $F^m=0.86 \pm 0.03$  with a maximally entangled state ( $C=1$ ).

Sources of infidelity in the experimentally-reconstructed ion-photon entangled state are now analysed. It will be shown that the 50 km ion-photon state infidelity ( $1 - F^m$ ) can be accounted for (to within statistical uncertainty) by taking into account background detector counts and imperfections in the initial ion-854 nm photon state output directly from the ion-cavity system.

Three additional independent experiments are performed, corresponding to state tomography of the ion-photon state at three different points in the photon path. First the ion-854 nm photon state was measured immediately at the cavity output (using free space polarisation analysis and two single-mode fibre-coupled 854 nm photon detectors, one at each port of a polarising beam splitter). Second, the ion-1550 nm photon state was measured immediately after conversion (with only a 1 m telecom fibre), referred to as 0 km distance. Third, the ion-1550 nm photon state after 50 km travel was reconstructed (result shown in Figure 5.6). The reconstructed state fidelities, with maximally entangled states, are presented in table 5.2 (bottom row ‘Experiment’).

The effect of background photon detector counts is analysed (defined as a detector click that didn’t result from a photon from the ion). For this, the background count rate is extracted from the measured counts in the tomography experiments by looking far outside the time window in which the ion-photon arrives, giving  $2 \pm 0.1$  cps for the

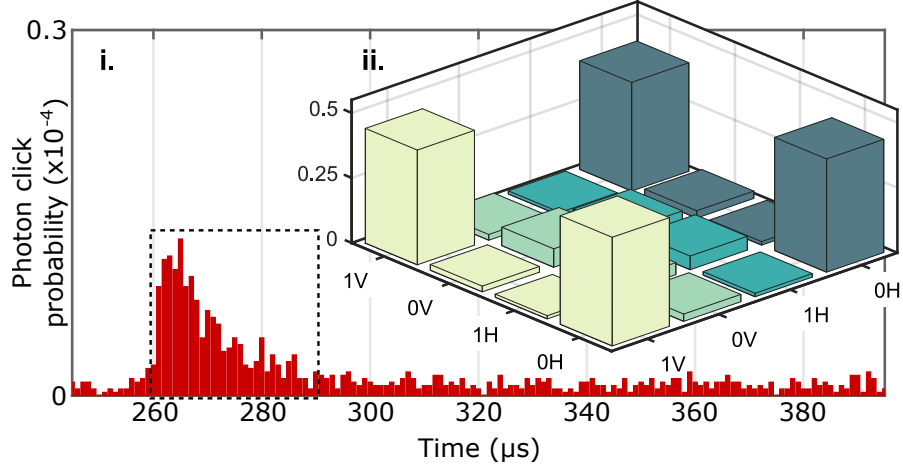


Figure 5.6: **Observation of ion-photon entanglement over 50 km of optical fibre.** **i.** 2D red bar chart: histogram of photon detection times (photon wavepacket in dashed box), following the generation of an 854 nm photon with a  $30 \mu\text{s}$  Raman laser pulse  $247 \mu\text{s}$  earlier, repeated at 2.2 kHz. Ion-photon state tomography is performed for photon detection events recorded in the dashed box (total contained probability  $P = 5.3 \times 10^{-4}$ ). **ii.** 3D bar chart: absolute value of experimentally-reconstructed density matrix of the telecom photonic polarisation qubit ( $H$  and  $V$  are Horizontal and Vertical, respectively) and ion-qubit state ( $|0\rangle = |D_{J=5/2, m_j=-3/2}\rangle$ ,  $|1\rangle = |D_{J=5/2, m_j=-5/2}\rangle$ ).

1550 nm photon at 50 km and  $10 \pm 1$  cps for the 854 photon, which are both in agreement with the telecom ( $1.9 \pm 0.15$  cps) and 854 nm ( $10.1 \pm 0.9$  and  $10.8 \pm 1$  cps) detectors' dark count rates (measured independently). For the 1550 nm photon at 0 km we get  $4 \pm 0.1$  cps, where the additional 2 cps background is produced by the photon conversion pump laser anti-Stokes Raman scattering which was shown in Chapter 4 and [17]. Note that this added noise is attenuated at the same rate as the photons from the ion over the 50 km, and so becomes a small contribution to the background compared to the intrinsic detector dark counts (which do not attenuate over distance).

The infidelity that the background counts would contribute when applied to a perfect maximally-entangled Bell state is simulated numerically. Specifically, the expected background count probability in our photon time-window is added to the expected measurement outcome probabilities for a perfect state as white noise, then a new 'noisy' state density matrix is reconstructed via Maximum Likelihood tomography. We call this approach 'Model 1', which simulates the effect of measured background counts only, and find that it explains the majority of the infidelity in the 50 km state (see Table 5.2).

In addition to the background counts, Model 2 takes the measured imperfect 854 nm ion-photon state into account. That is, the tomographically reconstructed ion-854 nm-photon state is used as the state

$F^m, \%$	854 nm @ 0 km	1550 nm @ 0 km	1550 nm @ 50 km
Model 1	99.5	96	86
Model 2	-	93	83
Experiment	$96.7 \pm 0.6$	$92 \pm 2$	$86 \pm 3$

Table 5.2: Comparison of modelled and measured ion-photon entangled state fidelities. Model 1: ideal Bell state subjected to background counts during photon qubit measurement. Model 2: Experimentally reconstructed 854 nm state affected by background counts.

to which background counts are added as with Model 1. The results, shown in table 5.2, show that background counts and imperfections in the initial 854 nm state explain the state infidelities to within statistical uncertainty.

Since the imperfections introduced into the ion-photon state by the converter are consistent with those expected from added photon noise and detector dark counts, any other sources of imperfections (e.g. polarisation contrast loss - see Chapter 4 for a detailed analysis) cannot be resolved above the  $\sim 1\%$  infidelity level.

Regarding infidelities in the initial ion-854 nm photon state: It is straightforward to show that the maximum fidelity of an arbitrary state  $\rho_{arb}$  with any pure state is given by the square root of the purity of  $\rho_{arb}$ , that is,  $F \leq \sqrt{\gamma}$ . The fidelity in this case is limited by the state purity ( $\gamma = 0.94 \pm 0.01$  for the 854 nm reconstructed state) meaning that only the imperfections leading to decoherence (or effective decoherence) need be considered. Possible error sources include errors in the 729 nm laser pulses used to determine the ion measurement basis, decoherence of the ion-qubit due to e.g. fluctuating magnetic fields and relative intensity fluctuations of the two frequency components in the Raman drive leading to a mixture of different states over the duration of the experiment. Identifying the size and relative contribution of these errors is beyond the scope of this work. The achieved fidelity at 854 nm is similar to that achieved in [31].

Therefore, we can summarize that the reduction in fidelity due to adding the QFC stage and 50 km spool can, within statistical uncertainty, be entirely explained by our telecom photon detector dark counts (2 cps).

### 5.3.3 Decoherence of the ion-qubit state

One of the functions played by matter in a quantum network is as a memory to store established entanglement, while new entanglement is being made or processed in other parts of the network. Decoherence processes in the matter qubit will limit the distance over which it is possible to distribute quantum entanglement (the distance a photon could possibly travel in the ‘coherence time’ of the matter qubit). In our

50 km experiment, the ion qubit is already stored for the 250  $\mu$ s photon travel time through the 50 km fibre, with no statistically significant reduction in the ion-photon entanglement quality (this was achieved by installing a mu-metal shield around the ion-trap vacuum chamber to attenuate ambient magnetic field fluctuations which directly change the energy spacing between the levels in which we encode our ion-qubit).

Additional tomographic measurements are performed to see how the ion-qubit decays over time. Specifically, state tomography is performed for increasing delays introduced between measurements of the telecom photon polarisation state (0 km fibre travel distance) and measurements of the state of the ion-qubit. This is equivalent to introducing an additional storage time for the ion-qubit. The results show that strong entanglement is still present after 20 ms wait time ( $F^m = 0.77 \pm 0.04$ ,  $C = 0.57 \pm 0.08$ ), the longest wait time employed. This already opens up the possibility of distributing entanglement over several thousands of kilometres (if the only limit was the speed of light) and the time to perform hundreds of single and multi-qubit ion quantum logic gates [124].

A dominant source of decoherence of our ion-qubit are uncontrolled energy-level shifts due to intensity fluctuations of the 806 nm laser field used to lock the cavity around the ion. Further attention to minimising the absolute size of these fluctuations should lead to entanglement storage times of more than  $\sim 100$  ms, limited by the lifetime of the metastable D state of the ion-qubit. Beyond this, the ion-qubit could be transferred to hyperfine clock transitions within different co-trapped ion species that offer coherence times of many seconds and longer [125]. Section 8.6 takes a closer look into the decoherence of the ion-qubit.

#### 5.4 RESULTS WITH IMPROVED SETUP

The results shown above are the first experiments that were done that combine the ion-trap and photon conversion system. Subsequently, multiple improvements were made to the setup which led to a significant increase in the photon detection efficiency. In this section the main improvements done are summarized. Following these improvements we repeated the measurements for ion - telecom-photon entanglement for 0 km and performed a long distance entanglement measurement. This time, because of the improved detection efficiencies, the distance was increased to 100 km.

### 5.4.1 Setup improvements

For improving the total photon detection efficiency, different stages of the photon path were optimized. The changes done to the setup starting from the beginning of the photon path to the end are described.

First, the ion was discovered to be approximately 0.5 mm away from the cavity waist, as described in Chapter 5 of [69]. Repositioning of the cavity - ion alignment reduced the cavity effective mode area by a factor of two, leading to a two times higher cooperativity  $C$ . Second, the single-mode fibre coupling efficiency of the photon leaving the cavity was improved from 0.5(1) to 0.82(5), by more careful attention to mode matching with lenses. Last, the single telecom photon detector was replaced by two telecom superconducting nanowire single photon detectors (SNSPD), one at each output of the polariser. A comparison of the performance of the old and new detectors is presented in table 5.3. With two single photon detectors, two bases of the photon state can be measured simultaneously. Therefore, only 3 waveplate positions are needed for full state tomography. The reconstruction of this data can be more challenging due to different path efficiencies and different detector efficiencies. In our experiment we still carried out measurements using 6 different waveplate positions (6 measurement settings). With these 6 measurements, every projection is measured twice, once at each detector. The outcomes for the same measurement basis are summed up across both detectors, to cancel any differences in detection path efficiencies and noise rates. Since only one set of filters was available, the polarization analysis setup was adapted slightly (see Figure 5.4 ii): The PBS in the polarization analysis path was moved after the iris and both outputs of the PBS (transmitted and reflected path) were guided through a bandpass filter to a fibre-coupled single photon detector separately.

Another change to the system is the Raman beam direction. While in the previous experiment the Raman beam was oriented along the B field, here it was directed parallel and opposite to the 729 nm qubit laser (see Figure 5.2), which has an angle of  $45^\circ$  to the B-field. This change was done for other experiments carried out during the same time period.

### 5.4.2 Results for ion - telecom-photon entanglement with the improved system

The ion - photon state was first measured directly after the conversion setup without fibre spool, via state tomography. Figure 5.7 shows the measured photon wavepacket and the reconstructed density matrix. The different angle together with a different optical power of the Raman laser results in a longer wavepacket compared to the result in Figure 5.6. The reconstructed state has a fidelity, to the nearest

1550 nm Detector	Solid state	SNSPD 1	SNSPD 2
Efficiency in %	10	74	75
Dark count rate	1.9(2)	0.6(1)	0.6(1)

Table 5.3: Efficiency and dark count rate for our 1550 nm single photon detectors. Solid state single photon detector: IDQuantique, InGaAs ID230. SNSPD: Scontel FCOPRS-CCR-2TW75+2SW85. The efficiency for the solid state detector is from the manufacturer’s data sheet, while the efficiencies for the SNSPDs were measured by the company directly after installation, using a calibrated single photon source. The dark count rate of all detectors were measured directly in the lab.

maximally entangled two-qubit state, of  $F^m = 0.971 \pm 0.007$ . This value is statistically-consistent with the one achieved at 0 km before the system improvements. The purity of the reconstructed density matrix is  $\gamma = 0.95(1)$ . The maximum fidelity that a state  $\rho$  can have with a maximally-entangled two-qubit state is given by the square root of the purity of  $\rho$ . Since  $\sqrt{0.95(1)} = 0.97(1)$ , the fidelity of our state is limited by its purity, which in turn is limited by non-unitary processes.

Simulating the measured noise rate<sup>3</sup> of 34.8(8) cps on a Bell state limits the fidelity to  $F^m = 0.991$  (Model 1 of Section 5.3.2). The noise rate here is dominated by photons produced via anti-Stokes Raman scattering of the pump laser inside the the conversion crystals.

The total photon detection efficiency was  $5.9 \pm 0.1\%$ . This compares to 0.41% measured before the system improvement and directly after the conversion stage (Section 5.3.1). Combining all known losses for this experiment yields 6.0(9)%. A detailed list of the known losses can be found in Table 5.4.

#### 5.4.3 Results for 100 km light-matter entanglement in the improved setup

The 50 km fibre spool was extended with a second 50 km fibre spool (both Corning SMF-28 ultra, Fiontec) using a fibre joiner. Tomography of the ion-photon state after travel through this 100 km was performed and the results are shown in Figure 5.8. In order to improve the SNR, only photon detections which occur within the first 30  $\mu$ s after the beginning of the wavepacket are used for the analysis. A strongly entangled ion-photon state is observed over 100 km, quantified by a concurrence [38]  $C = 0.70 \pm 0.07$  and state fidelity  $F^m = 0.85 \pm 0.04$  with a maximally entangled state ( $C=1$ ).

The total measured photon detection efficiency inside the expected 30  $\mu$ s photon arrival time is  $7.4(3) \times 10^{-4}$ . This total detection effi-

<sup>3</sup> This noise rate was directly taken from the experimental time tag file by counting photons outside of the photon wavepacket window

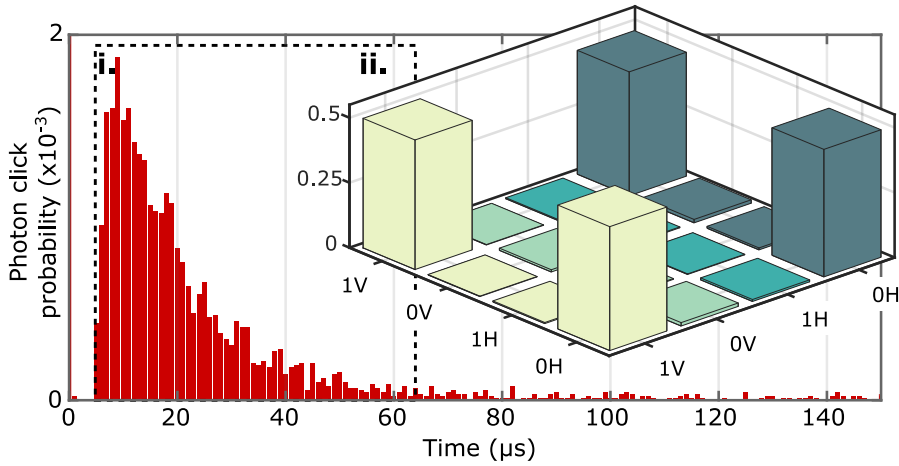


Figure 5.7: **Observation of ion-photon entanglement over 100 km of optical fibre.** i. 2D red bar chart: histogram of photon detection times (photon wavepacket in dashed box), following the generation of an 854 nm photon with a  $60 \mu\text{s}$  Raman laser pulse. Ion-photon state tomography is performed for photon detection events recorded in the dashed box (total contained probability  $P = 5.9\%$ ). ii. 3D bar chart: absolute value of experimentally-reconstructed density matrix of the telecom photonic polarisation qubit ( $H$  and  $V$  are Horizontal and Vertical, respectively) and ion-qubit state ( $|0\rangle = |D_{J=5/2, m_j=-3/2}\rangle$ ,  $|1\rangle = |D_{J=5/2, m_j=-5/2}\rangle$ ).

ciency includes wanted photons from the Raman pulse and unwanted noise photons. The detected noise rate for this experiment is  $1.3(2)$  cps (sum over both detectors and dominated by the photon detector dark counts) which corresponds to a noise photon probability per photon wavepacket of  $1.3 \text{ s}^{-1} \times 30 \mu\text{s} = 3.9 \times 10^{-5}$ . Subtracting the noise probability per wavepacket from the total measured photon detection efficiency results in the background subtracted detection efficiency of  $7.0(3) \times 10^{-4}$ . The product of the known efficiencies for the 100 km experiment shown in Table 5.4 results in  $(8.1 \pm 1.3) \times 10^{-4}$  and is consistent within statistics with the measured background-subtracted detection efficiency.

Now the sources of infidelity in the ion-photon state over 100 km are modelled. Recall that we obtained a fidelity of  $F^m = 0.85 \pm 0.04$  and that the measured noise count rate is  $1.3(2)$  cps. We use the 'Model 1' from Section 5.3.2 for simulating the effect of noise on a perfect Bell state. Simulating the measured noise rate onto a perfect Bell state, we obtain a value of 0.95. This simulated value is significantly different from the experimentally obtained value. Another source of infidelity has to limit the fidelity. The new source of error was caused by a mistake in setting the frequency of laser pulses during the experiment. The difference from the fidelity produced by Model 1 to the experimental measured value is caused by rotations of the ion-photon state during the experiment.

Location in the photon path	Efficiency
On demand photon out of cavity $P_{\text{out}}$ [71]	$0.64 \pm 0.03$
1 <sup>st</sup> single-mode fibre coupling	$0.82 \pm 0.05$
Telecom conversion stage (& filtering)	$0.22 \pm 0.02$
100 km fibre transmission	$0.0136 \pm 0.0004$
2 <sup>nd</sup> single-mode fibre coupling (to detector)	$0.70 \pm 0.05$
Telecom photon detector efficiency	$0.74 \pm 0.05$
Expected 0 km detection probability	$(6.0 \pm 0.9) \times 10^{-2}$
Measured 0 km detection probability	$(5.9 \pm 0.1) \times 10^{-2}$
Expected 100 km detection probability	$(8.1 \pm 1.3) \times 10^{-4}$
Measured 100 km detection probability	$(7.0 \pm 0.3) \times 10^{-4}$

Table 5.4: Photon losses in the 100 km photon distribution experiment. See Figure 5.1 for the respective locations in the experimental setup.

In our experimental sequence there is a beat frequency  $\delta_{393}$  between the two tones of the bichromatic 393 nm Raman laser pulse that generates the entangled ion-photon state. There is also a beat frequency  $\delta_{729}$  between the two 729 nm pulses used for the analysis of the ion-photon state. The frequencies and phases of the two beats are set by the PulseBox at the beginning of each experimental sequence. Ideally, as mentioned in Section 3.5.2,  $\delta_{393} = \delta_{729}$  which keeps the phase relation between the beat signals constant. If the beat frequencies are not equal then the relative phase of the beats evolves in time during the experimental sequence, leading to the phase of the ion-photon state being a function of the time of photon detection during the experimental sequence. Due to a mistake, the frequency difference was set to  $\Delta f = \delta_{393} - \delta_{729} = 66$  Hz. The phase evolution of the ion-photon state due to photons detected from the same Raman pulse over the Raman pulse length of  $30 \mu$  is only  $\phi = 0.012$  rad. The phase evolution of the ion-photon state due to photons detected from different Raman pulses is comparably large. These photons are  $j \times 758 \mu\text{s}$  apart, with  $j$  the number of attempts between the photons. The sequence for this experiment was set to maximally 10 unsuccessful photon generation and detection attempts, before the sequence resets. Therefore, also 10 differently rotated entangled states could be measured, depending which attempt was successful. So the total reconstructed state, which includes data from all attempts, should lead to a mixture of these 10 rotated two-qubit states. Also the purity of the measured state indicates mixed states: The purity of the measured state is  $\gamma = 0.74(5)$ , which is significantly lower than  $\gamma = 0.95(1)$ , achieved with the 0 km experiment.

Now a simple model of the frequency setting error on the ion-photon state is presented. A frequency difference  $\Delta f$  causes a phase

evolution of entangled states  $\phi(t) = 2\pi\Delta ft$  over time  $t$ . Given the time difference of  $t = 758 \mu\text{s}$  between photon generation attempts and the frequency mismatch of  $\Delta f = 66 \text{ Hz}$ , one obtains a phase rotation between attempts of  $\phi = 0.315 \text{ rad}$ . I model this phase rotation as:

$$R_z(\phi) = \begin{pmatrix} 1 & 0 \\ 0 & 1 \end{pmatrix} \otimes \begin{pmatrix} e^{-i\phi} & 0 \\ 0 & e^{i\phi} \end{pmatrix}, \quad (5.1)$$

where the first operator acts on the photon-qubit and the second on the ion qubit. For simulating the effect of this rotation over the experimental sequence onto the measured state, we rotated 10 Bell states ( $|\Psi^+\rangle$ ) with the expected angles.

$$\rho_j = R_z(j\phi)\rho_0R_z(j\phi)^\dagger, \quad (5.2)$$

with  $\rho_0 = |\Psi^+\rangle\langle\Psi^+|$  and  $j = 0, 1, \dots, 9$  the repetition number. Since the total photon detection probability is much less than one, we can expect that the photon counts are equally distributed over these 10 repetitions. This leads to a total simulated state of

$$\rho_{sim} = \frac{1}{10} \sum_j \rho_j. \quad (5.3)$$

This simulated state  $\rho_{sim}$  has a purity of  $\gamma = 0.70$ , which is consistent with the purity of the measured state to within one standard deviation of uncertainty. The fidelity of  $\rho_{sim}$  with the nearest maximally entangled state is  $F^m=0.82$ , which is also statistically consistent with  $F^m=0.85 \pm 0.04$  observed in the experiment. The fidelity between the experimental reconstructed and the simulated state  $\rho_{sim}$  is  $F = 0.97 \pm 0.03$ . This model describes our experiment well.

We conclude that the main limit to the observed ion-photon entanglement fidelity over 100 km was a mistake in setting laser frequencies and is straightforward to correct in future.

## 5.5 DISCUSSION

In this Chapter we demonstrated entanglement between a trapped ion and photon that had travelled over up to 100 km of optical fibre. In these experiments the photon travelled over a fibre spool in our lab. Repeating this for a deployed optical fibre that distributes the photon to a remote location is more challenging. First, due to larger temperature and pressure fluctuations, a deployed optical fibre is expected to rotate the polarization of the transmitted photon on shorter timescales compared to the fibre spool inside a temperature stabilized lab. As such one expects to have to stabilise for the polarisation rotations in the deployed fibre. One approach is to first characterise the polarization rotation through the fibre, e. g. by sending classical light with defined polarizations through the fibre, then correct for that rotation using

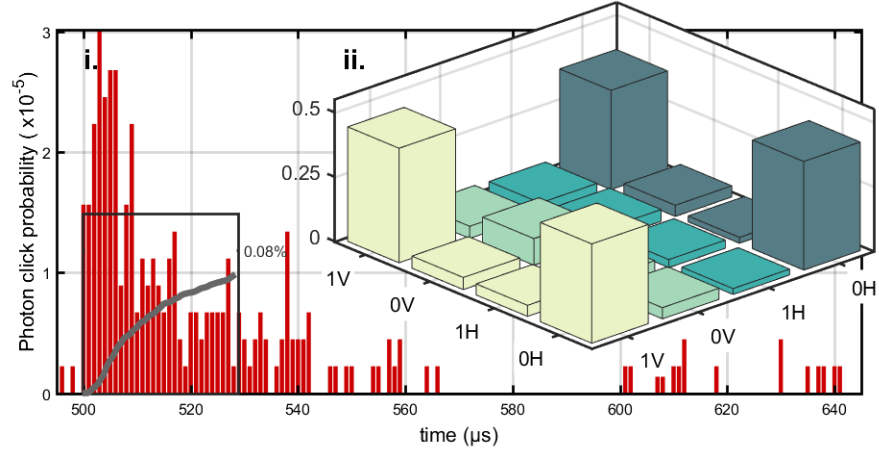


Figure 5.8: **Observation of ion-photon entanglement over 100 km of optical fibre.** **i.** 2D red bar chart: histogram of photon detection times, following the generation of an 854 nm photon with a 60  $\mu\text{s}$  Raman laser pulse 494  $\mu\text{s}$  earlier, repeated at 650 Hz. Ion-photon state tomography is performed for photon detection events recorded in the inset small box (total contained probability  $P = 7 \times 10^{-4}$ ). **ii.** 3D bar chart: absolute value of experimentally-reconstructed density matrix of the telecom photonic polarisation qubit ( $H$  and  $V$  are Horizontal and Vertical, respectively) and ion-qubit state ( $|0\rangle = |D_{J=5/2, m_j=-3/2}\rangle$ ,  $|1\rangle = |D_{J=5/2, m_j=-5/2}\rangle$ ).

waveplates. This characterisation and correction should be performed and repeated on a timescale that is determined by the timescale of the polarisation dynamics in the fibre. Classical light, which can be filtered out from single photons, could be used for a live analysis of the polarization dynamics [126].

Going beyond 100 km ion-photon entanglement would be possible by increasing the overall photon detection efficiency. However, the ion-cavity photon source works already near the upper limit of photon generation efficiency. Also the SPDC's are state of the art single photon detectors and the detection efficiency is close to 1. The efficiency of the conversion setup (as discussed in Section 4.6) and the overall fibre couplings could still be improved. Altogether, we don't expect improvements in efficiency of the whole system by more than a factor of 3 in our system. A factor of 3 allows for additional  $\sim 25$  km of optical fibre without significantly changing the total detection efficiency and the signal-to-noise-ratio. Nevertheless, 100 km is already a reasonable internode spacing to start building quantum networks according to the quantum repeater approach. The first steps towards such a quantum repeater using our system are shown in Chapter 8.

In the experiments presented in this chapter the detection of a photon after travelling over the optical fibre signals a successful distribution event and triggered state characterisation of the ion-qubit. Since the fibre was coiled up we had to wait for the one-way travel time,

but the return classical signal took only some tens of nanoseconds to travel over a few meters over electric cables. In the case of a deployed optical fibre, in a straight line away from the ion-trap, one would have to wait twice the fibre travel time. For a 100 km fibre, the total wait time increases then from 494  $\mu\text{s}$  to 988  $\mu\text{s}$ . While this presents no significant challenge to the memory of our ion-qubit (see section 5.3) the maximum reachable repetition rate decreases by a factor of 2 from 2 kHz to 1 kHz. When considering only photon losses due to fibre losses (0.16 dB/km, Corning SMF-28 ULL) this limits the maximal possible distribution rate, for a single ion in the trap, of 25 per second.

A way to overcome this limit, set by the speed of light, is multi-mode distribution, where multiple entanglement distribution events are carried out in parallel. This could perhaps be realized by using several ions, producing several photons subsequently, where each photon is entangled with a different ion. This approach provides then an increase in the chance of at least one photon making it compared to a single ion-photon entanglement. Using e. g. 10 ions in parallel would increase the maximum distribution rate by a factor of ten (from 25 Hz to 250 Hz in the example above). First test experiments in our group with up to 3 ions already demonstrated this method, but these experiments are beyond scope of this thesis.



## SECOND ORDER CORRELATION FUNCTION OF CONVERTED PHOTONS

---

This chapter presents measurements of the second order correlation function  $g^{(2)}$  of 854 nm photons from the ion and after conversion to 1550 nm. At the time of writing the results of this chapter are unpublished. Victor Krutyanskiy (VKru) and Martin Meraner (MM) designed and built the conversion setup. The 854 nm photon detection board was built by Vojtech Krcmarsky (VKrc), the 1550 nm detection board was built by MM. Experimental data taking was done by VKru and MM. Data analysis and interpretation was done by MM and Ben Lanyon (BPL). The project was conceived and supervised by BPL.

### 6.1 INTRODUCTION

An ideal single photon source produces one photon at a time, not more. The second order correlation function  $g^{(2)}$  describes the extent to which a photon source produces only one photon at a time [127, 128]. While the lower bound for a classical light source is  $g^{(2)} = 1$ , an ideal single photon source has  $g^{(2)} = 0$ . For measuring this function we use a Hanbury Brown and Twiss (HBT) setup [129] corresponding to a 50:50 beam splitter and a single photon detector at each output of the beam splitter. The photon detection times are recorded for each detector, yielding two lists of timetags. The  $g^{(2)}$  function can be calculated from the correlations between these timetags, as described in a later section.

In this chapter, the  $g^{(2)}$  measurements for unconverted 854 nm photons and for converted 1550 nm photons are presented. In Section 6.2 the experimental setup used to take the data is introduced. The experimental sequence is explained in Section 6.3. Section 6.4 shows the results. In Section 6.5 the results are analysed in more detail and compared to a model. Finally in Section 6.6 the results are discussed and summarized.

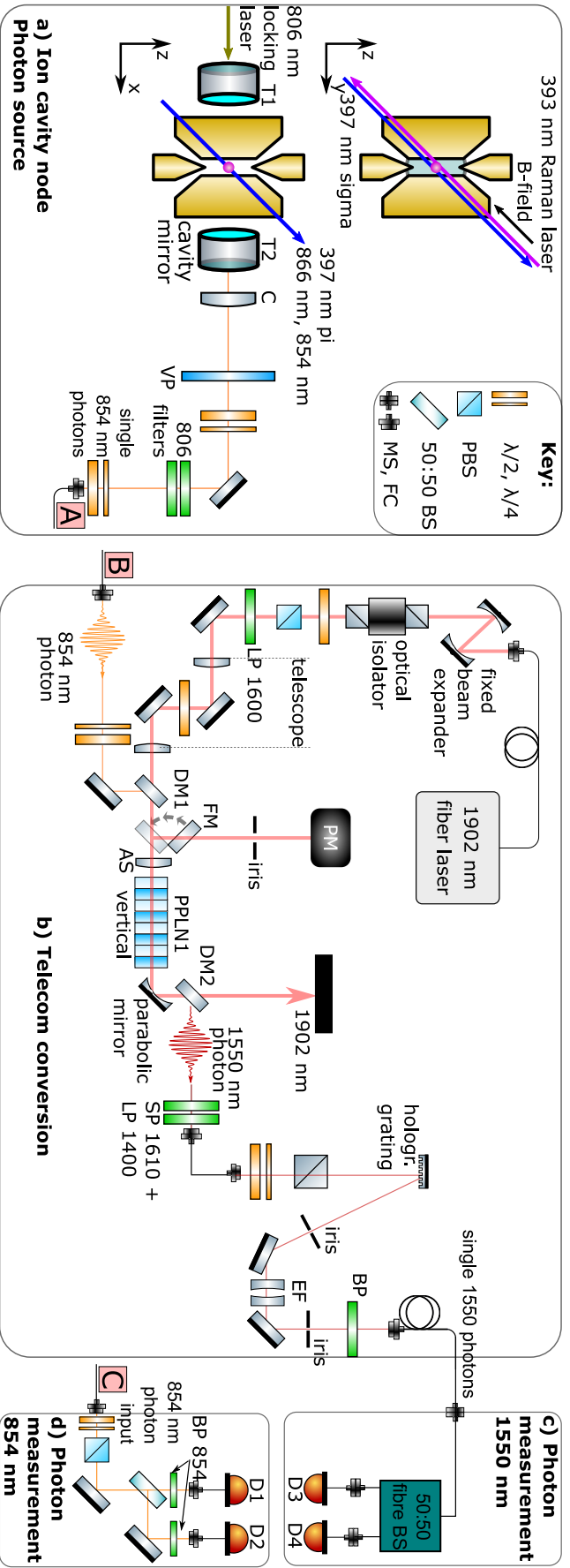


Figure 6.1: **Detailed experimental diagram for measuring the  $g^{(2)}$  function for unconverted 854 nm photons and converted 1550 nm photons.** All elements used for the experiments are shown in this diagram. **a) Ion cavity node:** A detailed explanation of this part can be found in Figure 3.3. A 393 nm Raman pulse creates a vertically polarised photon. This photon is guided through a collimating lens (C), view port of the vacuum chamber (VP), waveplates and filters before the photon is fibre coupled at point A. For the 854 nm experiment the points A and C are connected. For the 1550 nm experiment the points A and B are connected. **b) Telecom conversion:** The 854 nm photon is converted to 1550 nm via DFG using a nonlinear crystal. Therefore the 854 nm photon is overlapped with a 1902 nm pump laser on a dichroic mirror (DM1) and coupled through a PPLN waveguide. A second dichroic mirror (DM2) splits the converted 1550 nm photon from the remaining pump laser. A filter network consisting of a long pass (LP), short pass (SP), PBS, holographic Bragg grating, an etalon filter (EF) and a band pass (BP) is used to reduce the unwanted noise photons. More details on these filters, and the PPLN waveguides, can be found in Section 4.2. **c) Photon detection setup for 1550 nm photons:** the 1550 nm photons are split on a 50:50 fibre beam splitter (Thorlabs TW1550R5A2) and sent to the detectors D3 and D4 (SNSPD). **d) Photon detection setup for 854 nm photons:** the 854 nm photons are split on a 50:50 free space beam splitter and sent to the detectors D1 and D2 (SNSPD). Band passes at 854 nm (BP 854) filter the background light.

## 6.2 EXPERIMENTAL SETUP

Detailed schematics of the experimental setups used to measure the  $g^{(2)}$  functions at 854 nm and 1550 nm are shown in Figure 6.1. In summary, in both cases a vertically polarised photon produced via a CMRT (Section 3.5) from the ion-cavity system is used.

To measure the  $g^{(2)}$  function of 854 nm photons, the photons are sent directly to a free-space-coupled HBT setup, which consists of a beam splitter and two SNSPD detectors. To measure the  $g^{(2)}$  function of 1550 nm photons, the 854 nm photons are first sent to a single ridge-waveguide conversion and filtering stage (the same one as in Section 4.2.2) and then directed to a fibre-coupled HBT setup. In both HBT setups a time tagging module (Swabian Industries Time Tagger 20) stores all photon detection events on a computer for later analysis. Additionally, one digital output channel of the PulseBox (Appendix A.1) is connected to an input channel of the time tagger. The PulseBox sends a TTL to the time tagger via this channel every time a photon generation attempt is made (Raman laser pulse) to help correlate the detection events with generation attempts during data analysis.

## 6.3 EXPERIMENTAL SEQUENCE

The laser pulse sequence used for all  $g^{(2)}$  measurements is shown in Figure 6.2. Each loop in the sequence consists of Doppler cooling, followed by optical pumping to prepare the ion into the state  $S_{J=1/2, m_j=-1/2}$ , followed by a Raman pulse set to generate a vertically-polarized photon, leaving the electron ideally in the state  $D_{J=5/2, m_j=-5/2}$ . A Raman laser pulse Rabi-frequency of  $\Omega = 41(2)$  MHz was set for the experiments by adjusting laser power until the corresponding AC-Stark shift is observed on the Raman transition accordingly.

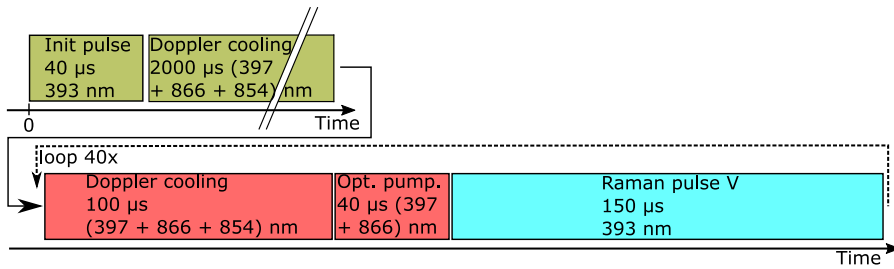


Figure 6.2: **Laser pulse sequence:** The starting sequence (shown in green) consists of an initialisation 393 nm laser pulse which is used for intensity stabilisation and Doppler cooling. The loop (shown in red and blue) consists of additional Doppler cooling, optical pumping and a (photon generation) Raman pulse which generates a vertically polarized photon. This loop is repeated 40 times. After the loop (not shown in the figure) a state detection is done (This is necessary for our sequencer but not required for the  $g^{(2)}$  measurement).

## 6.4 DATA ANALYSIS AND RESULTS

The second order correlation function for pulsed single photon sources, from one photon generation attempt (Raman pulse) to the  $n^{\text{th}}$  neighbour photon generation attempt, is given by [63, 118]

$$g^{(2)}(n) = \frac{N \cdot N_{\text{coinc},n}}{N_1 \cdot N_2}, \quad (6.1)$$

with  $N$  the total number of attempts,  $N_{\text{coinc},n}$  the number of coincidences from one generation attempt with the  $n^{\text{th}}$  neighbour generation attempt and  $N_1$  ( $N_2$ ) the number of detection events on channel 1 (2). A coincidence means that both a photon at detector 1 and a photon at detector 2 were measured. The value  $n$  means that this coincidence occurred between the  $n^{\text{th}}$  neighbouring generation attempt. For example, a coincidence with  $n = 1$  can mean that a photon was first measured at detector 1 and a subsequent photon was measured at detector 2 during the next generation attempt. A coincidence at  $n = 0$  means that within one generation attempt both a photon at detector 1 and a photon at detector 2 were measured. We only count detected photons from a photon generation attempt inside an expected photon arrival time. This so called gate starts together with the start of the Raman pulse and has a length of  $T_{\text{gate}} = 50 \mu\text{s}$ . This gate length contains 99.9% of the photon wavepacket observed in this experiment. The gate splits the photon detections into the different photon detection attempts and reduces the noise counts significantly. For our photon source we expect  $g^{(2)}(0) \geq 0$  due to added background noise. For  $n \neq 0$  we expect  $g^{(2)}(n \neq 0) = 1$ . The different values from Equation 6.1 can be analysed from the saved timetags as described now.

Key decisions in the data analysis are now listed. First, we extract only counts from each detector that occur during a window  $T_{\text{gate}}$ , immediately following a Raman pulse. Second, cases where during one photon generation attempt multiple photon detection events on the same detector are detected we considered only the first one. Third, the number of coincidences  $N_{\text{coinc},n}$  between one photon generation attempt and the  $n^{\text{th}}$  neighbour are counted. A coincidence is an event where one detector detected a photon in the  $k^{\text{th}}$  generation attempt, while the other detector detected a photon in the  $(k+n)^{\text{th}}$  generation attempt. Finally, the  $g^{(2)}(n)$  function can be calculated using Equation 6.1.

For the 854 nm experiment, 12 million generation attempts were performed, which took about 1.5 hours. For the 1550 nm experiment, 24 million generation attempts were performed, taking around 3 hours. The  $g^{(2)}(n)$  functions measured for both 854 nm and 1550 nm photons are shown in Figure 6.3. The key results are  $g_{854}^{(2)}(n=0) = 3.1(2) \cdot 10^{-3}$  for the unconverted 854 nm photons and  $g_{1550}^{(2)}(n=0) = 0.17(1)$  for the converted 1550 nm photons.

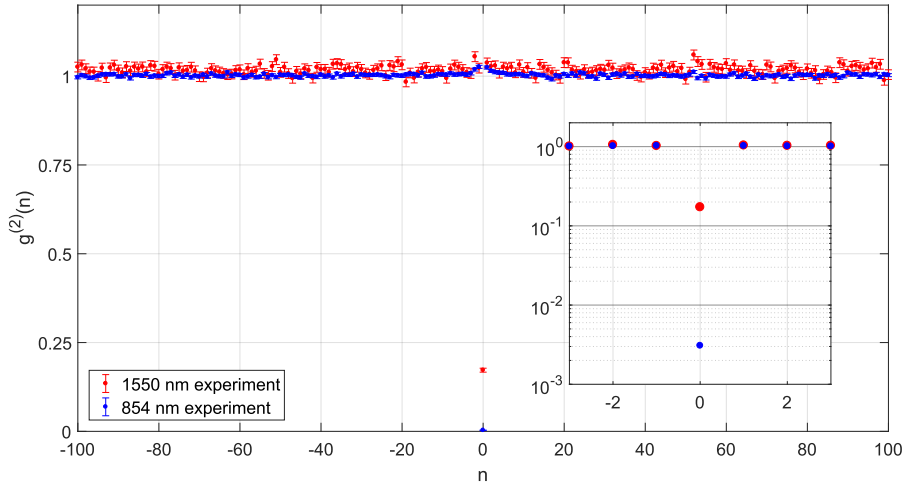


Figure 6.3: **Measured  $g^{(2)}(n)$  function for 854 nm and frequency-converted 1550 nm photons.**  $n$  is the number of generation attempts between coincident photon detection. The blue points represent unconverted 854 nm photons. The red points represent the converted 1550 nm photons. The errorbars display one standard deviation assuming Poissonian counting statistics. For the 854 nm experiment we see a  $g^{(2)}(n) > 1$  for  $n$  close to 0. This shows that our system has a higher probability of generating a photon, when in the previous attempts already a photon was generated successfully. For the 1550 nm experiment we see  $g^{(2)}(n \neq 0) > 1$  for nearly all values. This is caused by the higher total noise rates for this experiment. The small inset plot is a zoom-in around  $n = 0$  with a logarithmic vertical axis. The error bars, based on Poissonian photon counting statistics, are smaller than the displayed points.

The experimental results for the 854 nm experiment shown in Figure 6.3 shows  $g^{(2)}(n) > 1$  for  $n$  close to 0. It seems that our photon source has a higher probability to generate a photon, when the previous generation attempt was successful. At time of writing, the origin of the effect is not understood.

## 6.5 TIME DEPENDANT ANALYSIS OF THE $g^{(2)}$ FUNCTION

To understand the finite  $g^{(2)}(0)$  values, we now look into the time distribution of the coincidence counts within a photon generation attempt and compare it with a theoretical model.

To get a time dependant  $g^{(2)}$  function from the data, the time differences between corresponding detection events on channel 1 and channel 2 are calculated. The histogram of these measured time differences gives the correlation function with the time difference on the x-axis. The y-axis of the histogram can be formed into a probability density by dividing the number of coincident detection events by the number of photon generation attempts ( $N$ ) and by the bin size

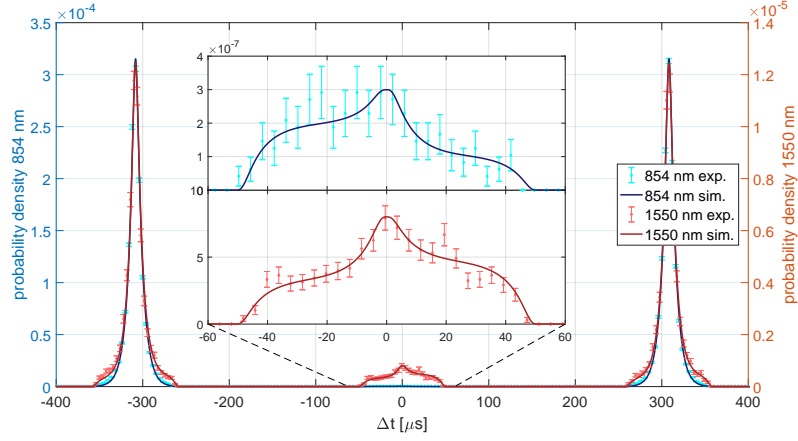


Figure 6.4: **Measured and simulated coincidence probability density.** The peaks near  $\pm 300\mu\text{s}$  correspond to a measured correlation between one generation attempt and the next neighbour generation attempt. The small peak (and zoom-in) in the centre corresponds to coincidences within the same photon generation attempt. The blue data points represent the unconverted 854 nm data, the red data points represent the converted 1550 nm data. The error bars represent one standard deviation of uncertainty due to Poissonian photon counting statistics. The solid lines represent the model for a perfect single photon source that includes our independently-measured background noise, as described in the text. For this plot a  $50\mu\text{s}$  gate starting together with the Raman pulse was used. The asymmetric shape of the small peak is caused by different path efficiencies and background noise rates for the two detectors, after the 50:50 beam splitter.

used in the histogram. Figure 6.4 presents this density plot for our experiments, for a bin size of  $1\mu\text{s}$ . The theory lines in this figure are explained in the next section.

### 6.5.1 Contributions to $g^{(2)}(0) \neq 0$

Now we develop a model which explains the offset from  $g_{854}^{(2)}(n=0) = 0$ . The model assumes a single photon source with  $g_{\text{source}}^{(2)} = 0$  spoiled with white noise, yielding a total value of  $g_{\text{total}}^{(2)}$ . White noise means a constant noise probability in time. In this section each of the known contributions to  $g_{\text{total}}^{(2)}$  in our experiment are explained.

Equation 6.1 can be rewritten in terms of the total click probabilities of each detector,  $P_{\text{tot}1}$  and  $P_{\text{tot}2}$ , and the coincidence probability  $P_{\text{coinc},n}$  of the channel, during a given time bin as

$$g^{(2)}(n) = \frac{P_{\text{coinc},n}}{P_{\text{tot}1} \cdot P_{\text{tot}2}}, \quad (6.2)$$

where  $P_{\text{tot}i} = P(Ph_i) + P(N_i)$ , the sum of the probabilities that detector  $i$  clicked due to a photon from the ion,  $P(Ph_i)$ , and due to a noise

event,  $P(N_i)$ . The total coincidence probability between the two paths can be expressed as

$$P_{\text{coinc},n} = P(Ph_1 \cap Ph_2) + P(Ph_1 \cap N_2) + P(N_1 \cap Ph_2) + P(N_1 \cap N_2). \quad (6.3)$$

For a perfect single-photon source the correlation  $P(Ph_1 \cap Ph_2) = 0$  for  $n = 0$  and  $P(Ph_1 \cap Ph_2) = P(Ph_1) \cdot P(Ph_2)$  for  $n \neq 0$ . The remaining contributions to  $P_{\text{coinc},n}$  in Equation 6.3 are due to what in this thesis is called ‘noise’ photons which are assumed to be independent such that they can be written as a product of single event probabilities  $P(A \cap B) = P(A) \cdot P(B)$ .

### 6.5.2 Measured rates

This section explains how the different terms in the model given in Equation 6.3 are determined. Specifically, how our estimates of the probabilities for detecting noise photons and for detecting photons produced by the ion are derived from the experimental data. First, we obtain an estimate for the noise rate for a given detector by looking at the timetags recorded in time windows during which a photon generation attempt did not occur. Specifically, we choose a 100  $\mu\text{s}$  window at a point in the experimental sequence when Doppler cooling of the ion is occurring and no cavity photons are being generated. Inspection of the timetag file shows no observable difference in the photon count rate at this Doppler-cooling time compared to shorter time windows during which no lasers are being shone into the ion trap. As such, the total photon counts during this 100  $\mu\text{s}$  window are expected to come from background noise sources that will also be present during the photon generation attempt. By dividing the total counts in these windows by 100  $\mu\text{s}$ , and by the total number of attempts, we obtain our estimate for the total photon noise rate of each detector. This noise includes the photon detector’s dark count rate and the noise counts created from background room light. For the 1550 nm experiment also the noise produced by the photon conversion pump laser is present at all times, since the pump laser remains on.

The measured background noise rates for the different detectors are shown in Table 6.1. Separate measurements of noise rates show that the main contribution at 854 nm is background room light. Only  $0.3 \pm 0.1 \text{ s}^{-1}$  ( $0.5 \pm 0.1 \text{ s}^{-1}$ ) of the total noise rate corresponds to the detector dark count rate of channel 1 (channel 2) at 854 nm. The main contribution to the noise rates at 1550 nm are noise photons produced by the pump laser in the conversion crystal. The measured<sup>1</sup> dark count rate of the 1550 detectors for both channels is  $0.6 \pm 0.1$

<sup>1</sup> The detector dark count rate was measured by closing the fibre input to the cryostat with a cap for an acquisition time of 60 s. This measurement was performed by the manufacturer after installing the detector in our lab.

$s^{-1}$ . A separate 1550 nm measurement without any pump laser power gives the contribution to the noise rate due to background room light as  $2.6 \pm 0.2 s^{-1}$  for channel 1 and  $7.9 \pm 0.3 s^{-1}$  for channel 2 (after subtracting the given detector dark counts). This unbalanced noise rate due to room light is caused by asymmetric shielding of the fibres in the 50:50 beam splitter. The colour of one of the fibre coatings is red while the other one is white and the red one does better at screening out room light. The remaining 1550 nm noise rates of  $20.5 \pm 0.3 s^{-1}$  and  $22.6 \pm 0.3 s^{-1}$  on channel 1 and 2, respectively, correspond to the rate of noise photons produced by the pump laser. The unbalanced noise rate from the pump laser can be entirely explained by the two different detection path efficiencies, as also seen in Table 6.2.

Detector	854 Ch1	854 Ch2	1550 Ch1	1550 Ch2
Noise rates ( $s^{-1}$ )	$2.71 \pm 0.05$	$2.42 \pm 0.03$	$23.7 \pm 0.1$	$31.1 \pm 0.1$

Table 6.1: **Noise rate estimates extracted from time tag data files as described in the main text.** Calculated noise rates for all detectors used in both (854 nm and 1550 nm)  $g^{(2)}$  experiments. Due to the conversion process, the noise rates for the 1550 nm experiment are significantly higher compared to the 854 nm experiment. The unbalanced noise rate for the two 1550 nm detectors are caused by background light and could be avoided by better shielding of both output fibres from the 50:50 fibre beam splitter.

Next, the photon probability from a Raman pulse can be analysed. The total measured click probability inside a Raman pulse is the sum of the probability of detecting a photon from the ion due to a Raman pulse and the noise probability during this Raman pulse. This total click probability is calculated by dividing the total measured detection events during the Raman pulses by the number of total Raman pulse attempts. Since the noise rates and path efficiencies are different for each channel, this analysis has to be done for both detectors separately. By subtracting the noise probability from the total click probability the single photon probability is obtained. Table 6.2 presents the total photon detection probabilities  $P_{\text{tot},i}$  and the estimates of the noise probabilities  $P(N_i)$  during a Raman pulse and photon probabilities due to a Raman pulse  $P(Ph_i)$ .

### 6.5.3 Comparison of the measured and modelled $g^{(2)}$ function

As already mentioned, noise photons are assumed to be 'white', meaning that they are equally distributed over time. Therefore, the noise photon rate is multiplied by the time bin length of the simulation to get the noise probability per time bin. In contrast, the detection probability of a photon from the ion per time bin evolves dynamically across the single photon wavepacket. To obtain a model for the photon

Photon probability	$P_{\text{tot},i}$	$P(N_i)$	$P(Ph_i)$
854 Ch1	0.0729(1)	$1.36(3) \cdot 10^{-4}$	0.0728(1)
854 Ch2	0.0717(1)	$1.21(2) \cdot 10^{-4}$	0.0716(1)
1550 Ch1	0.01453(8)	$1.19(5) \cdot 10^{-3}$	0.01334(3)
1550 Ch2	0.01608(3)	$1.56(5) \cdot 10^{-3}$	0.01452(3)

Table 6.2: The columns show, from left to right, the measured total probability for detecting a photon during a Raman pulse ( $P_{\text{tot},i}$ ), the estimated noise probability ( $P(N_i)$ ) calculated from Table 6.1 and the photon probability from a Raman pulse calculated by subtracting the estimated noise probability from the total detection probability ( $P(Ph_i) = P_{\text{tot},i} - P(N_i)$ ).

wavepacket a numeric simulation was performed. The used simulation code was developed by the QED team at UIBK, led by Tracy Northup. The code is based on the master equation formalism and uses independently-measured cavity and atomic parameters for this experiment. More details about the numerical simulation of wavepackets can be found in [130]. For this simulation a Raman Rabi frequency of  $\Omega = 41$  MHz, an ion-cavity coupling strength of  $g = 1.19$  MHz and a detuning from Raman resonance of  $\delta = 40$  kHz was used. After the numerical simulation of the wavepacket, the simulated results are gated with the same gate ( $T_{\text{gate}} = 50 \mu\text{s}$ , starting together with the Raman pulse) used in the experiment. The numerical model predicts the photon probability out of the cavity, not the final detected probability which includes all losses in the detection path. For the 854 nm experiment we find that detection path efficiencies of 10.80(2)% and 10.62(2)% for channel 1 and 2, respectively, produce a close match between the model and measured wavepackets. Remember, the 50:50 beam splitter already at least halves the path efficiency. For the 1550 nm experiment we find path efficiencies of 1.97(4)% for channel 1 and 2.15(4)% for channel 2. With these efficiencies the single photon probability in each time bin of the wavepacket can be simulated.

Finally, we use equation 6.3 to convert the simulated single ion-photon and noise-photon probabilities into the simulated coincidence probabilities. The solid lines in Figure 6.4 show the results of this simulation, overlapped with the experimentally measured data for both photons at both 854 nm and 1550 nm. One sees that the model describes the data well, to within statistical precision. By integrating the simulation over the correlations, second order correlations of  $g_{854}^{(2)}(0) = 2.9(1) \cdot 10^{-3}$  for unconverted 854 nm photons and  $g_{1550}^{(2)}(0) = 0.17(1)$  for converted 1550 nm photons are obtained as simulated results. The uncertainty of these values are the standard deviations of 100 repetitions of the simulation, while the relevant noise rates and detection efficiencies were randomly generated according to a normal distribution, with the mean value and the standard deviation taken

as the measured values and their uncertainty. The simulated values are equal within statistical uncertainty with the measured results of  $g_{854}^{(2)}(n=0) = 3.1(2) \cdot 10^{-3}$  for the unconverted 854 nm photons and  $g_{1550}^{(2)}(n=0) = 0.17(1)$  for the converted 1550 nm photons.

## 6.6 DISCUSSION AND CONCLUSION

The signal to noise ratio (SNR) can be expressed as

$$\text{SNR}_i = P(Ph_i) / P(N_i), \quad (6.4)$$

which corresponds to the ratio of the ion-photon detection probability to the background click probability, for detector  $i$ . Equation 6.2 can be re-expressed in terms of the SNR as:

$$g^{(2)}(0) = 1 - \frac{\text{SNR}_1 \text{SNR}_2}{(\text{SNR}_1 + 1)(\text{SNR}_2 + 1)}. \quad (6.5)$$

It is clear that increasing the SNR lowers the  $g^{(2)}(0)$ .

Since the photon wavepacket shape (see e. g. figure 5.7) has a long tail with lower photon detection probability compared to the front of the wavepacket, a shorter gating improves the SNR and consequently  $g^{(2)}(0)$ , at the expense of a reduced count rate and therefore larger error bars. For example, a gate starting with the Raman pulse, with a length of  $T_{gate} = 25 \mu\text{s}$  still contains 97% of the counts in the photon wavepacket while halving the noise counts.

For unconverted 854 nm photons and a gate length of  $T_{gate} = 25 \mu\text{s}$  we achieved a measured second order correlation value of  $g_{854}^{(2)}(0) = 1.5(5) \cdot 10^{-3}$ : a factor of two lower than the value for the 50  $\mu\text{s}$  gate. In both cases, the difference between the measured value and the one for an ideal photon source can be entirely explained by the background noise rates in our experiments. The noise rate is dominated by the room background light induced by imperfect shielding. A better shielding of the HBT setup that eliminates the estimated noise due to room light would yield a  $g^{(2)}(0)$  value at 854 nm of  $2.8(5) \cdot 10^{-4}$  for  $T_{gate} = 50 \mu\text{s}$  and  $g^{(2)}(0) = 1.4(2) \cdot 10^{-4}$  for  $T_{gate} = 25 \mu\text{s}$ , dominated by detector dark counts. The work in [118, 131], led by Thomas Walker, at the University of Sussex achieved  $g_{854}^{(2)}(0) = 1.7(12) \cdot 10^{-3}$  for unconverted 866 nm photons. Here, the value was limited by the detector dark count rate and the room background light equally.

For the converted 1550 nm photons and a gate length of  $T_{gate} = 25 \mu\text{s}$  we achieve a measured second order correlation value of  $g_{1550}^{(2)}(0) = 0.10(2)$ . The offset from 0 can be entirely explained by the noise rates within statistical uncertainty. Here, the dominant source of noise is due to photons generated by Anti-Stokes Raman scattering of the pump laser used for frequency conversion. A narrower frequency filtering

could decrease the noise further without significantly affecting the total efficiency: the current filtering has a bandwidth of 250 MHz, whilst the photon line width of converted photons is expected to be below a few MHz.

A lower pump power would also decrease the noise rate with the cost of a lower conversion efficiency. The experiments in this chapter were optimized for maximum conversion efficiency. Lower  $g$ -factors could be achieved by optimizing the SNR, as shown in Section 4.2.2. Background light also produces a non-negligible part of the noise. A better shielding of the fibres from the HBT setup to the detector should decrease this part of the noise significantly. The work in [118, 131], led by Thomas Walker, at the University of Sussex achieved  $g_{1530}^{(2)}(0) = 0.67(7)$  for converted 1530 nm photons. Additionally they measured the second order correlation for converted photons after 10 km of optical fibre and achieved  $g_{1530}^{(2)}(0) = 0.59(7)$ .

Another way to improve  $g^{(2)}(0)$  could be to generate shorter photon wavepackets by using a higher Rabi-frequency. Preliminary simulations show that while shorter wavepackets decrease the overall efficiency [71] there is an increase in probability density for shorter gate times. Another drawback of shorter photon wavepackets generated by higher Rabi-frequencies is the increase in their distinguishability as analysed in [132].



## INDISTINGUISHABILITY OF CONVERTED PHOTONS

---

This chapter includes the measurement of indistinguishability between two photons produced by the same ion and converted to the telecom wavelength. That result is published in [Phys. Rev. A 102, 052614 \(2020\) \[132\]](#) and the authors are Martin Meraner (MM), Azadeh Mazloom (AM), Victor Krutyanskiy (VKru), Vojtech Krcmarsky (VKrc), Josef Schupp (JS), Dario A. Fioretto (DF), Pavel Sekatski (PS), Tracy E. Northup (TN), Nicolas Sangouard (NS), and Ben Lanyon (BPL). VKru, MM, and VKrc took the data. VKrut, AM, BPL, PS and MM analysed the data. VKrut, MM, VKrc, JS and BPL contributed to the experimental setup and design. AM, VKrut, PS, BPL, MM, DF, TN and NS performed theoretical modelling. BPL, VKrut, MM, PS, TN and NS wrote the majority of the paper, with contributions from all authors. The project was conceived and supervised by BPL. Except for minor modifications, the contents of this chapter are taken directly from [132], but bring together the main text and supplementary into one continuous document.

### 7.1 ABSTRACT

Trapped atomic ions embedded in optical cavities are a promising platform to enable long-distance quantum networks and their most far-reaching applications. Here we achieve and analyse photon indistinguishability in a telecom-converted ion-cavity system. First, two-photon interference of cavity photons at their ion-resonant wavelength is observed and found to reach the limits set by spontaneous emission. Second, this limit is shown to be preserved after a two-step frequency conversion replicating a distributed scenario, in which the cavity photons are converted to the telecom C band and then back to the original wavelength. The achieved interference visibility and photon efficiency would allow for the distribution and practical verification of entanglement between ion-qubit registers separated by several tens of kilometres.

## 7.2 INTRODUCTION

Envisioned quantum networks, consisting of remote quantum matter linked up with light [3, 6], offer a fundamentally new communication paradigm [133] as well as a practical path to large-scale quantum computation and simulation [7] and to precision measurements in new regimes [8, 134, 135]. Trapped atomic ions are expected to enable the most promising applications of large-scale quantum networks [26, 83, 136] given their demonstrated capabilities for quantum logic [137], multi-qubit registers [138], and optical clocks [139]. Ion qubits have been entangled with propagating photons [140] and those photons have been used to entangle ions in traps a few meters apart [10, 28, 141]. Integrating ion traps with optical cavities offers the possibility of a near-deterministic and coherent light-matter interface for quantum networking [26, 136], and both ion-photon entanglement [31] and state transfer [77] have been achieved in this setting.

Photons from trapped ions have recently been converted to the optimal telecom wavelengths for long-distance quantum networking [18, 41, 118]. Those experiments used near-infrared photons from a trapped calcium ion, allowing for direct, low noise conversion in the long-pump wavelength regime [41, 60] and efficiencies of tens of percent. The combination of telecom-conversion and ion-photon collection using an optical cavity could allow for entangled ions spaced by a hundred kilometres [41] via the entanglement the swapping protocol [21], orders of magnitude further than the state of the art of a few meters [10, 28, 141]. However, the quality of the swapped entanglement is set by the degree to which the involved photons are indistinguishable, and this has not previously been studied for either an ion-cavity system or for telecom conversion of ion-compatible photons.

The extent to which photons are in identical pure states, and therefore indistinguishable can be quantified by the visibility in a two-photon interference experiment [121]. The visibility is directly related to the swapped entangled state fidelity [21]. For a detailed theoretical analysis of two-photon interference from quantum emitters without conversion see, e. g. , [142, 143]. While direct two-photon interference has been achieved using neutral atoms in cavities [144, 145], it has not previously been reported for ions in cavities. As will be shown, the limiting factor on the interference visibility in our ion-cavity system is unwanted spontaneous emission from the ion during the cavity-mediated photon generation process. Such spontaneous emission is particularly relevant for ion-cavity systems demonstrated to date in which the ion-cavity coupling rate does not overwhelm the spontaneous scattering rate. Furthermore, photon conversion stages can easily introduce additional distinguishability, e.g., by directly adding noise photons at a rate that depends strongly on the particular photon

and pump laser wavelengths and filtering bandwidth [60], and must be assessed on a system-dependent basis.

In this chapter, experimental and theoretical results of photon distinguishability in a telecom-converted ion-cavity setting, based on interference between two photons produced sequentially from an ion in a cavity are presented. First, the experimental system is introduced and a summary of the theoretical model, developed by our collaborators from the University of Basel, of the effect of spontaneous emission on the emitted cavity photon is given. The full theoretical model can be found in the supplementary material of [132]. Second, two-photon interference results of cavity photons at the ion-resonant wavelength are presented, showing that spontaneous emission is the dominant limiting factor. Third, two-photon interference results are presented after a two-step frequency conversion, converting the wavelength of one cavity photon to the telecom band and back to the ion-resonant wavelength, showing that the photon indistinguishability is essentially preserved up to frequency instabilities of the pump laser. As an outlook, it is calculated that the achieved interference visibilities and overall detection efficiencies could already allow for the first observation of entanglement of ions tens of kilometres apart and presents paths to significantly extend that distance.

## 7.3 EXPERIMENTAL DETAILS AND MODEL

### 7.3.1 *Summary of the theory*

The effect of spontaneous scattering on the visibility is precisely quantified through a theoretical model describing the evolution of a three-level atom embedded in a cavity using a master equation, see appendix of the paper [132]. In the model, an expression for the mixed state of photons emitted from the cavity is obtained in two steps. First, we calculate the wave function of photons emitted from the cavity conditioned on the ion being in the initial state  $|S\rangle$  at time  $s$  and no spontaneous decay events happening for later times. Second, we compute the rate of spontaneous decay events from  $|P\rangle$  to  $|S\rangle$  as a function of time. The state of the emitted cavity photon is then expressed as a mixture over all the possibilities where the last  $|P\rangle \rightarrow |S\rangle$  decay happens at time  $s$  or no decay events occur and a pure state photon is emitted afterwards, plus the vacuum component collecting all the possibilities where no cavity photon is emitted. With the emitted photon states in hand, it is then straightforward to calculate the visibility of pairs of such photons (supplementary material of [132]). We refer to this model, that includes only imperfections due to spontaneous scattering, as the basic model. As an alternative from our model, the visibility could be computed from the master equation via the quantum regression theorem [142].

### 7.3.2 Experimental setup

Detailed schematics of the experimental setups used for the measurement of indistinguishability between two photons produced by the same ion and converted to the telecom wavelength are shown in Figure 7.1. Experiments employ a single  $^{40}\text{Ca}^+$  atom in the centre of a linear Paul trap and in the focus of a near-concentric optical cavity near-resonant with the 854 nm electronic dipole transition (Figure 7.2) [41]. We begin by Doppler cooling the ion's motional state and optical pumping into an electronic ground state  $|S\rangle = |4^2S_{J=1/2}, m_J = -1/2\rangle$  (see Figure 3.4). Each photon is generated via a Raman laser pulse at 393 nm which triggers emission, by the ion, of a polarized 854 nm photon into a vacuum cavity mode, via a cavity-mediated Raman transition [78]. Two photons are generated sequentially with a time gap between the beginning of their respective Raman pulses of 13.35  $\mu\text{s}$ , such that after delay of the first (the vertical 'long-path' photon,  $|V\rangle$ ) in a 3 km optical fibre spool, both photon wavepackets (the second being the horizontal 'short-path' photon,  $|H\rangle$ ) arrive simultaneously and with their polarizations rotated to be parallel, at different input ports of a 50:50 beamsplitter. Different photon polarizations are generated and modelled by 3-level Raman transitions that differ in the final Zeeman state of the  $|3^2D_{J=5/2}\rangle$  manifold (Figure 3.4). Specifically, after the generation of a  $|V\rangle$  (an  $|H\rangle$ ) photon the ion is in the final state  $|3^2D_{J=5/2}, m_J = -5/2\rangle$  ( $|3^2D_{J=5/2}, m_J = -3/2\rangle$ ). We switch the polarisation of the generated photons by changing the detuning of the Raman laser pulse by  $\delta = 7.1$  MHz: the frequency splitting of the aforementioned transitions. In every experiment we use a Raman laser Rabi frequency of  $\Omega = 2\pi \times 64(1)$  MHz.

The arrival times of photons at the beamsplitter output ports are recorded with single-photon detectors (Figure 7.4). In each experimental cycle, we generate two pairs of photons: while the temporal wavepackets of the first pair (synchronous) arrive simultaneously at the beamsplitter, a time gap is introduced between the wavepackets of the second pair (asynchronous) that provides complete temporal distinguishability. Each full experiment consists of many repeated cycles as described in Section 7.3.4. The coincidence rates of detection events from the synchronous and asynchronous photon pairs are denoted as  $C^{\parallel}$  and  $C^{\perp}$ , respectively. A more detailed description of the data analysis for this experiment is given in Appendix A.5. The two-photon interference visibility is given by  $V(T) = 1 - C^{\parallel}(T)/C^{\perp}(T)$ , where  $T$  is the coincidence window: the maximum time difference between photon clicks that is counted as a coincidence.

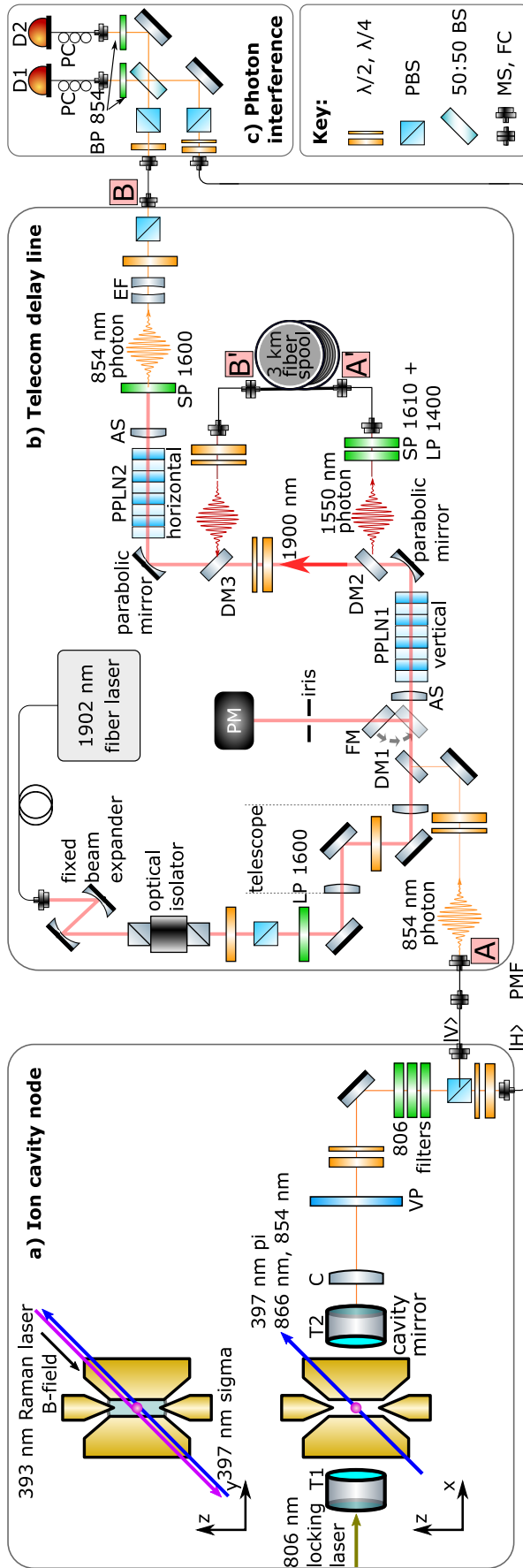


Figure 7.1: Schematic of our two-photon interference experiments. All elements used for the experiments are shown in this diagram. Detailed descriptions of the individual parts can be found in the following figures. In particular, Figure 7.2 describes the ion cavity node, Figure 7.3 the delay line and Figure 7.4 the photon interference.

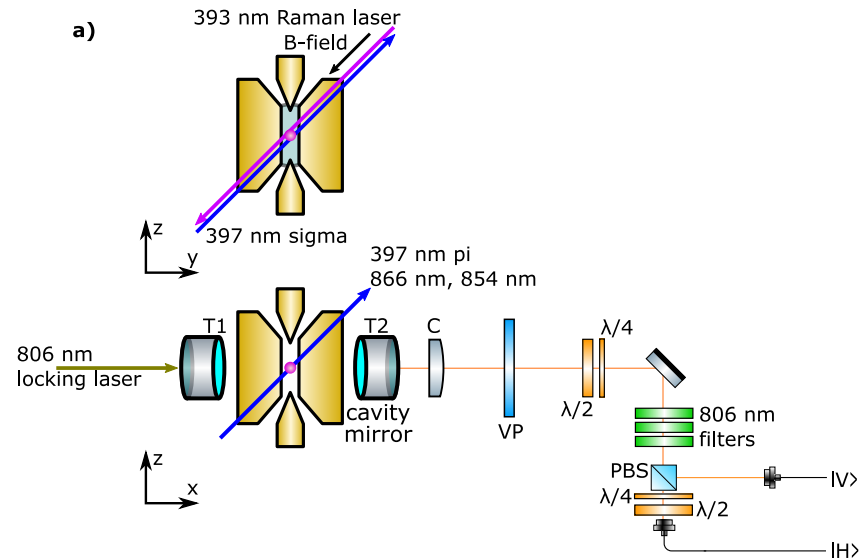


Figure 7.2: **a) Ion cavity node for the two-photon interference experiments.**

A single atomic ion (red sphere) in the centre of both a 3D radio-frequency (RF) linear Paul trap (gold electrodes) and an optical cavity. The two smaller electrodes are held at DC voltage. The 4 larger electrodes (two shown in figure projection) are driven with RF. Two cross sections are depicted: Along the cavity axis (top), showing: the  $\approx 4.229$  Gauss DC magnetic field (quantisation axis) generated by rings of permanent magnets and the circularly-polarized Raman laser for generating 854 nm cavity photons. Following a Raman pulse, an 854 nm cavity photon exits the cavity via the right mirror (transmission T2). The photon then passes the following elements: in-vacuum collimating lens (C); vacuum chamber viewport (VP); waveplates; 3 filters to remove the 806 nm laser light to which cavity length is continuously and actively stabilised; polarizing beam splitter (PBS) for directing the vertical photons into a single mode fibre, and the horizontal photons into a polarization maintaining fibre (PMF).

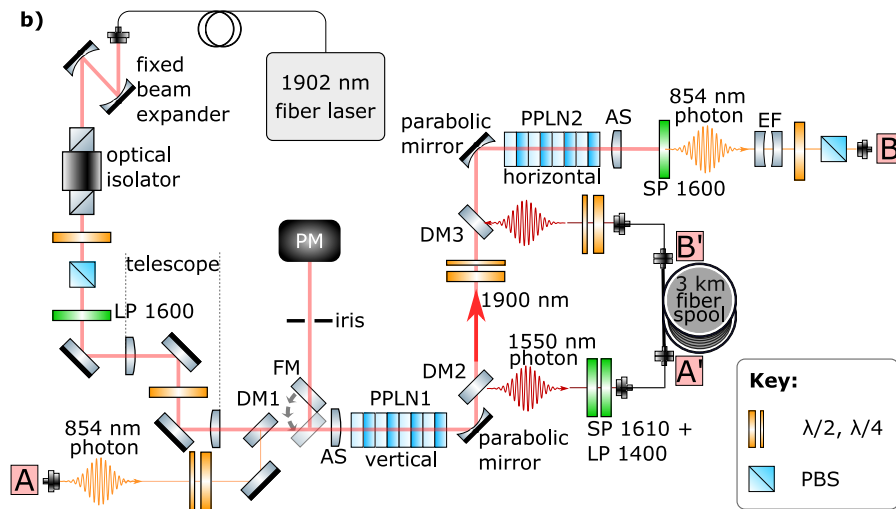


Figure 7.3: **b) Telecom delay line for the two-photon interference experiment with photon conversion.** The injected 854 nm photon (point A) passes waveplates (used for system optimization with classical light) and is overlapped with 800 mW of 1902 nm laser light (Tm-doped fibre laser, AdValue Photonics AP-SF1-1901.4-01-LP, measured at PM) on a dichroic mirror (DM1) and free-space coupled into one of the ridge waveguides of temperature-stabilised PPLN1 using an asphere (AS, 11 mm, positioned by an XYZ translation stage). The 1902 nm input path is described in 5.2.1. A gold parabolic mirror ( $f = 15$  mm) is used to collimate all fields at the output of PPLN1. A dichroic mirror (DM2; Thorlabs DMLP1800) splits the converted 1550 nm photons from the 1902 nm pump laser. A combination of a shortpass (SP 1610) and longpass (LP 1400) filter reduces unwanted pump laser and other noise light fields. The 1550 nm photon couples into the 3 km fibre spool (Corning SMF-28 Ultra), which is used as an optical delay line. The output of the fibre spool passes waveplates, to correct for polarization rotations through the fibre and is overlapped (with a dichroic mirror DM3; Thorlabs DMLP1800) back with the 1900 nm pump light, which passes waveplates to set correct pump power for the second crystal (PPLN2). Via a second gold parabolic mirror ( $f = 15$  mm) all fields are coupled into the second temperature controlled chip PPLN2, where the 1550 nm photon is converted back to the initial 854 nm via the reverse (upconversion) process. An Asphere (AS) collimates the output field, before a shortpass (SP 1600; OD5 at 1902) filters the 1902 nm pump laser from the 854 nm single photons. After passing an etalon filter (EF; LightMachinery, Bandwidth  $\sim 870$  MHz) a combination a waveplate and PBS is used to filter unpolarized noise photons before coupling the 854 nm photon into a single mode fibre (point B), which goes to the interference board.

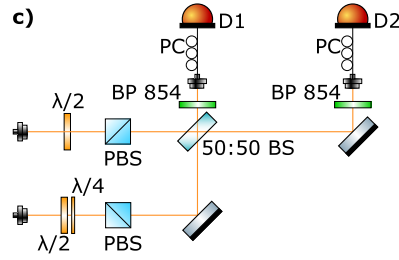


Figure 7.4: **c) Photon interference.** Both inputs pass waveplates and PBSs (cleaning polarization) and overlap on a 50:50 beamsplitter (50:50 BS). Both outputs of the beamsplitter are filtered with an 854 nm bandpass filter (BP 854); coupled to single mode fibres; polarization control paddles (PC) correct to most efficient polarization for followed single photon detector ( $D_1$  ( $D_2$ )): Scontel, efficiency 88%(87%), dark count rate  $0.5 \text{ s}^{-1}$  ( $0.3 \text{ s}^{-1}$ ). The electronic pulses produced by the detectors are detected with a time tagging module (Swabian Instruments Time Tagger 20).

In the case of perfectly indistinguishable photons entering separate ports of a symmetric beamsplitter, the well known Hong-Ou-Mandel photon bunching effect occurs: two perfect detectors placed at the output ports of the beamsplitter never fire simultaneously, resulting in  $C^{\parallel} = 0$  and  $V(T) \equiv 1$ . Yet in practice, perfect bunching is never observed, and it is important to understand the source of the imperfections. During the photon generation process, spontaneous decay events from the short-lived excited state ( $|P\rangle$ ) onto the final state manifold ( $|D\rangle$ ) act only as losses – no cavity photon is emitted through the Raman process if such an event occurs. In contrast, following any number of spontaneous decay events from  $|P\rangle$  back to the initial state ( $|S\rangle$ ) during the Raman laser pulse, a cavity photon can still be subsequently generated while the Raman laser remains on. Every spontaneously scattered photon carries away the information that the cavity photon has not yet been emitted. Consequently, the cavity photons impinging on the beamsplitter are each in a (temporally-) mixed state and therefore they do not bunch perfectly.

The results of two full 2-photon interference experiments are presented below. In the first experiment, the  $|V\rangle$  photon is sent directly to the fibre spool. In the second experiment, the  $|V\rangle$  photon is first converted to 1550 nm (telecom C band) via difference frequency generation (DFG) in a ridge-waveguide-integrated PPLN crystal with a 1902 nm pump laser. This first ‘down-conversion’ stage is described in [17, 41]. After the spool, an ‘up-conversion’ stage (not previously reported) converts the photon back to 854 nm via the reverse process: sum frequency generation (SFG). Approximately 0.2 W of pump laser power is used for each stage.

### 7.3.3 Telecom delay line efficiency and added noise

A set of characterisation measurements of the two-stage conversion process was carried out using classical laser light and the results are now described. The total efficiency from the start of the telecom delay line (Point A in Figure 7.3), to the end of the telecom delay line (point B in Figure 7.3) was measured using laser light to be  $0.098 \pm 0.005$  at the last calibration before the two-photon experiments (the error stands for the last digit of the powermeter reading).

The efficiencies of separate parts were characterized independently. The values below stand for those measured after optimization and immediately before the start of the corresponding two photon interference experiment. The given error bars are estimates of how much the value can differ based on the characterisation of the result of different optimisations done on different days. This was done to better capture the range of efficiencies expected during the lengthy two-photon experiments. First, the down-conversion stage efficiency from the point A to the in-coupling of the delay fibre was  $0.50 \pm 0.03$ , which we refer to as down-conversion external efficiency. The 3 km delay fibre transmission was measured to be  $0.6_{-0.05}^{+0.01}$  at 1550 nm, including in-coupling ( $0.75_{-0.05}^{+0.005}$ ) and two mating sleeves ( $0.95 \pm 0.02$ ). The up-conversion external efficiency (from the delay fibre out-coupler to the etalon) was measured to be  $0.53 \pm 0.03$  which includes the waveguide in- and out-coupling losses and transmission of the filter that blocks the pump field (see Figure 7.3). The etalon transmission was measured to be  $0.84_{-0.04}^{+0.005}$  and the coupling to the fibre that goes to the HOM board was measured to be  $0.73_{-0.03}^{+0.05}$ .

Now we have a closer look at the conversion efficiencies. We define the internal conversion efficiency as conversion efficiency without coupling and transmission losses, which can't be measured directly. For the upconversion we estimate a combined waveguide coupling and propagation loss efficiency of 70(5)%, limited by the mismatch of the output mode of the delay fibre and the input mode of the conversion waveguide. By taking into account those losses, an internal conversion efficiency of up to 89(0.5)% can be estimated. Note, that the external and internal up-conversion efficiencies reported here are higher than the ones achieved in similar systems before [115, 146].

On the day of the two-photon interference experiment using single photons (Figure 7.1), the total efficiency of the telecom delay line (Figure 7.3) was measured to be approximately 5%. This lower efficiency, compared to the aforementioned values achieved with classical light ( $0.098 \pm 0.005$ ) is caused by the combination of the following: an additional fibre joiner between the ion node and delay line (panels a) and b) in Figure 7.1); imperfectly optimised fibre couplers throughout the delay line; and potential slight mismatch between the photon polarization and the nonlinear crystal axes.

The noise, at the single photon level, introduced by the conversion process is now presented. These values are extracted from the photon detector click rate outside of the known ion-photon arrival times recorded in the experiment presented in Figure 7.7. Recall that final narrowband filtering is performed at 854 nm via a temperature-controlled etalon (Bandwidth 870 MHz, free spectral range 30 GHz) that has a maximum transmission of 84%. We observed  $13.3 \pm 0.7$  background counts per second on each of the detectors, where  $11 \pm 3$  cps was independently measured to be the conversion-pump-induced noise and the detectors dark count rate is  $< 0.5$  cps. From this and the known losses in the optical path between the etalon and the detectors we estimated the conversion photon noise level of  $50 \pm 10 \text{ s}^{-1}$  right after the final etalon filtering stage.

#### 7.3.4 Photon generation sequence

We sequentially generate photons of orthogonal polarizations using a cavity-mediated Raman transition with ion state reinitialisation in between. The full experimental sequence is shown in Figure 7.5. First, a  $40 \mu\text{s}$  ‘initialisation’ laser-pulse at 393 nm is measured by a photodiode in transmission of the ion-trap chamber and used for intensity stabilisation of the subsequent 393 nm photon-generation Raman pulses with a sample-and-hold system. The initialisation pulse is followed by  $2000 \mu\text{s}$  of Doppler cooling, involving three laser fields as indicated. Next, a cycle starts in which the photon-pair generation attempt takes place. This cycle is repeated (looped) 40 times before the whole sequence starts again.

In summary, each cycle contains four Raman pulses —  $V_1, H_1$  and  $V_2, H_2$  — which attempt to generate the two pairs of photons that are referred to as ‘synchronous’ and ‘asynchronous’. The first synchronous pulse pair ( $V_1, H_1$ ) has a time difference of  $13.35 \mu\text{s}$ , corresponding to the length of the delay line, such that the generated photon wavepackets arrive at the interference beamsplitter simultaneously (the delay was measured with  $< 50$  ns accuracy by recording the photon arrival times). The second asynchronous pulse pair ( $V_2, H_2$ ) has an additional delay  $t_{wait}$  and generates a fully temporally distinguishable photon pair as a reference ( $t_{wait} = 30 \mu\text{s}$ ). Before the  $V_1$  pulse in each loop we produce an electronic trigger-pulse that is recorded on a separate channel of the time-tagger, along with the photon detection events, to provide Raman pulse timing information.

In detail, each cycle starts with an additional Doppler cooling pulse ( $20 \mu\text{s}$ ) and optical pumping to the  $S_{J=1/2, m_j=-1/2}$  state via circularly polarized 397 nm laser light ( $46 \mu\text{s}$ ). The photon-generation Raman pulse  $V_1$  ( $9.4 \mu\text{s}$ , constant up to 1% variation intensity, rise/fall slope duration  $< 0.5 \mu\text{s}$ ) creates the vertical polarized photon that is directed to the delay line by a PBS. This is followed by a  $4 \mu\text{s}$  long, 854 nm

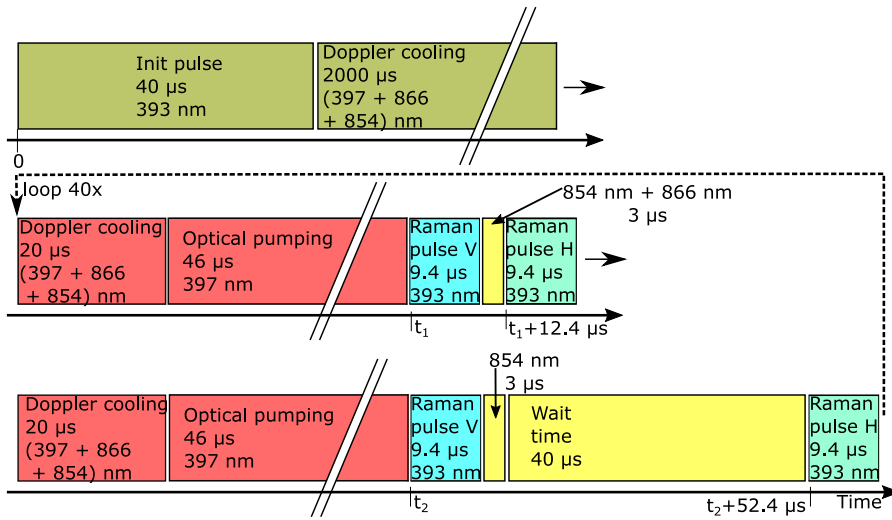


Figure 7.5: **Laser pulse sequence of our two-photon interference experiments:** Wavelengths and duration of pulses are labeled. Each cycle (what is shown within the loop) contains Doppler cooling (DC), optical pumping (OP) and four Raman laser pulses, which attempt to generate four photons. The first two are referred to as the synchronous pair and the second pair as the asynchronous pair. Each cycle is looped 40 times and this sequence is repeated thousands of times to produce the data presented.

repump pulse which pumps the ion back to the initial ground state  $S_{J=1/2, m_j=-1/2}$ . A second photon-generation Raman pulse  $H_1$  ( $9.4 \mu\text{s}$ , same profile as  $V_1$ ) creates a horizontal photon that is directed directly to the interference region. After a Doppler cooling pulse of  $20 \mu\text{s}$  and optical pumping of  $46 \mu\text{s}$ , the second pair of photons is produced.

## 7.4 RESULTS

Results are now presented for the case without photon conversion. The temporal profiles of the short-path and long-path single photon detection events from the second (asynchronous) photon pair are shown in Figure 7.6a. These single-photon wavepackets are presented as a probability density  $\rho_d(t) = N_d / (k \cdot \Delta_t)$ , where  $N_d$  is the number of detection events registered in a time bin  $\Delta_t = 125 \text{ ns}$  and  $k$  is the number of trials. Integration of the wavepackets gives the probability of detecting a short- (long-) path photon as 12.4% (2.7%). Differences in the single-photon wave packet shapes are due to slight differences in the corresponding transition strengths.

The temporal profile of the coincidence detection events (cross-correlation function) for the synchronous and asynchronous photon pairs are compared in Figure 7.6b. Here the coincidence probability density  $\rho_c(\tau)^{\parallel, \perp} = N_c^{\parallel, \perp} / (k \cdot \Delta_\tau)$  is used, where  $N_c^{\parallel, \perp}$  are the number of coincident detection events per time bin for the first and second

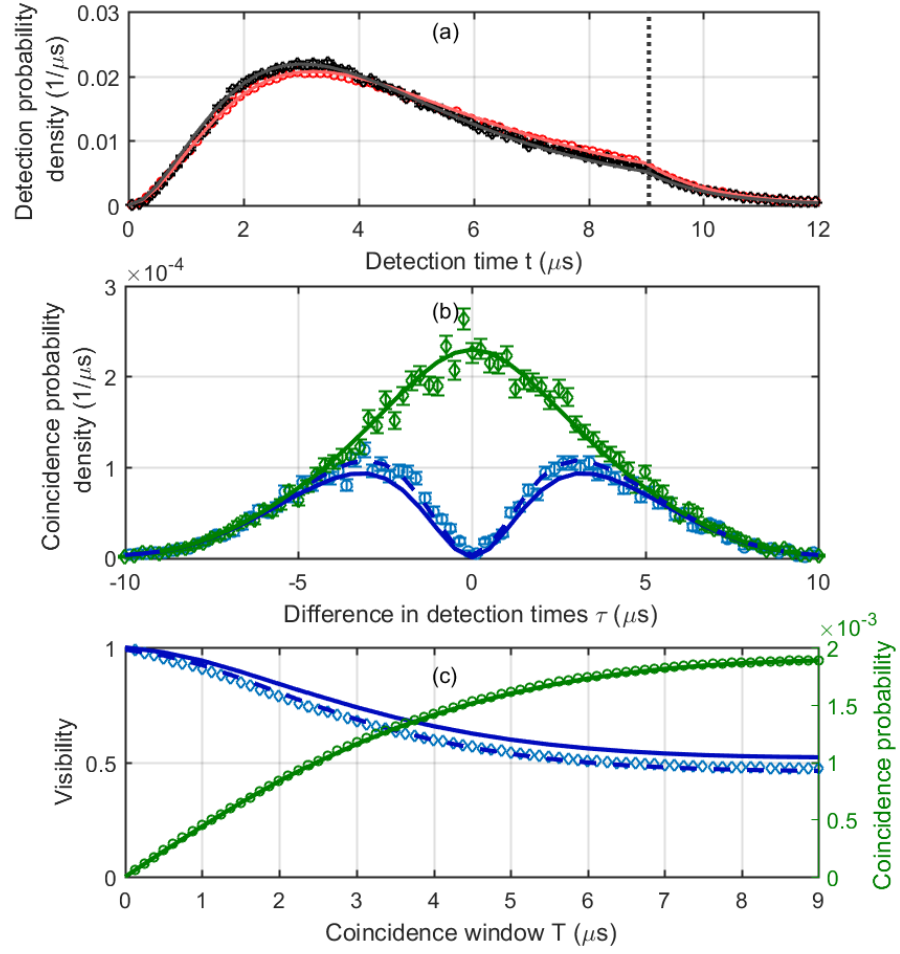


Figure 7.6: **Two-photon interference without photon conversion:** Solid (dashed) lines show basic theory (extended theory) model and shapes show data in all the panels. Probability densities are obtained by dividing the probability of detection (coincidence) per time bin by the bin size. See Appendix A.5 and supplementary material of [132] for details. (a) Single photon wavepackets for short path (red circles) and long path (black diamonds, rescaled by multiplication factor 4.6 to correct delay line losses). Vertical dotted line shows the end of the Raman laser pulse. (b) Photon coincidences for temporally synchronous ( $\rho_c^{\parallel}$ , blue circles) and asynchronous ( $\rho_c^{\perp}$ , green diamonds) cases. (c) Interference visibility  $V$  (left axis, blue diamonds) and integrated asynchronous coincidence probability  $C^{\perp}$  (green circles, right axis). Error bars represent  $\pm$  one standard deviation due to Poissonian photon counting statistics, not shown when smaller than shapes.

pair of photons respectively,  $\tau$  is the difference in detection times. Figure 7.6c shows the visibility  $V(T)$  and integrated coincidence rate of the asynchronous photons  $C^{\perp}(T) = \int_{-T}^T \rho_c^{\perp}(\tau) d\tau$ . For the smallest

coincidence window presented, the interference visibility  $V(125 \text{ ns})$  is  $0.986 \pm 0.006$  ( $0.987 \pm 0.005$  after subtracting detector dark counts). When considering a coincidence window containing the whole photon wavepacket, the visibility  $V(9 \mu\text{s})$  is  $0.472 \pm 0.008$ . From the theory, we calculate that the expectation value of the number of spontaneously-emitted photons on the  $|P\rangle \rightarrow |S\rangle$  transition, given generation of a cavity-photon, was 3.5.

The differences between the basic model and data in Figure 7.6 are consistent with an extension to the model that, in addition to spontaneous emission, includes a combination of an overall time-independent distinguishability factor of 1% and a centre frequency difference of the two photons of 40 kHz. This small photon frequency difference could be caused by several reasons, e.g., cavity length instability, acoustic noise in the 3 km delay line fibre and cavity birefringence. The 1% time-independent distinguishability can arise from slight polarization mode mismatch at the beamsplitter or imbalance of the 50:50 beamsplitter itself. The agreement between data and the basic model shows that we are close to the fundamental limit of photon indistinguishability set by spontaneous scattering in our system.

Figure 7.7 presents results for the case with photon conversion and is constructed in the same way as Figure 7.6. The probability of detecting a short- (long-) path photon across the entire wavepacket is 10% (0.5%). The visibility is  $0.96 \pm 0.04$  for the minimum coincidence window of 250 ns and  $0.37 \pm 0.04$  for the full wave packet window of 9  $\mu\text{s}$ .

For the theory curves presented in Figure 7.7 we determine  $\Omega/2\pi = 64.3(5)$  MHz,  $\Delta/2\pi = 403(5)$  MHz. The coupling reducing factor  $\alpha = 0.69(2)$  ( $g/(2\pi\beta) = 1.05$  MHz) was determined from the best fit of the simulated photon wavepacket.  $\beta$  is the product of the Clebsch-Gordan-coefficient of the 854 nm atomic transition and the projection of the polarization plane of the cavity mode onto the atomic dipole moment ( $\sqrt{10/15} \cdot 1/2$  for V photons,  $\sqrt{4/15}$  for H photons). This value is lower than the value expected from the temperature calibration measurement before the experiment ( $g/(2\pi\beta) = 1.15$  MHz) which could be caused by slight drift of the Doppler laser cooling parameters.

The differences between the basic model and frequency-converted data (Figure 7.7) are consistent with an extended model that includes a frequency drift of the unstabilized photon conversion pump laser at the level of 50 kHz on a 10  $\mu\text{s}$  timescale (consistent with independent measurements) and background coincidences, as detailed now. As in the case of the experiment without conversion, the discrepancy of theoretical and experimental visibilities, which depends on the coincidence window size, is attributed to the photons' frequency mismatch. When implementing photon frequency conversion before and after the delay line, the effect of the frequency instability of the

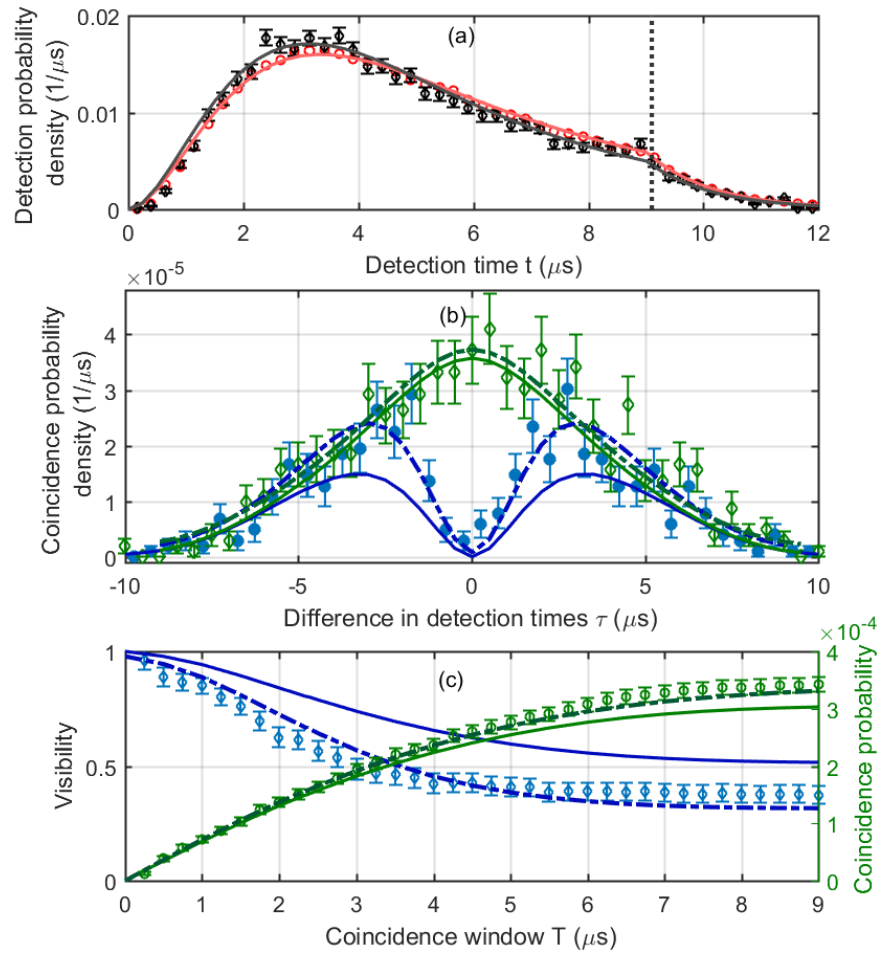


Figure 7.7: **Two-photon interference with photon conversion:** Solid (dotted) lines show basic theory (extended theory) model and shapes show data in all the panels. Probability densities are obtained by dividing the probability of detection (coincidence) per time bin by the bin size. See Appendix A.5 and supplementary material of [132] for details. (a) Single photon wavepackets for short path (red circles) and long path (black diamonds, rescaled by multiplication factor 19 to correct delay line losses). Vertical dotted line shows the end of the Raman laser pulse. (b) Photon coincidences for temporally synchronous ( $\rho_c^{\parallel}$ , blue circles) and asynchronous ( $\rho_c^{\perp}$ , green diamonds) cases. (c) Interference visibility  $V$  (left axis, blue diamonds) and integrated probability  $C^{\perp}$  (green circles, right axis). Error bars represent  $\pm$  one standard deviation due to Poissonian photon counting statistics.

unstabilized conversion pump laser (1902 nm) has to be taken into account and is the dominant effect. In our implementation there is a significant optical path length difference of  $\sim 15\mu\text{s}$  (the whole delay line) between the pump laser field and the photon (see Figure 7.1).

In that case any laser frequency drift on this time scale will result in a frequency mismatch of the short and long path photons at the interference beamsplitter. Note, however, that the constant (in time) part of the pump-laser frequency is expected to cancel out since the down and up conversion processes are symmetric. Based on the laser specification we expect  $\sim 50$  kHz instability on a  $10\mu\text{s}$  timescale, making it the dominant source of frequency mismatch.

To plot the extended-model curves in Figure 7.7 we use Equation E33 of the supplemental material of [132] with  $v(10\mu\text{s}) = 2\pi \cdot 50$  kHz and take into account the measured background-coincidence-rate by adding a constant coincidence-probability-density of  $0.8 \cdot 10^{-6} \mu\text{s}^{-1}$  (Figure 7.7b). The extended theory lines of Figure 7.7c are calculated by integrating the coincidence distributions including this background floor. The background coincidences are significant in the experiment with conversion because the signal level is  $\sim 5$  times lower. Also, the observed free-running noise counts were 13(2) cps compared to 2(2) cps per detector for the experiment without conversion due to the photon noise introduced by the frequency conversion process.

We anticipate no significant challenges to frequency stabilising the pump laser to the few kilohertz level in future work. Remote photon conversion stages in distributed networks will need independent pump lasers with absolute long-term frequency stability to within a fraction of the networking photon bandwidth.

## 7.5 DISCUSSION

The achieved visibilities and coincidence rates in our experiments could already allow for remote ion entanglement over tens of kilometres of optical fibre. Consider the entanglement swapping protocol of [83], which leads to maximal entanglement of two remote (ion) qubits with state fidelity  $F(T) = (1 + V(T))/2$  [21] at a heralded rate  $R_{\text{swap}}(T) \propto R_{\text{gen}} \times C^\perp(T)$ , where  $R_{\text{gen}}$  is the photon-generation attempt rate at each ion-trap network node. For single emitters separated by distance  $L$ , the propagation delay imposes a maximum possible entanglement distribution attempt rate of  $R_{\text{gen}}^{\text{max}} < c/L$  [41]. Using  $R_{\text{gen}} = 30$  kHz, the achieved values without photon conversion (Figure 7.6) would allow for 3 km ion-ion entanglement distribution with  $F(T = 9\mu\text{s}) = 0.736 \pm 0.004$ . Using 0.18 dB/km for telecom fibre losses and  $R_{\text{gen}}^{\text{max}} = 4$  kHz, the achieved performance with photon conversion (Figure 7.7) would allow for 50 km distant ion-ion entanglement generation with  $F(T = 9\mu\text{s}) = 0.69 \pm 0.02$  at rates on the order of 1 Hz (assuming photon detector dark count rates of 1 Hz).

The aforementioned rates and fidelities are practical values for the first observation of ion-ion entanglement over tens of kilometres. Such long-distance experiments must tackle location-dependent environmental noise in deployed optical fibres, absolute frequency

stabilization of remote laser systems and matching photons from remote network nodes. The maximum attempt rate ( $R_{gen}^{max}$ ), when using a single ion-qubit in each node, presents a strong restriction on the entanglement distribution rate: over 50 km of fibre with minimal propagation loss, and assuming perfect photon collection and conversion efficiency, the maximum rate would be 0.4 kHz. Multiplexing is a solution to overcome this limit and significantly improve rates and fidelities: to run many entanglement distribution processes in parallel, using many qubits in each node to produce or store entanglement with many parallel or closely-spaced travelling photons. In our system, time-multiplexing involving strings of tens of ions might be possible, with the depth limited by the temporal extent of the photon wavepacket. Methods to both decrease photon duration and to improve visibility, without reducing the photon generation rate, are those that can significantly increase the coherent ion-cavity coupling rate  $g$ , such as coupling multiple ions in entangled (superradiant) states to the cavity [147, 148] and recent developments in trapped-ion fibre cavities [149–151].

Our model reveals that there is an optimal drive-laser Rabi frequency ( $\Omega$ ) that achieves the highest photon generation probability (and therefore  $C^\perp$ ) for a given threshold visibility, highlighting the important role such models will play in enabling the upcoming next generation of long-distance networking experiments. Our results present a path to distributing entanglement between trapped-ion registers spaced by several tens of kilometres at practical rates for verification: significantly further than state-of-the-art experiments involving spacings of a few meters [10, 28, 141] and a practical distance to start building large-scale quantum-logic-capable quantum networks.

*Note:* During our project on two-photon interference we became aware of complementary work in which sequential interference of 866 nm photons from an ion in a cavity is achieved and studied [155].

The following text does not appear in [132] and was added during the writing of this thesis. After the measurements for the article [132] some work on the stabilization of the pump laser was done. The technique used for stabilizing the pump laser is based on an interferometer, as described in [152, 153]. The basic idea of this stabilization method is a fibre-based Michelson interferometer, where both paths have a different fibre length. We used a fibre lengths of 200 m for the long path and around 20 cm for the short path. The frequency difference of the interfering light beams equals the frequency drift of the laser during the travel time difference over both paths. One path has an additional AOM to produce an additional fixed frequency offset. The beat signal is directed to a photodiode, which creates an electronic beat signal. A feedback produced by a PID controller on a second AOM, which is placed directly after the laser output, can minimize the short term frequency drifts. The setup is similar to the one used in [154].

The stabilization currently isn't used because we don't have enough optical power to run the stabilization and the experiment at the same time. Also, the performance of the stabilisation wasn't characterized yet.



This chapter presents a way to use our setup as a quantum memory that can store established remote entanglement whilst more is made — a key step towards a quantum repeater. MM and BPL worked out the pulse sequence. MM implemented and tested the pulse sequence on the experiment. MM designed and programmed the logic board. Experimental data taking was done by VKru and MM. Data analysis and interpretation was done by MM and BPL. The project was conceived and supervised by BPL. The presented results are not published yet. I want to acknowledge Daniel Heinrich for setting up the camera detection software that is required for these experiments.

## 8.1 ABSTRACT

In this chapter two ions are used for the experiments. We demonstrate the ability to generate a photon from, and entangled with, each ion separately. We show the storage of this entanglement over many milliseconds in an ion qubit ‘memory’. The memory is a different qubit encoding in the ion than used so far in this thesis.

In Section 8.2 the importance of having the possibility to store entanglement whilst new entanglement is made will be explained. Section 8.3 will give an overview over the experiment. The necessary changes to our experimental setup are detailed in 8.4. Section 8.5 presents the experimental sequence used. The experimental results are presented and discussed in Section 8.6. Section 8.7 concludes the results and presents the next steps of this project towards the demonstration of a quantum repeater.

## 8.2 INTRODUCTION AND MOTIVATION

One main problem in realising quantum communication is the exponential loss probability of the information carriers with the length of the channel. For example, the probability that a photon successfully traverses an optical fibre reduces exponentially with the optical fibre length. A second problem is that the probability of an error occurring in the information encoded in the carrier also increases exponentially with channel length, given finite error probability per unit length. Both

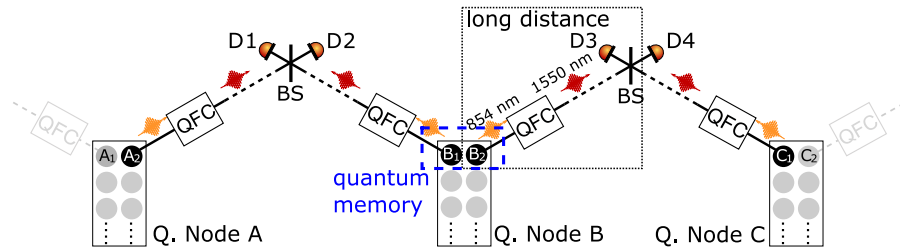


Figure 8.1: **Quantum repeater scheme for distances above 25 km:** The goal is to achieve entanglement between the quantum nodes A and C by splitting the distance into two (or multiple) smaller fractions. The scheme used in our experiments requires at least two ions in each quantum node. Photons entangled with each separately are sent in different directions aiming to establish remote entanglement with a node in a different direction. The remote entanglement is achieved via two-photon interference: coincident detection of a photon at each photon detector ( $D_1/D_2$  and  $D_3/D_4$ ) projects the remote pair of ions into an entangled state. Finally an entangling gate (e. g. MS-gate[156]) between the ions  $B_1$  and  $B_2$  followed by a logical state measurement create an entanglement between  $A_2 - C_1$ . The black dotted part of this scheme was performed in chapter 5. This section takes a closer look at the dashed blue box. This part of the scheme we call a quantum memory.

of these problems can be overcome via the quantum repeater approach of [25] proposed in Innsbruck in 1998.

A central idea of the quantum repeater is first to split the total channel length into several shorter lengths over which the transmission and error probabilities are acceptable and, second, to join the shorter lengths with repeater nodes containing multiple qubits, quantum memories and quantum logic capabilities. This chapter presents preliminary results in the direction of realising a repeater scheme consisting of a chain of quantum nodes, as shown in Figure 8.1.

In order to create entanglement in a scalable fashion between all neighbouring nodes, at least two qubits are required in each node: one to establish entanglement between the node and its left neighbour and one to establish entanglement between the node and its right neighbour. Further, those two qubits, or others in the node, should serve as quantum memories, able to store established remote entanglement until other remote entanglement is achieved.

### 8.3 OVERVIEW OF THE EXPERIMENT

In this chapter we want to test the capability of our ions to serve as quantum memories in the presence of ongoing remote entanglement distribution attempts. We use two ions spaced such that both couple to the cavity. Figure 8.2 shows conceptually how multiple ions can couple to the cavity simultaneously. A single-ion-focused Raman laser,

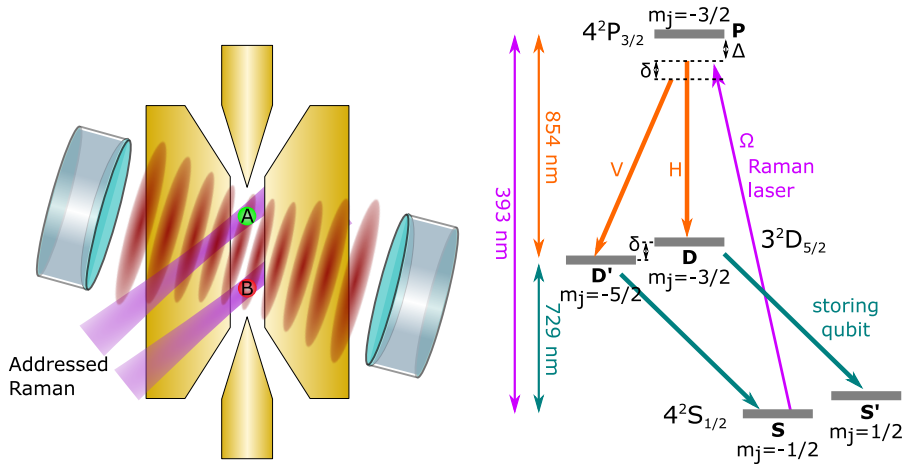


Figure 8.2: **Left: Two ions coupled to the cavity.** The cavity axis was measured to be  $4.1(1)^\circ$  [69] from being perpendicular to the ion string axis. This allows one to couple two or more ions with different fringes of the vacuum cavity standing wave at the same time for specific axial confinements of the ion string. An addressed Raman-laser can produce entangled photons from ion A and separately, from ion B. **Right: Relevant level scheme for the quantum memory.** After photon generation, the polarisation of the photon is entangled with the D/D' levels of the ion. Two 729 nm laser pulses map the states to S/S', which we call the quantum memory.

which is detailed in [157], is used to produce, sequentially, separate photons from each ion. Both photons are polarization entangled with their respective ion.

In the experiment we first produce a photon from ion A. We store the ion-state by mapping the final D/D' population into the S/S' manifold using laser pulses at 729 nm (shown as 'storing qubit' in Figure 8.2)<sup>1</sup>. This ion is called the memory ion. Next, we try several times to produce a photon from ion B, called the communication ion. Finally state tomography is performed of the both ion-photon states (both joint ion-qubit and photon-qubit states), to quantify the quality of the ion-photon entanglement.

We want to investigate how the photon detection probability of a photon produced by the communication ion evolves with increasing number of attempts to detect a photon from that ion. Also we want to investigate how the quality of the stored, and newly-generated, ion-photon states change with increasing attempt number.

<sup>1</sup> The 729 nm mapping pulses are global, not addressed. In the experiment we try to make photons from both ions sequentially, map both to memory and then try again many times on the communication ion).

#### 8.4 SETUP AND NEW HARDWARE

Two major changes of our experimental setup are implemented in order to run this experiment. First, the global 393 nm Raman beam was replaced with a single-ion-focused 393 nm Raman beam. The complete setup and details are shown in the master thesis of Marco Canteri [157]. In order to address only a single ion, the diameter of the Raman-beam on the ion has to be small enough to hit the addressed ion but not the neighbour ion. The waist of the single-ion-focused 393 nm Raman beam was measured to be  $1.3(1) \mu\text{m}$  using a single ion to profile the beam [157], while the ion-ion separation is calculated to be  $5.7 \mu\text{m}$  in this experiment. The addressed Raman beam goes through the objective that is used for ion state detection, as shown in Figure 3.3. The focus of the addressed beam is switched between neighbouring ions using an acousto-optic deflector (AOD [157]). The Raman Rabi-frequency for this experiment was measured to be  $\Omega/2\pi = 47(2)$  MHz, via the method of measuring AC stark shifts on the Raman resonance frequency [69].

The second major change is the state detection of the ion. While in the previous experiments the detector of the fluorescence light only had to distinguish between bright and dark, for this experiment the individual states of the ions have to be distinguished. Therefore, instead of the PMT a camera (ANDOR iXon Ultra) was used as shown in Figure 3.3. Together with a camera detection program, both states of the ions can be measured independently.

As shown in Figure 8.2 the cavity axis is tilted by  $\sim 4.1(1)^\circ$  with respect to being perpendicular to the ion string axis. This tilt allows the simultaneous coupling of multiple ions to different cavity vacuum standing wave nodes. The given angle leads to an ideal ion-ion separation of  $\sim 5.3 \mu\text{m}$  to couple both ions to neighbouring cavity nodes. The required end cap voltage for reaching that ion-ion distance is higher than we are comfortable with, so we stayed at lower voltages of 1100 V and 1114 V which lead to a COM frequency, measured by side-band spectroscopy, of  $963(1)$  kHz and a calculated ion-ion distance of  $5.7 \mu\text{m}$ . When setting up the experiment we optimized the photon generation efficiency for ion B, leading to a lower photon generation efficiency on ion A by a factor of  $\sim 93\%$ . The trap drive frequency used was 23.405 MHz.

#### 8.5 EXPERIMENTAL SEQUENCE

The experimental sequence is shown in Figure 8.3. The sequence starts with an 8 ms long initial pulse sequence, consisting of an intensity stabilization pulse for the Raman laser and Doppler cooling pulse. This unusually long initialization is mainly for ensuring that the cavity-length PID stabilization system has enough time in the locked regime.

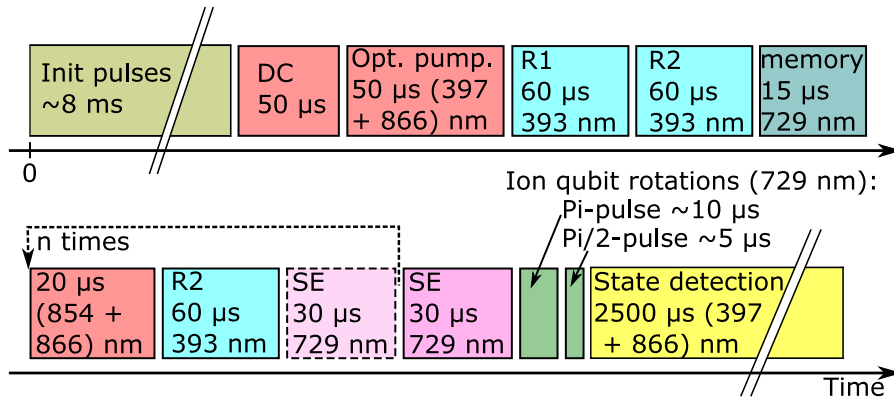


Figure 8.3: **Laser pulse sequence for the experiment.** The starting sequence (shown in green) consists of an initialisation laser pulse. This init pulse consists of pulses for intensity stabilisation and Doppler cooling. After the init pulse a short Doppler cooling (DC) and optical pumping is applied. A photon is produced subsequent from ion A (R1) and from ion B (R1). 729 nm laser pulses maps the population from D/D' to S/S'. Ion A is then used as the memory ion, ion B as the communication ion. Now the loop starts. After clearing out the remaining population from the D-states (854 nm + 866 nm), another attempt is made on the communication ion. This is repeated  $n$  times. For the  $n = 30$  and  $n = 60$  experiment a spin echo (SE) is performed after the half attempts. For the  $n = 100$  experiment three times a spin echo is performed after each quarter. After the loop another spin echo is performed to rotate the memory ion back. Then, ion qubit manipulation and state detection (shown in green and yellow) are performed to reconstruct the state. The cavity lock is turned off after the init pulse and turned back on again before the state detection.

After the initialization, the locking laser for the ion-cavity length is turned off and a sample and hold system holds the previous feedback parameters to the cavity piezos controlling the length, before another short Doppler cooling pulse and optical pumping is performed. Two subsequent addressed Raman pulses—one on ion A and one on ion B—are performed. In the ideal case, and when corresponding photons are detected, each ion-photon pair is then in the state  $\frac{1}{\sqrt{2}}(|D, H\rangle + |D', V\rangle)$  (Figure 8.2). Next two 729 nm pi-pulses, applied globally to both ions, map the D/D' qubit into the S/S' manifold, ideally preparing the state  $\frac{1}{\sqrt{2}}(|S', H\rangle + |S, V\rangle)$ . Since in the experiment we focus on analysing the cases where a photon from ion A was detected from the first Raman pulse, we therefore refer to the action of the 729 nm pulses as storing ion-qubit A (the memory ion) in memory. In cases where no photon is generated, or detected, from an ion then the electronic state of that ion is mixed. Following the 729 nm pulses, a loop starts which makes  $n$  new attempts to produce a photon from ion B (the communication ion). Each attempt consists of repumping pulses to clear out any remaining D-state population of both ions, followed

by an addressed Raman pulse on ion B. This attempt to generate a photon from ion B is expected to succeed with lower probability than the very first attempt, since ion B is not, in general, initialised in the ideal initial state ( $|S_{J=1/2, m_j=-1/2}\rangle$ ) by the repumping pulses.

Separate experiments were done for loop repetitions of  $n = 30, 60$  and  $100$ , each resulting in  $n + 1$  attempts to generate a photon from the communication ion. For the  $n = 30$  and  $n = 60$  experiments we performed a spin echo on the S/S' memory qubit manifold after half the loops. The spin echo swaps the S/S' states via three subsequent  $729$  nm  $\pi$ -pulses: S'-D, S-D and again S'-D. For the  $n = 100$  experiment, spin echos are performed after  $25, 50$  and  $75$  loops. After the last loop for all experiments another spin echo is performed such that there are always an even number of spin echos. After all loops and spin echos are complete, a  $729$  nm  $\pi$ -pulse on the S-D transition of both ions is performed, which ideally brings both ion qubits into superpositions of (different) Zeeman states of the  $S_{1/2}$  and  $D_{5/2}$  manifolds. Specifically, in cases where a photon from the memory ion was detected, the ideal final state of that ion and its photon is  $\frac{1}{\sqrt{2}}(|S'_A, H\rangle + |D_A, V\rangle)$ . In cases where a photon from the communication ion was detected in the last loop, the ideal final state of that ion and its photon is  $\frac{1}{\sqrt{2}}(|S_B, H\rangle + |D'_B, V\rangle)$ .

These final states are then analysed via  $729$  nm analysis pulses, standard electron shelving technique and the camera. Specifically, single-ion-resolved full state tomography of each ion-photon pair is performed.

## 8.6 RESULTS AND DISCUSSION

First we look into the achieved photon detection efficiency during the  $n = 100$  experiment. As a reminder, for this experiment we make one photon generation attempt on ion A, the memory ion, and then in total  $101$  photon generation attempts on ion B, the communication ion. The measured temporal photon wavepackets and detection efficiencies are shown in Figure 8.4. If you look at the first two wave packets, corresponding to the photon from the memory ion and the first photon from the communication ion respectively, you see that the detection efficiency of the communication ion is higher due to the optimization of the cavity coupling onto this ion. Starting with the third wavepacket, the photons are produced from the communication ion without optical pumping. Therefore, the detection efficiencies of these attempts are lower compared to the second wavepacket. Also, a longer time gap between wavepacket two and wavepacket three is visible which corresponds to the time required to map the memory ion qubit into the  $S_{1/2}$  manifold. The gaps after the  $27^{\text{th}}$ ,  $52^{\text{nd}}$  and  $77^{\text{th}}$  wavepackets correspond to the times needed for the spin echo sequence. The wavepacket shapes from the different attempts don't

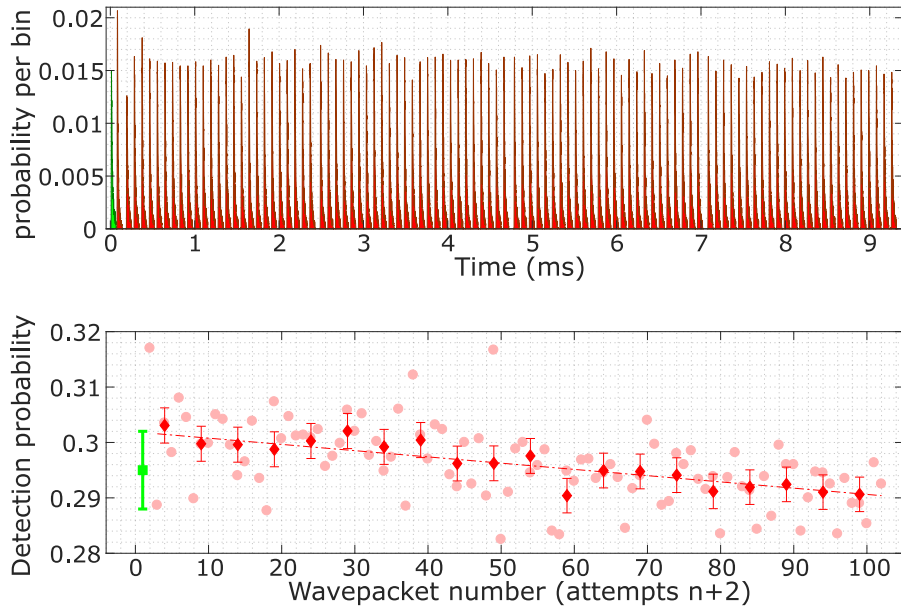


Figure 8.4: **102 Wave packets in a row.** The upper figure shows the temporal photon detection distribution of the experiment, where the communication ion had 101 photon production attempts. The first, green wave packet corresponds to the wave packet from the memory ion, followed by 101 wave packets from the communication ion (red). The lower figure shows the total detection probability per wave packet. Again, the first green point corresponds to the photon from the memory ion. The light red points indicates each single attempt, where the red points with the error bars are the calculated mean value of the 5 neighbouring points. The memory ion detection efficiency is lower than the first communication ion attempts, because the communication ion is better centred in the cavity. The communication ion detection efficiency decreases by  $1.1(2) \cdot 10^{-4}$  per attempt as indicated with the red dashed linear regression line.

differ significantly given measurement statistics based on Poissonian photon counting.

Figure 8.4b shows that the detection efficiency for a photon from the communication ion decreases with increasing number of attempts. The slope of a linear fit function from the 3<sup>rd</sup> to the last wavepacket is  $-1.1(2) \cdot 10^{-4} n^{-1}$  which correspond to the fractional reduction in photon detection efficiency per attempt on the memory ion. The error budget for the slope was calculated by a Monte-Carlo approach as described now. 500 different datasets for the 100 wavepackets used for fitting the slope were randomly generated with a Poissonian distribution over the measured detected counts from each wavepacket. The generated counts were divided by the number of total attempts to get the detection probability. For each dataset the linear fit function was calculated. The final slope with its inaccuracy equals the mean value and the standard deviation of the 500 fit functions. We

anticipate two dominant causes of the decreasing detection efficiency with attempt number. First, by switching off the cavity lock during the experiment to avoid AC Stark shifts from the locking laser on the memory qubit, the ion-cavity coupling is expected to reduce as the number of attempts increases as the cavity length drifts. The lower ion-cavity coupling results into lower photon generation efficiency. Second, the laser pulses used for all the photon generation attempts heat up the motional states of the ion string via photon absorption and scattering. Without cooling between the attempts, the total phonon number of the ion-string motional modes will increase, which again decreases the ion-cavity coupling and the coupling of the Raman laser and ionic carrier transitions. These size of these effects have not yet been quantified directly and this is left for future work. Overall, the efficiency after 101 attempts is still "impressively high".

In addition to the detection probability, we look into the evolution of the state quality of the ion-photon pairs involving each ion. Due to decoherence effects we expect a change of the memory ion-photon state over time, which leads to loss in entanglement. The fidelities of the tomographically-reconstructed ion-photon density matrices with their nearest maximally-entangled two qubit state are shown in Figure 8.5, for a range of different loop numbers ( $n$ ).

Figure 8.5 also shows ion-photon state fidelities obtained from a repetition of the experiment performed without spin echos. One sees that the spin echo technique helps to significantly reduce the fidelity decay of the memory ion-photon state. However, even in the case of spin echos, fidelity decay with attempt number is clearly visible. Remaining decoherence of the memory ion-photon state is attributed by us entirely to decoherence of the memory qubit. Possible causes include motional heating of the ion string limiting the quality of subsequent laser pulses including spins echos and those in state reconstruction. More investigation would be necessary to pin down and quantify the main contributions. Still, the fidelity of the memory ion-photon state to the next maximum entangled state after 101 attempts on the neighbouring communication ion is  $F^m(n_{100})=0.76(1)$  and therefore far above the 0.5 threshold for separable states. Rotations of the ion-photon state that do not change the entanglement content are not captured by the fidelities presented in Figure 8.5 (where always the nearest maximally entangled state is considered). In order to check for such rotations between states produced in different attempts, the fidelity between the reconstructed *memory* ion-photon states for different attempt numbers are calculated. The fidelity between the reconstructed state with  $n = 31$  attempts and  $n = 61$  attempts is  $F(n_{30}, n_{60}) = 0.97(1)$ . The fidelity between the reconstructed state with  $n = 31$  attempts and  $n = 101$  attempts is  $F(n_{30}, n_{60}) = 0.95(1)$ . This indicates that the state of the memory ion is not significantly rotating over time, even in the presence of up to 101 Raman laser pulses on the neighbouring ion.

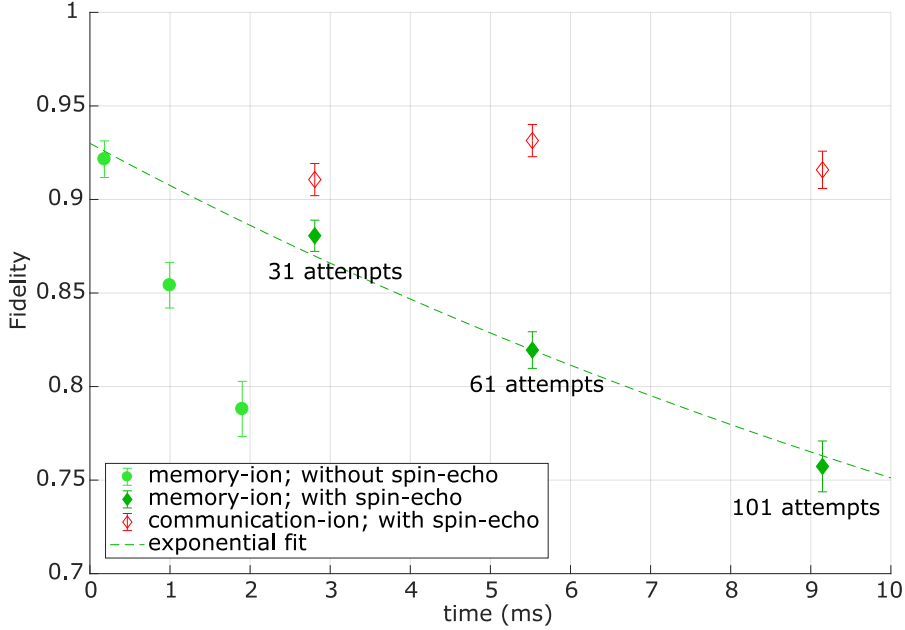


Figure 8.5: **Fidelity of ion-photon entanglement during the memory experiment.** Fidelities of the reconstructed ion-photon states against the storage time of the memory ion (green shapes), for different numbers of attempts ( $n$ ) to generate photons from the communication ion (red shapes). Fidelities are calculated to the nearest maximally-entangled 2-qubit state. The experiments with  $n = 31$  and  $n = 61$  attempts are done with one spin echo, the experiment with  $n = 101$  attempts was done with three spin echos. Fidelities without spin echos are shown for  $n = 2$ ,  $n = 11$  and  $n = 21$  attempts. The dashed lines shows an exponential fit for the decoherence of the fidelity that involves the memory ion with spin echos. The fit-function  $F = Ae^{-t/\tau} + 0.5$  applied on the 4 measurement points  $n = 2, 31, 61, 101$  results in  $A = 0.43(1)$  and  $\tau = 18.6(4) \text{ ms}^{-1}$ . Therefore, the fidelity of the memory-ion-photon state decays by  $0.20(1)\%$  per attempt, when using spin echos. For longer storage times the fidelity of the ion-photon state in memory drops while the communication ion-photon fidelity stays constant to within statistical precision, at over 90%.

The results of preliminary experimental runs in this project, not presented here, revealed a strongly rotating ion-photon state when stored in memory. This was due to a mistake in setting the 393 nm bichromatic frequency difference, which should ideally match the frequency splitting of the D/D' states ( $\delta_{393} = \delta_{729}$ , as described in Section 3.5.2). After finding this mistake we looked into older results and found that it had happened previously in the 100 km entangling experiment as described in Section 5.4. This mistake doesn't change the conclusions of that section, but likely contributed to a reduction of about 10% in the achieved ion-photon state fidelities.

## 8.7 CONCLUSION AND OUTLOOK

We demonstrated the ability to store entanglement with a remote photon in one ion-qubit, while up to 101 attempts took place to generate a new photon entangled with a neighbouring ion-qubit. Moreover, the efficiency and entangled state fidelity of that neighbouring ion-photon state was not significantly reduced. The entangled state fidelity of the stored ion-photon state is seen to reduce and the origins of this effect requires further investigation in order to design methods to further reduce it.

The next steps towards a quantum repeater node are presented now. Most of these next steps presented here are already done in the lab, but are beyond the scope of this thesis, and we hope will be published soon. One important step from the presented 'memory' experiment towards a full quantum repeater is to switch the photons from the different ions into different paths. This can be done either with a 50:50 beam splitter, with the drawback of losing at least 50% efficiency, or with an electro-optical switch. The switch can be driven from the PulseBox in order to direct the desired photon into the desired path.

Another step would be to swap the two ion-photon pairs to photon-photon entanglement between the memory-photon and the communication photon, thereby simulating entanglement swapping to remote nodes. In order to swap the entanglement to the photons, an entangling gate, like the MS-gate [156], could be performed on the ions. One challenge here is that after production of photons from the memory ion and communication ion, the two ion-qubits are left in different Zeeman states (as described in 8.5). However, established MS-gates required encoding in the same qubit states. This can be achieved by developing a single-ion-qubit manipulation laser and that is currently underway in our group.

The third step to a long distance quantum repeater would be to combine the memory with the conversion setup and a long fibre (see Sections 4 and 5) to enable the distribution of ion-entangled photons to distant remote nodes "to the left and to the right". The lower photon distribution probabilities and the extra light travel time will increase the performance requirements of the integrated memory: more attempts and greater coherence times will be desirable. In order to boost the memory time, it would be useful to implement conditional spin echos. For example, after a defined number of attempts, a spin echo is performed.

The final experiment would be to combine all these steps together: Producing two photons, each from a different ion, where the first ion that leads to a photon detection event stores the information (remote entanglement), while the other ion makes new entanglement distribution attempts. The two photons are converted to telecom wavelength and switched to different, long fibres. An entangling gate between the

ions then swaps the entanglement to the two photons, which have travelled to two different places, tens to hundreds of kilometres apart.

There is, of course, even one step further step: entangling remote ions via entanglement swapping heralded by photon detection. During the writing of this thesis, our group and that of Tracy Northup achieved entanglement of our ion with an ion in their similar setup in a building some 400 m away, heralded via two-photon interference. Combining that work with the telecom interface and memory results in this thesis points towards the near-term possibility of entangling atomic ions over tens to hundreds of kilometres.



## CONCLUSION AND OUTLOOK

---

In the introduction 7 key questions that set out to answer in my PhD studies are raised. Here is a summary of the answers to those questions, in the light of the results detailed in the previous chapters.

**Efficiency of the conversion process.** We achieve a maximum *waveguide conversion efficiency* to 1550 nm of  $0.59 \pm 0.03$ , for a linearly polarised input 854 nm light field (Section 4.2). This efficiency is defined as the ratio of the number 1550 nm photons leaving the waveguide to the number of 854 nm photons sent at the waveguide. The upper limit for single polarization conversion is set by in-coupling and transmission losses through the waveguide. Assuming the same in-coupling and transmission losses for 1550 nm as we measured for 854 nm, this upper limit is estimated to be  $0.89 \pm 0.04$  for the waveguides that we used. From observations of the waveguide output mode at 854nm, we conclude that the difference between the achieved waveguide efficiency and the upper limit is due to the excitation of higher order modes on in-coupling 854 nm into the waveguide. By chaining two conversion waveguides, we achieved a polarization maintaining converter with a *device efficiency* of 30%. The device efficiency is the probability for converting a 854 nm single-mode-fibre-coupled photon into a 1550 nm single-mode-fibre-coupled photon. For the device efficiency, in addition to the excitation of higher order modes, the passive optical losses of the used optical elements are a limiting factor.

**Added noise through conversion.** The free-running noise photon rate added from the conversion process is  $58 \pm 4$  counts per second in the single mode fibre at the output of the polarisation preserving conversion device. This rate was achieved within a filtering bandwidth of 250 MHz. A detailed study revealed that the noise added by the conversion process is anti-Stokes Raman scattering of the strong pump laser inside the nonlinear crystal. Since the noise is seen to be white around our filtering bandwidth, we expect that narrower filtering will further reduce the noise in proportion. Since the photons generated in this thesis have, up to frequency fluctuations of the pump laser, sub-MHz bandwidth, significantly tighter filtering would not cause reductions in the transmission efficiency. Nevertheless, efficient filtering at the MHz bandwidth level is challenging. A separate approach to reduce anti-Stokes Raman scattering would be to reduce the temperature of the waveguide (and modify the quasi-phase matching accordingly). For example, moving from the current phase matching temperature of 38 °C, to -50 °C is expect to provide a total noise reduction factor of 9.

**Preservation of single photon character.** The preservation of the single photon character was assessed by measuring the second order correlation function of the light before and after conversion. We measured  $g_{854}^{(2)}(0) = 3.1(8) \cdot 10^{-3}$  for the unconverted 854 nm photons. This value is predominantly limited by the noise photons from the background room light. No imperfection of the ion-cavity system that leads to a non-zero  $g^{(2)}(0)$  could be resolved in the data. A better shielding of the photon detection paths from room lights is expected to allow for a  $g_{854}^{(2)}(0)$  value of  $3(1) \cdot 10^{-4}$ , at which point detector dark counts (0.3(1)/0.5(1) per second) are the limit. For converted 1550 nm photons we measured  $g_{1550}^{(2)}(0) = 0.18(3)$ . The offset from 0 is consistent with the measured background noise rates. The main noise contributions in this experiment are anti-Stokes Raman scattering of the pump laser and background room light. A better shielding of the background light is expected to yield down to  $g_{1550}^{(2)}(0) = 0.07(1)$ . Further improvements can be achieved by increasing the conversion efficiency or lowering the anti-Stokes Raman noise, as described in the previous points. Another important factor is the length and shape of the photon wavepacket. A slightly smaller window would keep most of efficiency while decreasing noise probability, which leads to a significantly lower  $g^{(2)}(0)$ . Here there is a trade off between decreasing  $g^{(2)}(0)$  and increasing the single photon detection efficiency.

**Preservation of the photonic qubit state.** Up to fixed unitary rotations, the quantum process implemented by the conversion stage on the input polarisation, of 854 nm laser light, was found to have a fidelity of 0.95(1) with the identity operator. Quantum process tomography for input single photons was not carried out, although we do not expect any significant difference in performance, up to the noise added by the pump laser.

**Preservation of photon indistinguishability.** We demonstrated a Hong-Ou-Mandel interference experiment between two sequentially-produced 854 nm, to test the indistinguishability of our photons. In the first experiment these photons came directly from the ion-cavity system, without conversion. In the second experiment the first photon was converted to 1550 nm, sent through a 3 km long delay fibre and converted back to 854 nm before being overlapped with the unconverted second photon on a beamsplitter. We refer to that experiment as the 'converted' case. For the unconverted case a two-photon HOM interference visibility of  $V = 0.472 \pm 0.008$  was measured for a coincidence window of 9  $\mu$ s, which includes the entire photon wavepacket. That value is consistent with the predictions of a model that considers spontaneous scattering from the ion as a source of distinguishability, up to a small correction due to, perhaps, a length drift of the optical cavity between the times of sequential photon emissions. For the converted case we measured a visibility of  $V = 0.37 \pm 0.04$ . To within statistical precision, the drop in visibility for converted photons is con-

sistent with a model that considers a frequency drift of the pump laser of 50 kHz over 10  $\mu\text{s}$ , which corresponds to the time between Raman pulses that generate the two sequential photons. As such, we expect that frequency stabilising the pump laser should return the visibility to the value before conversion. No further effect of the converter on the distinguishability of the converted photons was detected.

**Entanglement between telecom-photon and ion.** We demonstrated the preservation of entanglement between an ion qubit and photon polarisation through the telecom conversion process. State tomography of the ion-photon pair qubit pair before and after the conversion shows no reduction in the fidelity to a maximally-entangled state to within statistical uncertainty. For unconverted photons a fidelity of  $F^m=0.967 \pm 0.006$  with a maximally-entangled two-qubit Bell state was achieved. The equivalent fidelity achieved for converted photons of  $F^m=0.971 \pm 0.007$  is not significantly different. New experiments would have to be designed and carried out to isolate the remaining sources of percent-level infidelity, probably using randomised benchmarking to eliminate state preparation and measurement errors.

**Distribution of light-matter entanglement over tens of kilometres.** The telecom ion-entangled photons were coupled into a long fibre spool before the ion-photon state was analysed. For a 50 km fibre spool, where the photon had a travel time of  $\sim 250 \mu\text{s}$ , we achieved a fidelity of  $F^m=0.86 \pm 0.03$  with a maximally entangled state. For a 100 km fibre spool, where the photon has a travel time of  $\sim 500 \mu\text{s}$ , we achieved a fidelity of  $F^m=0.77 \pm 0.04$ . Both states are entangled since they beat the 0.5 fidelity threshold, for non-entangled states, by more than 6 standard deviations. Various entanglement measures also confirm positive entanglement, which are available from the density matrix reconstruction. For the 50 km experiment, the fidelity of the state is limited by the detector dark count rate. For the 100 km experiment the main contribution to the infidelity was a rotation of the ion qubit state during the experiment caused by a mistake in setting the frequency of the photon generation Raman laser pulse. For the 100 km distribution, the total detected efficiency for the photon was  $7.0 \pm 0.3 \times 10^{-4}$ , which compares with an expected value of less than  $10^{-30}$  using photons at the unconverted 854nm wavelength.

**Towards a trapped-ion quantum repeater node.** In addition to the key questions announced in the introduction, Chapter 8 presented preliminary results demonstrating new functionalities required for the quantum repeater protocol in trapped ions. Here, two neighbouring ions in the trap were each entangled with a separate propagating photon. One of the ions served as a qubit-memory, storing correlations with a first detected photon, whilst repeated photon generation attempts were performed on the the other 'communication' ion. We found that even after 100 attempts to distribute a photon entangled with the communication ion, taking over 9 ms, the state stored in the

memory ion qubit and its photonic qubit is still clearly entangled. This proves firstly that our quantum memory functions for at least 9 ms in the presence of over 100 nearby photon generation attempts. Secondly, we see that the efficiency of the photon generation process is only marginally reduced even after so many photon generation attempts, which add heat to the ion string via photon recoil. While these preliminary results demand more careful analysis and investigative experiments, they are very promising for the realisation of a quantum repeater over tens of kilometres with trapped ions.

#### OUTLOOK

Following the work in this thesis, ion-photon entanglement over up to 100 km of optical fibre has been proven. A significant step would be to use this capability to achieve entanglement between ions separated by tens of kilometres, according e. g. to the entanglement swapping schemes of [25, 158], as shown in Figure 8.1. Here, several issues have to be solved. First, in order to send the photon to a place far away from the ion-cavity setup, one has to use the existing telecom network. Therefore, a polarization stabilization for the fibre has to be designed. This could be done for example with a second stabilizing laser on a different telecom wavelength. Second, when swapping the ion-photon entanglement to an ion-ion entanglement it would be beneficial, for the success rate and the achieved fidelities, to stabilize the pump laser frequency to below the ideal photon bandwidth (of a  $\sim 100$  kHz) to increase the HOM-visibility of the converted photons.

The basic principles of a trapped ion quantum repeater node have been investigated in the quantum memory experiment in Chapter 8. The next steps of that project are the switching of the generated photons to different paths, the swapping of the two ion-photon entangled pairs to photon-photon entanglement (mimicking future remote ion-ion entanglement) and the combination of the QFC and long fibres. During the writing of this theses, some of these steps have been taken in the lab, led by our postdoc Victor Krutyanskiy.

This experiment again could be combined with two other ion-cavity nodes and therefore the photon-photon entanglement could be swapped to an ion-ion entanglement of these two remote nodes. Finally, our ion-cavity system seems capable of stably trapping strings of at least ten ions and therefore the experiments presented here can be extended in terms of ion-qubit numbers in the node. This work is currently being pursued by new PhD students James Bate and Marco Canteri.

APPENDIX

---

## A.1 PULSEBOX

In our experiments we use the PulseBox V2 in combination with TrICS (Trapped Ion Control System). The PulseBox is an FPGA-based control device, which can provide 32 different TTL output signals and up to 9 programmable DDS output signals. It also can react on 8 different input TTL channels. The PulseBox is referenced to a 10 MHz external clock signal. At IQOQI that signal is provided by a Rb-referenced quartz oscillator, that is distributed in the wall sockets around the labs. Programming of the PulseBox is done via an Ethernet connection with the 'control PC', where the home-developed software program 'TrICS' is run, which is the tool to program the FPGA from the PulseBox for each experiment.

More details about the **PulseBox** can be found in the internal UIBK wiki and in the diploma thesis of Philipp Schindler [159]. More details about **TrICS** and the **Sequencer** can be found the UIBK git repository and in the thesis of Daniel Heinrich [160].

## A.2 CONDITIONAL LOGIC BOARDS

The FPGA based logic boards in our experiments are used to branch into different sequences, executed by the PulseBox, conditional on photon detection events. We call these boards 'conditional logic boards'. The main purpose of the logic boards is to broaden the electronic pulses sent by our single photons detectors, from their initial length of approximately 100 nanoseconds to several microseconds which is sufficient to trigger the PulseBox. In addition, the boards also provide basic logic features which, e. g. , help to prevent noise photons (clicks outside the known arrival windows of photons from the ions) from triggering the pulse box. The PulseBox branches the sequence that it is executing conditional on the output signal from a logic board.

A circuit diagram of the conditional logic board used for the long distance ion-photon entanglement experiments that are reported in Chapter 5, is shown in Figure A.1. This board has four digital inputs (Reset, Photon1, Photon2 and Gate) and one digital output (Out). The inputs Photon1 and Photon2 are connected with the outputs of the single photon detectors. If only one detector is used, one of the inputs is grounded to 0. The Gate and Reset inputs are connected with a TTL output of the PulseBox and can be controlled with the sequence. The output Out is connected to a TTL input of the PulseBox.

The main building block of all conditional logic boards is the D flip-flop. The truth table for the D flip-flop is shown in Table A.1. This table shows, that the logic reacts on raising edges and has the ability to store previous states (last row). For our usage we set the D input and the CLR input of the flip-flop constantly to 0. Therefore, the PR input of the flip-flop resets the flip-flop and a rising edge of the CLK input change the output  $\bar{Q}$  to high. If both inputs are 0, the output of the flip-flop keeps the previous state.

Input				Output	
PR	CLR	CLK	D	Q	$\bar{Q}$
1	0	X	X	1	0
0	1	X	X	0	1
1	1	X	X	X	X
0	0	↑	1	1	0
0	0	↑	0	0	1
0	0	0	X	$Q_0$	$\bar{Q}_0$

Table A.1: Truth table for a D flip-flop. X stands for arbitrary input, ↑ for raising edge and  $Q_0/\bar{Q}_0$  for holding the previous state. This memory feature will be used for keeping the output on high, until the PulseBox could read out the state. In our conditional logic board the inputs PR and D are constantly set to 0.

The input logic to the CLK input of the flip-flop is used to filter noise photons outside of the expected photon arrival time. The OR gate (Figure A.1) lets the circuit react to photon detection events from either detector. The AND gate of the photon inputs lets the circuit react only to photons inside a specific gate (time window). The truth table of the whole logic board is shown in Table A.2. The basic working functionality of the conditional logic board is shown in Figure A.2.

Input				Output
Photon1	Photon2	Gate	Reset	Out
X	X	X	1	0
↑	X	1	0	1
X	↑	1	0	1
X	X	0	0	Out <sub>0</sub>
0	0	X	0	Out <sub>0</sub>

Table A.2: Truth table for the conditional logic scheme. X stands for arbitrary input, ↑ for raising edge and Out<sub>0</sub> for holding the previous state. The first row shows the effect of having reset on high: Out is reset to 0. The second and third row shows a photon detection event when the gate is high: Out is set to 1. The two last rows shows what happens outside a gate or when no photon detection event happens: Out keeps the previous state.

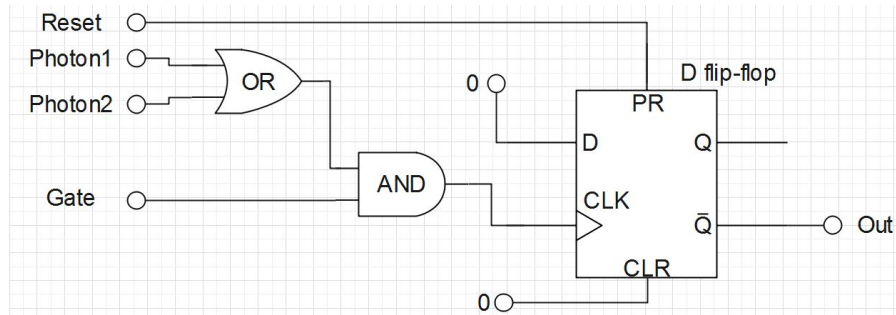


Figure A.1: **Conditional logic scheme for 50 km ion-photon entanglement experiment:** The OR gate let the flip-flop react on both photon detectors. The AND gate lets the flip-flop react only during the expected photon arrival time provided by the 'Gate' input. The D flip-flop extends the short (~ 100 ns) electric pulse from the single photon detectors input into 'Photon1' and 'Photon2', such that the PulseBox can read out the state via 'Out'.

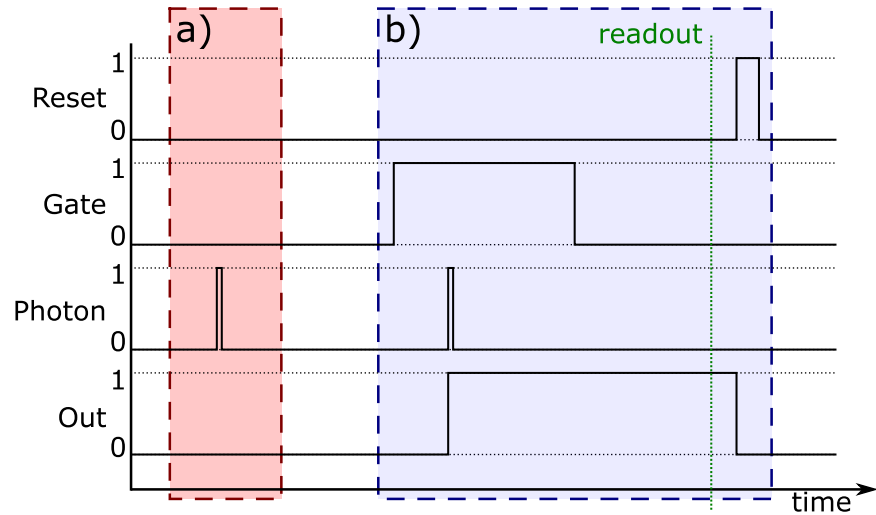


Figure A.2: **Example of the functionality of the conditional logic board of Figure A.1:** **a)** An electric pulse from a single photon detector signals a detection event (either Photon1 or Photon2). The photon detection is outside the gate (gate input is 0), so the output stays low (0). **b)** A electric pulse from the single photon detector signals a detection event. Here the photon detection happened inside the gate (gate input is 1 at the time of photon detection), so the output changes to high (1) and stays at this value. Other photon detection events (not shown in this example) inside or outside the gates after the output changed to high (1) doesn't effect the logic. This storing of the output in high (1) enables a readout of this state from the PulseBox. A reset pulse changes the output back to 0.

A.3 STANFORD CHIPS LAYOUT

The following pictures were kindly provided by Carsten Langrock from the group of Martin Feyer from Stanford University. Figure A.3 shows the manufacturing process of the nonlinear waveguide chips used. Figure A.4 shows a close-up schematic of one waveguide. Figure A.5 shows the common device specification of the provided fibre-coupled converters.

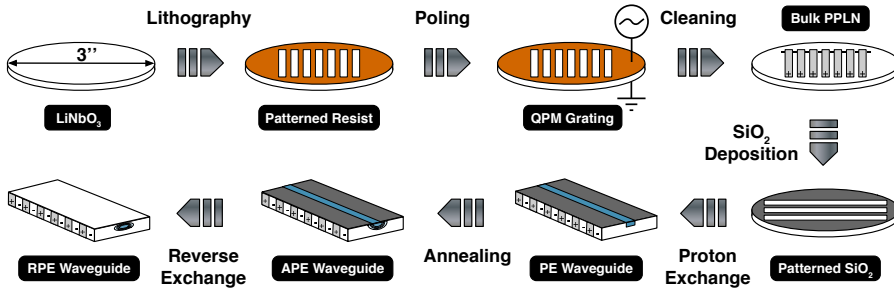


Figure A.3: Manufacturing process used for the provided fibre coupled waveguides. This picture is kindly provided by Carsten Langrock from the group of Martin Feyer from Stanford University

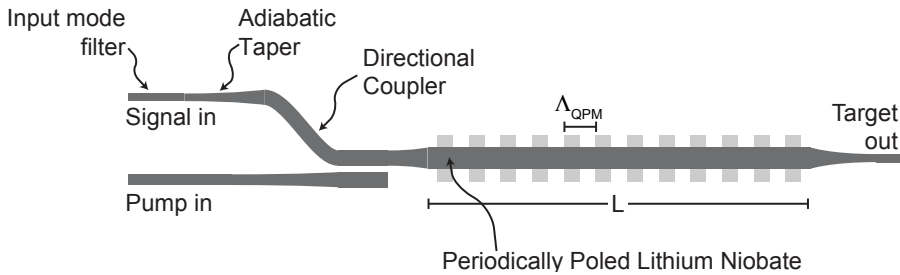


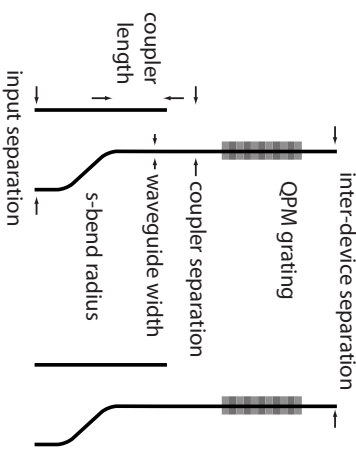
Figure A.4: Close-up schematic from one fibre coupled waveguide. This picture is kindly provided by Carsten Langrock from the group of Martin Feyer from Stanford University

# M27 - SciNet ARL Project

## Downconversion of 854-nm photons (Ca<sup>+</sup> ion trap) to C-band

### Common device specifications

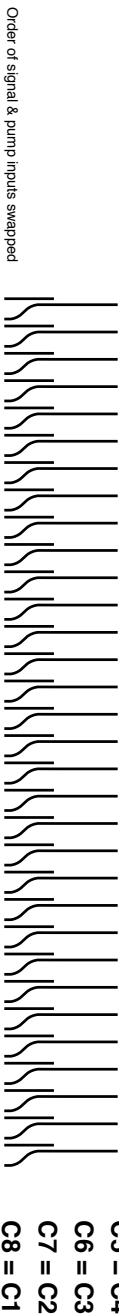
- device length: 52 mm (C1 - C3, C6 - C8), 67 mm (C4, C5)
  - signal / pump wavelength: 854 / 1901 nm
  - modelfilter / taper length: 2.0-mm-long mode filters, 1.5-mm-long tapers
  - waveguide test structures: none
  - inter-device separation: 180  $\mu$ m
  - waveguides per chip: 32
- on-chip WDM parameters
- input separation: 127  $\mu$ m
  - coupler separation: 10  $\mu$ m
  - waveguide width: 5.6  $\mu$ m
  - s-bend minimum radius: 10 mm



### Device layout (C1 - C4)

QPM period	Waveguide width	Modelfilter width (output)	Coupler length	Modelfilter width (signal / pump)	Modelfilter width (signal / pump)	Modelfilter width (output)
3.4	8.5	19.8	C1 (baseline)	2.6 / 4.4	0.8	3.6
3.4	9.0	19.8		2.6 / 4.4	0.8	3.6
3.4	9.5	19.8		2.6 / 4.4	0.8	3.6
3.4	10	19.8		2.6 / 4.4	0.8	3.6
3.4	8.5	19.9	C2 (diff)	2.6 / 4.4	0.8	3.6
3.4	9.0	19.9		2.6 / 4.4	0.8	3.6
3.4	9.5	19.9		2.6 / 4.4	0.8	3.6
3.4	10	19.9		2.6 / 4.4	0.8	3.6
3.4	8.5	19.8	C3 (diff)	2.6 / 4.4	0.9	3.6
3.4	9.0	19.8		2.6 / 4.4	0.9	3.6
3.4	9.5	19.8		2.6 / 4.4	0.9	3.6
3.4	10	19.8		2.6 / 4.4	0.9	3.6
3.4	8.5	19.9	C4 (diff)	2.6 / 4.4	0.9	3.6
3.4	9.0	19.9		2.6 / 4.4	0.9	3.6
3.4	9.5	19.9		2.6 / 4.4	0.9	3.6
3.4	10	19.9		2.6 / 4.4	0.9	3.6
3.6	8.5	19.8	C5 = C4	2.8 / 4.4	0.8	3.4
3.6	9.0	19.8		2.8 / 4.4	0.8	3.4
3.6	9.5	19.8		2.8 / 4.4	0.8	3.4
3.6	10	19.8		2.8 / 4.4	0.8	3.4
3.6	8.5	19.9	C6 = C3	2.8 / 4.4	0.8	3.4
3.6	9.0	19.9		2.8 / 4.4	0.8	3.4
3.6	9.5	19.9		2.8 / 4.4	0.8	3.4
3.6	10	19.9		2.8 / 4.4	0.8	3.4
3.6	8.5	19.8	C7 = C2	2.8 / 4.4	0.9	3.4
3.6	9.0	19.8		2.8 / 4.4	0.9	3.4
3.6	9.5	19.8		2.8 / 4.4	0.9	3.4
3.6	10	19.8		2.8 / 4.4	0.9	3.4
3.6	8.5	19.9	C8 = C1	2.8 / 4.4	0.9	3.4
3.6	9.0	19.9		2.8 / 4.4	0.9	3.4
3.6	9.5	19.9		2.8 / 4.4	0.9	3.4
3.6	10	19.9		2.8 / 4.4	0.9	3.4

### Device layout (C5 - C8)



Order of signal & pump inputs swapped

- C5 = C4
- C6 = C3
- C7 = C2
- C8 = C1

Figure A.5: Common device specification from the provided fibre-coupled converters. This picture is kindly provided by Carsten Langrock from the group of Martin Feyrer from Stanford University

## A.4 TEMPERATURE STABILIZATION OF NONLINEAR CRYSTALS

This section describes how the temperature stabilization was done for the nonlinear crystals used in this thesis. The basic idea stays the same for all different conversion crystals used. For heating and cooling of the crystals, Peltier-elements are used which are driven by a PID-controller, built and designed in-house by the electronic workshop at IQOQI Innsbruck. This rack-mounted PID-controller is specialized for temperature stabilization and provides currents up to 2 A. A feedback loop measures the temperature of the crystal via a Wheatstone bridge, consisting of two temperature sensitive resistors (NTC 10k 697-4572) and a variable resistor for setting the target temperature. The difference between the actual temperature and the set temperature results into a voltage offset from 0 on the Wheatstone bridge. This voltage is fed back to the PID-controller. The PID controller adjusts the current such that the actual temperature equals the set temperature. For one of the NTT-crystals (ridge waveguides) a commercial PID temperature controller is used (Thorlabs, TED200C), but the principle of the setup and the feedback loop stays the same.

The ovens for the all crystals were designed by me and fabricated in the in-house mechanical workshop. The two main features of this oven system are to bring the crystal into the optical path and to stabilise the crystal temperature. For the free space NTT crystals we chose a beam height of 100 mm from the optical table. The oven was built such that the waveguides of the crystals are at this beam height. Also we wanted to use the translation stage from Elliot Scientific, since the group of Hugues de Ridmatten and the group of Gregor Weihs use them successfully. As shown in Figure A.6, the XYZ-translation stages from Elliot Scientific are placed on distance plates to achieve a final beam height of 100 mm. The crystal oven is mounted on an aluminium block, which acts as a heat sink, and has a lid to prevent the crystal from ambient air flow in the lab. The lid also protects the crystal from dust.

The temperature stabilization oven system for the fibre-coupled conversion crystals from Stanford is similar to the one for the NTT crystals and is shown in Figure A.7. The Stanford devices are delivered without any mounting system, therefore also the crystal holder was designed by me and fabricated in the in-house mechanical workshop. The crystal is placed into our holder and fixed with a lid. The holder is then mounted on a Peltier element, which again is mounted on an aluminium block, which acts also as the heat sink. An additional cover (not shown in the figure) is placed on the mount over the whole crystal system to protect it from airflow and dust.

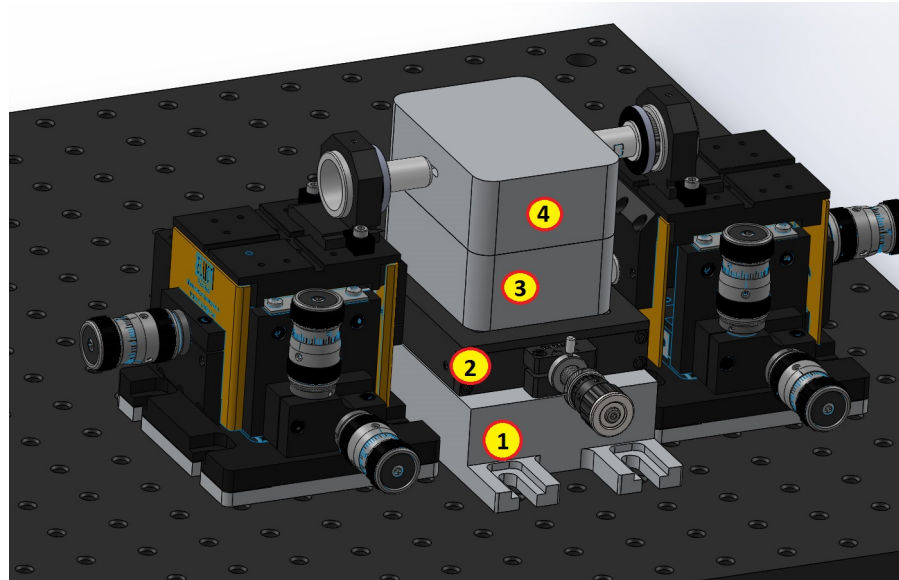


Figure A.6: **Temperature stabilisation and alignment stage constructed for our NTT ridge-waveguide crystals:** The aluminium base-mount (1) is screwed on the optical table. On the mount a translation stage (2) enables changing between the single waveguides of the crystal. The second mount (3) connects the translation stage with the waveguide holder (not visible in this figure) and lifts the system to the correct optical height. The delivered NTT-crystals are already connected to a peltier element and a small holder. This holder is screwed on the second mount (3). A lid (4) prevents dust and air flow changing the system. This tower is placed between to xyz- translation stages (Elliot Scientific Ltd, MDE 122) with mounted lenses to couple light in and out of the waveguides.

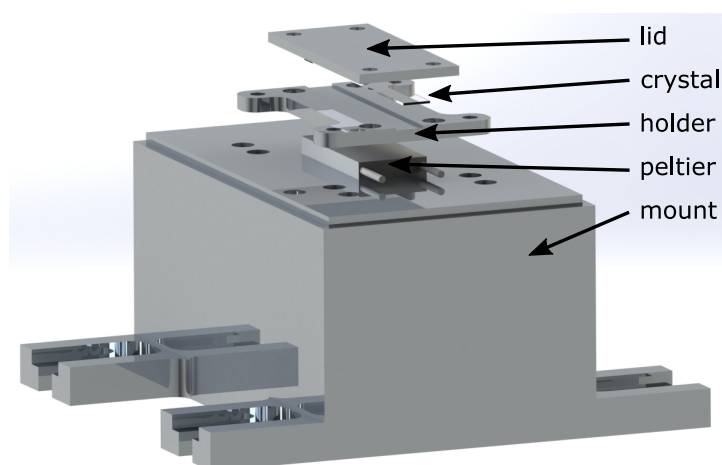


Figure A.7: **Temperature stabilisation oven and assembly for the fibre-coupled waveguide crystals from Stanford:** The aluminium mount is screwed on the optical table to reach the preferred optical height and also serves as a heat reservoir. Such a heat reservoir allows better temperature control of the crystal when using Peltier-elements. The holder has additionally 4 holes drilled on the side, in which temperature sensors could be glued into it. The lid holds the crystal on the holder. On top of this setup (not shown here) is a cover, to prevent airflow and dust disturbing the system.

### A.5 INDISTINGUISHABILITY OF CONVERTED PHOTONS: DATA ANALYSIS

During the experimental run we record the absolute time stamps of two detector events  $D_1$  and  $D_2$ , and of an electronic trigger pulse generated simultaneously with  $V_1$  at time  $t_1$  in each cycle (see Figure 7.5). We then work in a time frame referenced to the trigger pulse. In this frame the photon arrival times are grouped into three time windows: the first group contains the overlapped synchronous photons (generated by  $V_1$  and  $H_1$ ), the second group contains the first of the time-displaced ‘asynchronous’ photons ( $V_2$ , through the delay line) and the third group contains the later asynchronous photon ( $H_2$ , direct path). In the Figure 7.6a we sum up the data for two detectors and plot separately the probabilities of events corresponding to (windows containing)  $V_2$  and  $H_2$ . This is done by shifting the distributions in time by a fixed offset  $t$  ( $t + t_{wait}$ ) for  $V_2$  ( $H_2$ ), with  $t$  being the delay between the trigger pulse and the expected  $V_2$ -photons’ front-slope;  $t_{wait}$  is the known additional wait time  $t_{wait} = 30 \mu\text{s}$ . We plot the detection-probability-density, defined as the number of events detected in a certain time bin during the experiment divided by the number of trials and bin duration. The error bars represent  $\pm 1$  standard deviation of Poissonian photon counting statistics.

To plot the coincidence distribution (Figures 7.6b and 7.7b) we first choose a time window (software gate) where the corresponding photons are expected to arrive based on sequence timing and the histogram of all recorded events. Then we calculate the probability density  $\rho_c(D_1(t_1), D_2(t_2))$  of observing a two-photon detection event in a given trial as a function of the detections time difference  $\tau = t_2 - t_1$ . The plotted values in the figure are calculated as  $\rho_c(\tau) = \frac{1}{\Delta_t k} \int_{gate} dt_1 \int_{t_1+\tau}^{t_1+\tau+\Delta_t} dt_2 N(t_1, t_2)$  where  $N(t_1, t_2)$  is the number of two-photon clicks with given times,  $\Delta_t$  is the bin size in the figure and  $k$  is the total number of attempts. The errorbars for each point in the figure are calculated from the total number of events detected for this bin assuming Poissonian statistics. The coincidence distribution for the distinguishable photons (from  $V_2, H_2$ ), originally peaking at the  $\tau = \pm t_{wait}$ , is shifted to  $\tau = 0$  and summed over positive and negative branches to represent the expected coincidence distribution for the fully distinguishable but synchronized photons.

Given the distribution of coincidences in time we define the visibility (plotted in Figures 7.6c and 7.7c as:

$$V(T) = \frac{C^\perp(T) - C^\parallel(T)}{C^\perp(T)}, \quad (\text{A.1})$$

where  $C^\perp(T)$  ( $C^\parallel(T)$ ) are the coincidence probabilities for the distinguishable (overlapped) pair of photons plotted in Figures 7.6b and

7.7b integrated over the delay range  $\tau \in [-T; T]$ :  $C(T) = \int_{-T}^T \rho_c(\tau) d\tau$ .

For the passive delay-line experiment (without conversion) we perform in total 7.5 million cycles, where each cycle corresponds to one loop (cycle) in Figure 7.5 (attempt to generate four photons). The experiment with frequency conversion consists of a total of 2.5 million cycles.



## BIBLIOGRAPHY

---

- [1] S. Fischer. *A history of language*. London: Reaktion, 1999. ISBN: 9781861890801.
- [2] Aischylos. *Die Orestie*. Hofenberg, May 2016. 132 pp. ISBN: 3843050864.
- [3] H. J. Kimble. “The quantum internet.” In: *Nature* 453.7198 (2008), pp. 1023–1030. DOI: [10.1038/nature07127](https://doi.org/10.1038/nature07127).
- [4] P. Zoller et al. “Quantum information processing and communication.” In: *The European Physical Journal D* 36.2 (2005), pp. 203–228. DOI: [10.1140/epjd/e2005-00251-1](https://doi.org/10.1140/epjd/e2005-00251-1).
- [5] D. Bouwmeester, A. Ekert, and A. Zeilinger, eds. *The Physics of Quantum Information*. Springer Berlin Heidelberg, 2000. DOI: [10.1007/978-3-662-04209-0](https://doi.org/10.1007/978-3-662-04209-0).
- [6] S. Wehner, D. Elkouss, and R. Hanson. “Quantum internet: A vision for the road ahead.” In: *Science* 362.6412 (2018). DOI: [10.1126/science.aam9288](https://doi.org/10.1126/science.aam9288).
- [7] C. Monroe, R. Raussendorf, A. Ruthven, K. R. Brown, P. Maunz, L.-M. Duan, and J. Kim. “Large-scale modular quantum-computer architecture with atomic memory and photonic interconnects.” In: *Physical Review A* 89.2 (2014), p. 022317. DOI: [10.1103/physreva.89.022317](https://doi.org/10.1103/physreva.89.022317).
- [8] P. Kómár, E. M. Kessler, M. Bishof, L. Jiang, A. S. Sørensen, J. Ye, and M. D. Lukin. “A quantum network of clocks.” In: *Nature Physics* 10.8 (2014), pp. 582–587. DOI: [10.1038/nphys3000](https://doi.org/10.1038/nphys3000).
- [9] S. Ritter, C. Nölleke, C. Hahn, A. Reiserer, A. Neuzner, M. Uphoff, M. Mücke, E. Figueroa, J. Bochmann, and G. Rempe. “An elementary quantum network of single atoms in optical cavities.” In: *Nature* 484.7393 (2012), pp. 195–200. DOI: [10.1038/nature11023](https://doi.org/10.1038/nature11023).
- [10] D. L. Moehring, P. Maunz, S. Olmschenk, K. C. Younge, D. N. Matsukevich, L.-M. Duan, and C. Monroe. “Entanglement of single-atom quantum bits at a distance.” In: *Nature* 449.7158 (2007), pp. 68–71. DOI: [10.1038/nature06118](https://doi.org/10.1038/nature06118).
- [11] B. Hensen et al. “Loophole-free Bell inequality violation using electron spins separated by 1.3 kilometres.” In: *Nature* 526.7575 (2015), pp. 682–686. DOI: [10.1038/nature15759](https://doi.org/10.1038/nature15759).
- [12] M. Pompili et al. “Realization of a multinode quantum network of remote solid-state qubits.” In: *Science* 372.6539 (2021), pp. 259–264. DOI: [10.1126/science.abg1919](https://doi.org/10.1126/science.abg1919).

- [13] S.-K. Liao et al. "Satellite-Relayed Intercontinental Quantum Network." In: *Physical Review Letters* 120.3 (2018), p. 030501. DOI: [10.1103/physrevlett.120.030501](https://doi.org/10.1103/physrevlett.120.030501).
- [14] A. Wallucks, I. Marinković, B. Hensen, R. Stockill, and S. Gröblacher. "A quantum memory at telecom wavelengths." In: *Nature Physics* 16.7 (2020), pp. 772–777. DOI: [10.1038/s41567-020-0891-z](https://doi.org/10.1038/s41567-020-0891-z).
- [15] P. A. Franken, A. E. Hill, C. W. Peters, and G. Weinreich. "Generation of Optical Harmonics." In: *Physical Review Letters* 7.4 (1961), pp. 118–119. DOI: [10.1103/physrevlett.7.118](https://doi.org/10.1103/physrevlett.7.118).
- [16] S. Zaske et al. "Visible-to-Telecom Quantum Frequency Conversion of Light from a Single Quantum Emitter." In: *Phys. Rev. Lett.* 109 (14 2012), p. 147404. DOI: [10.1103/PhysRevLett.109.147404](https://doi.org/10.1103/PhysRevLett.109.147404).
- [17] V. Krutyanskiy, M. Meraner, J. Schupp, and B. P. Lanyon. "Polarisation-preserving photon frequency conversion from a trapped-ion-compatible wavelength to the telecom C-band." In: *Applied Physics B* 123.9 (2017), p. 228. DOI: [10.1007/s00340-017-6806-8](https://doi.org/10.1007/s00340-017-6806-8).
- [18] M. Bock, P. Eich, S. Kucera, M. Kreis, A. Lenhard, C. Becher, and J. Eschner. "High-fidelity entanglement between a trapped ion and a telecom photon via quantum frequency conversion." In: *Nature Communications* 9.1 (2018). DOI: [10.1038/s41467-018-04341-2](https://doi.org/10.1038/s41467-018-04341-2).
- [19] J. Hannegan, J. Siverns, and Q. Quraishi. "Quantum Frequency Conversion of Ba<sup>+</sup> Photons." In: *Frontiers in Optics / Laser Science*. Optical Society of America, 2018, JW3A.60. DOI: [10.1364/FIO.2018.JW3A.60](https://doi.org/10.1364/FIO.2018.JW3A.60).
- [20] T. van Leent, M. Bock, R. Garthoff, K. Redeker, W. Zhang, T. Bauer, W. Rosenfeld, C. Becher, and H. Weinfurter. "Long-Distance Distribution of Atom-Photon Entanglement at Telecom Wavelength." In: *Physical Review Letters* 124.1 (2020), pp. – 010510. DOI: [10.1103/physrevlett.124.010510](https://doi.org/10.1103/physrevlett.124.010510).
- [21] A. Craddock, J. Hannegan, D. Ornelas-Huerta, J. Siverns, A. Hachtel, E. Goldschmidt, J. Porto, Q. Quraishi, and S. Rolston. "Quantum Interference between Photons from an Atomic Ensemble and a Remote Atomic Ion." In: *Physical Review Letters* 123.21 (2019), p. 213601. DOI: [10.1103/physrevlett.123.213601](https://doi.org/10.1103/physrevlett.123.213601).
- [22] P. Schindler, J. T. Barreiro, T. Monz, V. Nebendahl, D. Nigg, M. Chwalla, M. Hennrich, and R. Blatt. "Experimental Repetitive Quantum Error Correction." In: *Science* 332.6033 (2011), pp. 1059–1061. DOI: [10.1126/science.1203329](https://doi.org/10.1126/science.1203329).

- [23] N. M. Linke, M. Gutierrez, K. A. Landsman, C. Figgatt, S. Debnath, K. R. Brown, and C. Monroe. “Fault-tolerant quantum error detection.” In: *Science Advances* 3.10 (2017). DOI: [10.1126/sciadv.1701074](https://doi.org/10.1126/sciadv.1701074).
- [24] J. Benhelm, G. Kirchmair, C. F. Roos, and R. Blatt. “Towards fault-tolerant quantum computing with trapped ions.” In: *Nature Physics* 4.6 (2008), pp. 463–466. DOI: [10.1038/nphys961](https://doi.org/10.1038/nphys961).
- [25] H.-J. Briegel, W. Dür, J. I. Cirac, and P. Zoller. “Quantum Repeaters: The Role of Imperfect Local Operations in Quantum Communication.” In: *Phys. Rev. Lett.* 81 (26 1998), pp. 5932–5935. DOI: [10.1103/PhysRevLett.81.5932](https://doi.org/10.1103/PhysRevLett.81.5932).
- [26] N. Sangouard, R. Dubessy, and C. Simon. “Quantum repeaters based on single trapped ions.” In: *Phys. Rev. A* 79 (4 2009), p. 042340. DOI: [10.1103/PhysRevA.79.042340](https://doi.org/10.1103/PhysRevA.79.042340).
- [27] S. Olmschenk, D. N. Matsukevich, P. Maunz, D. Hayes, L.-M. Duan, and C. Monroe. “Quantum Teleportation Between Distant Matter Qubits.” In: *Science* 323.5913 (2009), pp. 486–489. DOI: [10.1126/science.1167209](https://doi.org/10.1126/science.1167209).
- [28] D. Hucul, I. V. Inlek, G. Vittorini, C. Crocker, S. Debnath, S. M. Clark, and C. Monroe. “Modular entanglement of atomic qubits using photons and phonons.” In: *Nature Physics* 11.1 (2015), pp. 37–42. DOI: [10.1038/nphys3150](https://doi.org/10.1038/nphys3150).
- [29] E. O. Ilo-Okeke, L. Tessler, J. P. Dowling, and T. Byrnes. “Remote quantum clock synchronization without synchronized clocks.” In: *npj Quantum Information* 4.1 (2018). DOI: [10.1038/s41534-018-0090-2](https://doi.org/10.1038/s41534-018-0090-2).
- [30] L. Slodička, G. Hétet, N. Röck, P. Schindler, M. Hennrich, and R. Blatt. “Atom-Atom Entanglement by Single-Photon Detection.” In: *Physical Review Letters* 110.8 (2013), p. 083603. DOI: [10.1103/physrevlett.110.083603](https://doi.org/10.1103/physrevlett.110.083603).
- [31] A. Stute, B. Casabone, P. Schindler, T. Monz, P. O. Schmidt, B. Brandstätter, T. E. Northup, and R. Blatt. “Tunable ion–photon entanglement in an optical cavity.” In: *Nature* 485.7399 (2012), pp. 482–485. DOI: [10.1038/nature11120](https://doi.org/10.1038/nature11120).
- [32] M. A. Nielsen and I. L. Chuang. *Quantum Computation and Quantum Information*. Cambridge University Press, 2000. ISBN: 521635039.
- [33] T. D. Ladd, F. Jelezko, R. Laflamme, Y. Nakamura, C. Monroe, and J. L. O’Brien. “Quantum computers.” In: *Nature* 464.7285 (2010), pp. 45–53. DOI: [10.1038/nature08812](https://doi.org/10.1038/nature08812).
- [34] C. Monroe and J. Kim. “Scaling the Ion Trap Quantum Processor.” In: *Science* 339.6124 (2013), pp. 1164–1169. DOI: [10.1126/science.1231298](https://doi.org/10.1126/science.1231298).

- [35] P. Schindler et al. "A quantum information processor with trapped ions." In: *New Journal of Physics* 15.12 (2013), p. 123012. DOI: [10.1088/1367-2630/15/12/123012](https://doi.org/10.1088/1367-2630/15/12/123012).
- [36] J. L. O'Brien. "Optical Quantum Computing." In: *Science* - 318.5856 (2007), pp. 1567–1570. DOI: [10.1126/science.1142892](https://doi.org/10.1126/science.1142892).
- [37] S. Hill and W. K. Wootters. "Entanglement of a Pair of Quantum Bits." In: 78.26 (1997), pp. 5022–5025. DOI: [10.1103/physrevlett.78.5022](https://doi.org/10.1103/physrevlett.78.5022).
- [38] W. K. Wootters. "Entanglement of Formation of an Arbitrary State of Two Qubits." In: *Phys. Rev. Lett.* 80.10 (10 1998), pp. 2245–2248. DOI: [10.1103/physrevlett.80.2245](https://doi.org/10.1103/physrevlett.80.2245).
- [39] I. L. C. Michael A. Nielsen. *Quantum Computation and Quantum Information*. Cambridge University Pr., Dec. 2010. ISBN: 1107002176.
- [40] D. F. V. James, P. G. Kwiat, W. J. Munro, and A. G. White. "Measurement of qubits." In: *Physical Review A* 64.5 (2001), p. 052312. DOI: [10.1103/physreva.64.052312](https://doi.org/10.1103/physreva.64.052312).
- [41] V. Krutyanskiy\*, M. Meraner\*, J. Schupp\*, V. Krčmaršky, H. Hainzer, and B. P. Lanyon. "Light-matter entanglement over 50 km of optical fibre." In: *npj Quantum Information* 5.1 (2019), p. 72. DOI: [10.1038/s41534-019-0186-3](https://doi.org/10.1038/s41534-019-0186-3).
- [42] H. Dehmelt. "Proposed  $10^{14} \Delta\nu < \nu$  Laser Fluorescence Spectroscopy on TI + Mono-Ion Oscillator." In: *Bulletin of the American Physical Society* 20 (1975).
- [43] T. Monz. "Quantum information processing beyond ten ion-qubits." PhD thesis. University of Innsbruck, Aug. 2011.
- [44] W. Kozlovsky, C. Nabors, and R. Byer. "Efficient second harmonic generation of a diode-laser-pumped CW Nd:YAG laser using monolithic MgO:LiNbO<sub>3</sub>/sub 3/ external resonant cavities." In: *IEEE Journal of Quantum Electronics* 24.6 (1988), pp. 913–919. DOI: [10.1109/3.211](https://doi.org/10.1109/3.211).
- [45] L. Ma, J. C. Bienfang, O. Slattery, and X. Tang. "Up-conversion single-photon detector using multi-wavelength sampling techniques." In: *Optics Express* 19.6 (2011), p. 5470. DOI: [10.1364/oe.19.005470](https://doi.org/10.1364/oe.19.005470).
- [46] P. Kumar. "Quantum frequency conversion." In: *Opt. Lett.* 15.24 (1990), pp. 1476–1478. DOI: [10.1364/OL.15.001476](https://doi.org/10.1364/OL.15.001476).
- [47] J. Huang and P. Kumar. "Observation of quantum frequency conversion." In: *Phys. Rev. Lett.* 68 (14 1992), pp. 2153–2156. DOI: [10.1103/PhysRevLett.68.2153](https://doi.org/10.1103/PhysRevLett.68.2153).
- [48] R. Boyd. *Nonlinear optics*. Amsterdam Boston: Academic Press, 2008. ISBN: 9780123694706.

- [49] R. Sutherland. *Handbook of nonlinear optics*. New York: Marcel Dekker, 2003. ISBN: 0824742435.
- [50] F Träger. *Springer handbook of lasers and optics*. New York: Springer, 2007. ISBN: 9780387304205.
- [51] Y. R. Shen. *Principles of Nonlinear Optics*. Wiley-Interscience, Nov. 2002. 576 pp. ISBN: 0471430803.
- [52] A. Lenhard. “Quantum Photonic Interfaces between Atomic and Telecommunication Wavelengths.” PhD thesis. Universität des Saarlandes, 2015.
- [53] R. V. Roussev, C. Langrock, J. R. Kurz, and M. M. Fejer. “Periodically poled lithium niobate waveguide sum-frequency generator for efficient single-photon detection at communication wavelengths.” In: *Optics Letters* 29.13 (2004), p. 1518. DOI: [10.1364/ol.29.001518](https://doi.org/10.1364/ol.29.001518).
- [54] B. Saleh. *Fundamentals of photonics*. New York: Wiley, 1991. ISBN: 9780471839651.
- [55] A. Christ, A. Fedrizzi, H. Hübel, T. Jennewein, and C. Silberhorn. “Parametric Down-Conversion.” In: *Experimental Methods in the Physical Sciences*. Elsevier, 2013. Chap. 11, pp. 351–410. DOI: [10.1016/b978-0-12-387695-9.00011-1](https://doi.org/10.1016/b978-0-12-387695-9.00011-1).
- [56] D. C. Burnham and D. L. Weinberg. “Observation of Simultaneity in Parametric Production of Optical Photon Pairs.” In: *Physical Review Letters* 25.2 (1970), pp. 84–87. DOI: [10.1103/physrevlett.25.84](https://doi.org/10.1103/physrevlett.25.84).
- [57] P. G. Kwiat, K. Mattle, H. Weinfurter, A. Zeilinger, A. V. Sergienko, and Y. Shih. “New High-Intensity Source of Polarization-Entangled Photon Pairs.” In: *Physical Review Letters* 75.24 (1995), pp. 4337–4341. DOI: [10.1103/physrevlett.75.4337](https://doi.org/10.1103/physrevlett.75.4337).
- [58] J. S. Pelc, C. R. Phillips, D. Chang, C. Langrock, and M. M. Fejer. “Efficiency pedestal in quasi-phase-matching devices with random duty-cycle errors.” In: *Optics Letters* 36.6 (2011), p. 864. DOI: [10.1364/ol.36.000864](https://doi.org/10.1364/ol.36.000864).
- [59] R. Loudon. “The Raman effect in crystals.” In: *Advances in Physics* 50.7 (2001), pp. 813–864. DOI: [10.1080/00018730110101395](https://doi.org/10.1080/00018730110101395).
- [60] J. S. Pelc, L Ma, C. R. Phillips, Q Zhang, C Langrock, O Slattery, X Tang, and M. M. Fejer. “Long-wavelength-pumped upconversion single-photon detector at 1550 nm: performance and noise analysis.” In: *Opt. Express* 19.22 (2011), pp. 21445–21456. DOI: [10.1364/OE.19.021445](https://doi.org/10.1364/OE.19.021445).

- [61] H. Kamada, M. Asobe, T. Honjo, H. Takesue, Y. Tokura, Y. Nishida, O. Tadanaga, and H. Miyazawa. "Efficient and low-noise single-photon detection in 1550 nm communication band by frequency upconversion in periodically poled LiNbO<sub>3</sub> waveguides." In: *Optics Letters* 33.7 (2008), p. 639. DOI: [10.1364/ol.33.000639](https://doi.org/10.1364/ol.33.000639).
- [62] M. Malyj and J. E. Griffiths. "Stokes/Anti-Stokes Raman Vibrational Temperatures: Reference Materials, Standard Lamps, and Spectrophotometric Calibrations." In: *Applied Spectroscopy* 37.4 (1983), pp. 315–333. DOI: [10.1366/0003702834634325](https://doi.org/10.1366/0003702834634325).
- [63] R. Ikuta, Y. Kusaka, T. Kitano, H. Kato, T. Yamamoto, M. Koashi, and N. Imoto. "Wide-band quantum interface for visible-to-telecommunication wavelength conversion." In: *Nature Communications* 2.1 (2011). DOI: [10.1038/ncomms1544](https://doi.org/10.1038/ncomms1544).
- [64] T. Monz, P. Schindler, J. T. Barreiro, M. Chwalla, D. Nigg, W. A. Coish, M. Harlander, W. Hänsel, M. Hennrich, and R. Blatt. "14-Qubit Entanglement: Creation and Coherence." In: *Phys. Rev. Lett.* 106.13 (2011), p. 130506. DOI: [10.1103/PhysRevLett.106.130506](https://doi.org/10.1103/PhysRevLett.106.130506).
- [65] D. Nigg, M. Müller, E. A. Martinez, P. Schindler, M. Hennrich, T. Monz, M. A. Martin-Delgado, and R. Blatt. "Quantum computations on a topologically encoded qubit." In: *Science* 345.6194 (2014), pp. 302–305. DOI: [10.1126/science.1253742](https://doi.org/10.1126/science.1253742).
- [66] J. T. Barreiro, M. Müller, P. Schindler, D. Nigg, T. Monz, M. Chwalla, M. Hennrich, C. F. Roos, P. Zoller, and R. Blatt. "An open-system quantum simulator with trapped ions." In: *Nature* 470.7335 (2011), pp. 486–491. DOI: [10.1038/nature09801](https://doi.org/10.1038/nature09801).
- [67] M. Schug, J. Huwer, C. Kurz, P. Müller, and J. Eschner. "Heralded Photonic Interaction between Distant Single Ions." In: 110.21 (2013), p. 213603. DOI: [10.1103/physrevlett.110.213603](https://doi.org/10.1103/physrevlett.110.213603).
- [68] P. Fisher, R. Cernansky, B. Haylock, and M. Lobino. "Single Photon Frequency Conversion for Frequency Multiplexed Quantum Networks in the Telecom Band." In: 127.2 (2021), p. 023602. DOI: [10.1103/physrevlett.127.023602](https://doi.org/10.1103/physrevlett.127.023602).
- [69] J. Schupp. "Light-matter interface for a quantum network with trapped ions." PhD thesis. University of Innsbruck, 2022.
- [70] V. Krcmarsky. "Towards a Trapped-Ion Quantum Network over 500 m." PhD thesis. University of Innsbruck, 2022, not published.

- [71] J. Schupp, V. Krcmarsky, V. Krutyanskiy, **M. Meraner**, T. E. Northup, and B. Lanyon. “Interface between Trapped-Ion Qubits and Traveling Photons with Close-to-Optimal Efficiency.” In: *PRX Quantum* 2 (2 2021), p. 020331. DOI: [10.1103/PRXQuantum.2.020331](https://doi.org/10.1103/PRXQuantum.2.020331).
- [72] A. Siegman. *Lasers*. University Science Books, 1986. ISBN: 978-0935702118.
- [73] C. J. Hood, H. J. Kimble, and J. Ye. “Characterization of high-finesse mirrors: Loss, phase shifts, and mode structure in an optical cavity.” In: *Phys. Rev. A* 64 (3 2001), p. 033804. DOI: [10.1103/PhysRevA.64.033804](https://doi.org/10.1103/PhysRevA.64.033804).
- [74] E. D. Black. “An introduction to Pound-Drever-Hall laser frequency stabilization.” In: *American Journal of Physics* 69.1 (2001), pp. 79–87. DOI: [10.1119/1.1286663](https://doi.org/10.1119/1.1286663).
- [75] H. Hainzer. “Laser Locking For Trapped-Ion Quantum Networks.” MA thesis. University of Innsbruck, 2018.
- [76] A. J. Fleisher, D. A. Long, Q. Liu, and J. T. Hodges. “Precision interferometric measurements of mirror birefringence in high-finesse optical resonators.” In: *Physical Review A* 93.1 (2016), p. 013833. DOI: [10.1103/physreva.93.013833](https://doi.org/10.1103/physreva.93.013833).
- [77] A. Stute. “A light-matter quantum interface: ion-photon entanglement and state mapping.” PhD thesis. University of Innsbruck, 2013.
- [78] M. Keller, B. Lange, K. Hayasaka, W. Lange, and H. Walther. “Continuous generation of single photons with controlled waveform in an ion-trap cavity system.” In: *Nature* 431.7012 (2004), pp. 1075–1078. DOI: [10.1038/nature02961](https://doi.org/10.1038/nature02961).
- [79] H. G. Barros, A. Stute, T. E. Northup, C. Russo, P. O. Schmidt, and R. Blatt. “Deterministic single-photon source from a single ion.” In: *New Journal of Physics* 11.10 (2009), p. 103004. DOI: [10.1088/1367-2630/11/10/103004](https://doi.org/10.1088/1367-2630/11/10/103004).
- [80] J. Jin and D. A. Church. “Precision lifetimes for the  $\text{Ca}^+$   $4p$   $^2P$  levels: Experiment challenges theory at the 1% level.” In: *Physical Review Letters* 70.21 (1993), pp. 3213–3216. DOI: [10.1103/physrevlett.70.3213](https://doi.org/10.1103/physrevlett.70.3213).
- [81] N. Gisin, G. Ribordy, W. Tittel, and H. Zbinden. “Quantum cryptography.” In: *Rev. Mod. Phys.* 74 (1 2002), pp. 145–195. DOI: [10.1103/RevModPhys.74.145](https://doi.org/10.1103/RevModPhys.74.145).
- [82] J. A. D. T. J. Proctor P. A. Knott. “Networked quantum sensing.” In: *arXiv:1702.04271* (2017).
- [83] L.-M. Duan and C. Monroe. “Colloquium: Quantum networks with trapped ions.” In: *Rev. Mod. Phys.* 82 (2 2010), pp. 1209–1224. DOI: [10.1103/RevModPhys.82.1209](https://doi.org/10.1103/RevModPhys.82.1209).

- [84] E. Waks and C. Monroe. "Protocol for hybrid entanglement between a trapped atom and a quantum dot." In: *Phys. Rev. A* 80 (6 2009), p. 062330. DOI: [10.1103/PhysRevA.80.062330](https://doi.org/10.1103/PhysRevA.80.062330).
- [85] G. Kurizki, P. Bertet, Y. Kubo, K. Mølmer, D. Petrosyan, P. Rabl, and J. Schmiedmayer. "Quantum technologies with hybrid systems." In: *Proceedings of the National Academy of Sciences* 112.13 (2015), pp. 3866–3873. DOI: [10.1073/pnas.1419326112](https://doi.org/10.1073/pnas.1419326112).
- [86] G. Vittorini, D. Hucul, I. V. Inlek, C. Crocker, and C. Monroe. "Entanglement of distinguishable quantum memories." In: *Phys. Rev. A* 90 (4 2014), p. 040302. DOI: [10.1103/PhysRevA.90.040302](https://doi.org/10.1103/PhysRevA.90.040302).
- [87] S. Tanzilli, W. Tittel, M. Halder, O. Alibart, P. Baldi, N. Gisin, and H. Zbinden. "A photonic quantum information interface." In: *Nature* 437.7055 (2005), pp. 116–120. DOI: [10.1038/nature04009](https://doi.org/10.1038/nature04009).
- [88] J. Lavoie, J. M. Donohue, L. G. Wright, A. Fedrizzi, and K. J. Resch. "Spectral compression of single photons." In: *Nature Photonics* 7.5 (2013), pp. 363–366. DOI: [10.1038/nphoton.2013.47](https://doi.org/10.1038/nphoton.2013.47).
- [89] S. Clemmen, A. Farsi, S. Ramelow, and A. L. Gaeta. "Ramsey Interference with Single Photons." In: *Phys. Rev. Lett.* 117 (22 2016), p. 223601. DOI: [10.1103/PhysRevLett.117.223601](https://doi.org/10.1103/PhysRevLett.117.223601).
- [90] R. Ikuta et al. "Observation of two output light pulses from a partial wavelength converter preserving phase of an input light at a single-photon level." In: *Opt. Express* 21.23 (2013), pp. 27865–27872. DOI: [10.1364/OE.21.027865](https://doi.org/10.1364/OE.21.027865).
- [91] Z.-Y. Zhou, Y. Li, and B.-S. Shi. "Quantum frequency up-conversion of heralded single photon orbital angular momentum states." In: *Conference on Lasers and Electro-Optics*. OSA, 2016. DOI: [10.1364/cleo\\_at.2016.jtu5a.10](https://doi.org/10.1364/cleo_at.2016.jtu5a.10).
- [92] O. Alibart, V. D'Auria, M. D. Micheli, F. Doutre, F. Kaiser, L. Labonté, T. Lunghi, É. Picholle, and S. Tanzilli. "Quantum photonics at telecom wavelengths based on lithium niobate waveguides." In: *Journal of Optics* 18.10 (2016), p. 104001. DOI: [10.1088/2040-8978/18/10/104001](https://doi.org/10.1088/2040-8978/18/10/104001).
- [93] S. Ramelow, A. Fedrizzi, A. Poppe, N. K. Langford, and A. Zeilinger. "Polarization-entanglement-conserving frequency conversion of photons." In: *Phys. Rev. A* 85 (1 2012), p. 013845. DOI: [10.1103/PhysRevA.85.013845](https://doi.org/10.1103/PhysRevA.85.013845).
- [94] A. Lenhard, J. Brito, M. Bock, C. Becher, and J. Eschner. "Coherence and entanglement preservation of frequency-converted heralded single photons." In: *Opt. Express* 25.10 (2017), pp. 11187–11199. DOI: [10.1364/OE.25.011187](https://doi.org/10.1364/OE.25.011187).

- [95] B. Kambs, J. Kettler, M. Bock, J. N. Becker, C. Arend, A. Lenhard, S. L. Portalupi, M. Jetter, P. Michler, and C. Becher. “Low-noise quantum frequency down-conversion of indistinguishable photons.” In: *Opt. Express* 24.19 (2016), pp. 22250–22260. DOI: [10.1364/OE.24.022250](https://doi.org/10.1364/OE.24.022250).
- [96] J. S. Pelc et al. “Downconversion quantum interface for a single quantum dot spin and 1550-nm single-photon channel.” In: *Optics Express* 20.25 (2012), p. 27510. DOI: [10.1364/oe.20.027510](https://doi.org/10.1364/oe.20.027510).
- [97] L. Yu et al. “Two-photon interference at telecom wavelengths for time-bin-encoded single photons from quantum-dot spin qubits.” In: *Nature Communications* 6.1 (2015). DOI: [10.1038/ncomms9955](https://doi.org/10.1038/ncomms9955).
- [98] B. Albrecht, P. Farrera, X. Fernandez-Gonzalvo, M. Cristiani, and H. de Riedmatten. “A waveguide frequency converter connecting rubidium-based quantum memories to the telecom C-band.” In: *Nature Communications* 5.1 (2014). DOI: [10.1038/ncomms4376](https://doi.org/10.1038/ncomms4376).
- [99] P. Farrera, N. Maring, B. Albrecht, G. Heinze, and H. de Riedmatten. “Nonclassical correlations between a C-band telecom photon and a stored spin-wave.” In: *Optica* 3.9 (2016), pp. 1019–1024. DOI: [10.1364/OPTICA.3.001019](https://doi.org/10.1364/OPTICA.3.001019).
- [100] R. Ikuta, T. Kobayashi, K. Matsuki, S. Miki, T. Yamashita, H. Terai, T. Yamamoto, M. Koashi, T. Mukai, and N. Imoto. “Heralded single excitation of atomic ensemble via solid-state-based telecom photon detection.” In: *Optica* 3.11 (2016), pp. 1279–1284. DOI: [10.1364/OPTICA.3.001279](https://doi.org/10.1364/OPTICA.3.001279).
- [101] N. Maring, K. Kutluer, J. Cohen, M. Cristiani, M. Mazzer, P. M. Ledingham, and H. de Riedmatten. “Storage of up-converted telecom photons in a doped crystal.” In: *New Journal of Physics* 16.11 (2014), p. 113021. DOI: [10.1088/1367-2630/16/11/113021](https://doi.org/10.1088/1367-2630/16/11/113021).
- [102] R. Clark. “Quantum Frequency Conversion for Ytterbium Ion Based Quantum Repeaters.” MA thesis. Duke University, 2012.
- [103] S. Kasture, F. Lenzi, B. Haylock, A. Boes, A. Mitchell, E. W. Streed, and M. Lobino. “Frequency conversion between UV and telecom wavelengths in a lithium niobate waveguide for quantum communication with  $\text{Yb}^+$  trapped ions.” In: *Journal of Optics* 18.10 (2016), p. 104007. DOI: [10.1088/2040-8978/18/10/104007](https://doi.org/10.1088/2040-8978/18/10/104007).
- [104] H. Rütz, K.-H. Luo, H. Suche, and C. Silberhorn. “Quantum Frequency Conversion between Infrared and Ultraviolet.” In: *Phys. Rev. Applied* 7 (2 2017), p. 024021. DOI: [10.1103/PhysRevApplied.7.024021](https://doi.org/10.1103/PhysRevApplied.7.024021).

- [105] D. E. Zelmon, D. L. Small, and D. Jundt. "Infrared corrected Sellmeier coefficients for congruently grown lithium niobate and 5 mol% magnesium oxide-doped lithium niobate." In: *Journal of the Optical Society of America B* 14.12 (1997), p. 3319. DOI: [10.1364/josab.14.003319](https://doi.org/10.1364/josab.14.003319).
- [106] J. S. Pelc, G.-L. Shentu, Q. Zhang, M. M. Fejer, and J.-W. Pan. "Up-conversion of optical signals with multi-longitudinal-mode pump lasers." In: *Phys. Rev. A* 86 (3 2012), p. 033827. DOI: [10.1103/PhysRevA.86.033827](https://doi.org/10.1103/PhysRevA.86.033827).
- [107] M. A. Albota and F. N. C. Wong. "Efficient single-photon counting at 1.55  $\mu\text{m}$  by means of frequency upconversion." In: *Opt. Lett.* 29.13 (2004), pp. 1449–1451. DOI: [10.1364/OL.29.001449](https://doi.org/10.1364/OL.29.001449).
- [108] C. Langrock, E. Diamanti, R. V. Roussev, Y. Yamamoto, M. M. Fejer, and H. Takesue. "Highly efficient single-photon detection at communication wavelengths by use of upconversion in reverse-proton-exchanged periodically poled LiNbO<sub>3</sub> waveguides." In: *Opt. Lett.* 30.13 (2005), pp. 1725–1727. DOI: [10.1364/OL.30.001725](https://doi.org/10.1364/OL.30.001725).
- [109] S. Zaske, A. Lenhard, and C. Becher. "Efficient frequency down-conversion at the single photon level from the red spectral range to the telecommunications C-band." In: *Opt. Express* 19.13 (2011), pp. 12825–12836. DOI: [10.1364/OE.19.012825](https://doi.org/10.1364/OE.19.012825).
- [110] A. Treiber, A. Poppe, M. Hentschel, D. Ferrini, T. Lorünser, E. Querasser, T. Matyus, H. Hübel, and A. Zeilinger. "A fully automated entanglement-based quantum cryptography system for telecom fiber networks." In: *New Journal of Physics* 11.4 (2009), p. 045013. DOI: [10.1088/1367-2630/11/4/045013](https://doi.org/10.1088/1367-2630/11/4/045013).
- [111] A. Stute, B. Casabone, B. Brandstätter, K. Friebe, T. E. Northup, and R. Blatt. "Quantum-state transfer from an ion to a photon." In: *Nature Photonics* 7.3 (2013), pp. 219–222. DOI: [10.1038/nphoton.2012.358](https://doi.org/10.1038/nphoton.2012.358).
- [112] Z. Hradil, J. Summhammer, and H. Rauch. "Quantum tomography as normalization of incompatible observations." In: *Physics Letters A* 261.1-2 (1999), pp. 20–24. DOI: [10.1016/S0375-9601\(99\)00619-2](https://doi.org/10.1016/S0375-9601(99)00619-2).
- [113] G. Vidal and R. F. Werner. "Computable measure of entanglement." In: *Physical Review A* 65.3 (3 2002), p. 032314. DOI: [10.1103/physreva.65.032314](https://doi.org/10.1103/physreva.65.032314).
- [114] K. R. Parameswaran, R. K. Route, J. R. Kurz, R. V. Roussev, M. M. Fejer, and M. Fujimura. "Highly efficient second-harmonic generation in buried waveguides formed by annealed and reverse proton exchange in periodically poled lithium niobate." In: *Optics Letters* 27.3 (2002), p. 179. DOI: [10.1364/ol.27.000179](https://doi.org/10.1364/ol.27.000179).

- [115] N. Maring, P. Farrera, K. Kutluer, M. Mazzera, G. Heinze, and H. de Riedmatten. “Photonic quantum state transfer between a cold atomic gas and a crystal.” In: *Nature* 551.7681 (2017), pp. 485–488. DOI: [10.1038/nature24468](https://doi.org/10.1038/nature24468).
- [116] A. G. Radnaev, Y. O. Dudin, R. Zhao, H. H. Jen, S. D. Jenkins, A. Kuzmich, and T. A. B. Kennedy. “A quantum memory with telecom-wavelength conversion.” In: *Nature Physics* 6.11 (2010), pp. 894–899. DOI: [10.1038/nphys1773](https://doi.org/10.1038/nphys1773).
- [117] A. Dréau, A. Tchebotareva, A. E. Mahdaoui, C. Bonato, and R. Hanson. “Quantum Frequency Conversion of Single Photons from a Nitrogen-Vacancy Center in Diamond to Telecommunication Wavelengths.” In: *Phys. Rev. Applied* 9 (6 2018), p. 064031. DOI: [10.1103/PhysRevApplied.9.064031](https://doi.org/10.1103/PhysRevApplied.9.064031).
- [118] T. Walker, K. Miyanishi, R. Ikuta, H. Takahashi, S. V. Kashanian, Y. Tsujimoto, K. Hayasaka, T. Yamamoto, N. Imoto, and M. Keller. “Long-Distance Single Photon Transmission from a Trapped Ion via Quantum Frequency Conversion.” In: *Physical Review Letters* 120.20 (2018), p. 203601. DOI: [10.1103/physrevlett.120.203601](https://doi.org/10.1103/physrevlett.120.203601).
- [119] J. D. Siverns, J. Hannegan, and Q. Quraishi. “Neutral-Atom Wavelength-Compatible 780 nm Single Photons from a Trapped Ion via Quantum Frequency Conversion.” In: *Physical Review Applied* 11.1 (2019), p. 014044. DOI: [10.1103/physrevapplied.11.014044](https://doi.org/10.1103/physrevapplied.11.014044).
- [120] L. Luo, D. Hayes, T. A. Manning, D. N. Matsukevich, P. Maunz, S. Olmschenk, J. D. Sterk, and C. Monroe. “Protocols and techniques for a scalable atom-photon quantum network.” In: *Fortschr. Phys.* 57.11-12 (Dec. 2009), pp. 1133–1152. DOI: [10.1002/prop.200900093](https://doi.org/10.1002/prop.200900093).
- [121] C. K. Hong, Z. Y. Ou, and L. Mandel. “Measurement of sub-picosecond time intervals between two photons by interference.” In: *Phys. Rev. Lett.* 59 (18 1987), pp. 2044–2046. DOI: [10.1103/PhysRevLett.59.2044](https://doi.org/10.1103/PhysRevLett.59.2044).
- [122] B. Efron and R. Tibshirani. “Bootstrap Methods for Standard Errors, Confidence Intervals, and Other Measures of Statistical Accuracy.” In: *Statist. Sci.* 1.1 (Feb. 1986), pp. 54–75. DOI: [10.1214/ss/1177013815](https://doi.org/10.1214/ss/1177013815).
- [123] C. Maurer, C. Becher, C. Russo, J. Eschner, and R. Blatt. “A single-photon source based on a single Ca<sup>+</sup> ion.” In: *New Journal of Physics* 6 (2004), pp. 94–94. DOI: [10.1088/1367-2630/6/1/094](https://doi.org/10.1088/1367-2630/6/1/094).
- [124] B. P. Lanyon et al. “Universal Digital Quantum Simulation with Trapped Ions.” In: *Science* 334.6052 (2011), pp. 57–61. DOI: [10.1126/science.1208001](https://doi.org/10.1126/science.1208001).

- [125] Y. Wang, M. Um, J. Zhang, S. An, M. Lyu, J.-N. Zhang, L. M. Duan, D. Yum, and K. Kim. “Single-qubit quantum memory exceeding ten-minute coherence time.” In: *Nature Photonics* 11.10 (2017), pp. 646–650. DOI: [10.1038/s41566-017-0007-1](https://doi.org/10.1038/s41566-017-0007-1).
- [126] G. B. Xavier, N Walenta, G. V. de Faria, G. P. Temporão, N Gisin, H Zbinden, and J. P. von der Weid. “Experimental polarization encoded quantum key distribution over optical fibres with real-time continuous birefringence compensation.” In: *New Journal of Physics* 11.4 (2009), p. 045015. DOI: [10.1088/1367-2630/11/4/045015](https://doi.org/10.1088/1367-2630/11/4/045015).
- [127] R. J. Glauber. “The Quantum Theory of Optical Coherence.” In: *Physical Review* 130.6 (1963), pp. 2529–2539. DOI: [10.1103/physrev.130.2529](https://doi.org/10.1103/physrev.130.2529).
- [128] H. J. Kimble, M. Dagenais, and L. Mandel. “Photon Antibunching in Resonance Fluorescence.” In: *Physical Review Letters* 39.11 (1977), pp. 691–695. DOI: [10.1103/physrevlett.39.691](https://doi.org/10.1103/physrevlett.39.691).
- [129] R. H. Brown and R. Twiss. “LXXIV. A new type of interferometer for use in radio astronomy.” In: *The London, Edinburgh, and Dublin Philosophical Magazine and Journal of Science* 45.366 (1954), pp. 663–682. DOI: [10.1080/14786440708520475](https://doi.org/10.1080/14786440708520475).
- [130] B. Brandstätter. “Integration of fiber mirrors and ion traps for a high-fidelity quantum interface.” PhD thesis. University of Innsbruck, 2013.
- [131] T. Walker. “Single Photons from a Trapped-IonCavity-QED System.” PhD thesis. University of Sussex, 2020.
- [132] **M. Meraner\***, A. Mazloom\*, V. Krutyanskiy\*, V. Krcmarsky, J. Schupp, D. A. Fioretto, P. Sekatski, T. E. Northup, N. Sangouard, and B. P. Lanyon. “Indistinguishable photons from a trapped-ion quantum network node.” In: *Phys. Rev. A* 102 (5 2020), p. 052614. DOI: [10.1103/PhysRevA.102.052614](https://doi.org/10.1103/PhysRevA.102.052614).
- [133] L.-M. Duan, M. D. Lukin, J. I. Cirac, and P. Zoller. “Long-distance quantum communication with atomic ensembles and linear optics.” In: *Nature* 414.6862 (2001), pp. 413–418. DOI: [10.1038/35106500](https://doi.org/10.1038/35106500).
- [134] E. T. Khabiboulline, J. Borregaard, K. De Greve, and M. D. Lukin. “Optical Interferometry with Quantum Networks.” In: *Phys. Rev. Lett.* 123 (7 2019), p. 070504. DOI: [10.1103/PhysRevLett.123.070504](https://doi.org/10.1103/PhysRevLett.123.070504).
- [135] P. Sekatski, S. Wölk, and W. Dür. “Optimal distributed sensing in noisy environments.” In: *Physical Review Research* 2.2 (2020), p. 023052. DOI: [10.1103/physrevresearch.2.023052](https://doi.org/10.1103/physrevresearch.2.023052).
- [136] A. Reiserer and G. Rempe. “Cavity-based quantum networks with single atoms and optical photons.” In: *Rev. Mod. Phys.* 87 (4 2015), pp. 1379–1418. DOI: [10.1103/RevModPhys.87.1379](https://doi.org/10.1103/RevModPhys.87.1379).

- [137] C. D. Bruzewicz, J. Chiaverini, R. McConnell, and J. M. Sage. “Trapped-ion quantum computing: Progress and challenges.” In: *Applied Physics Reviews* 6.2 (2019), p. 021314. DOI: [10.1063/1.5088164](https://doi.org/10.1063/1.5088164).
- [138] N. Friis et al. “Observation of Entangled States of a Fully Controlled 20-Qubit System.” In: *Phys. Rev. X* 8 (2 2018), p. 021012. DOI: [10.1103/PhysRevX.8.021012](https://doi.org/10.1103/PhysRevX.8.021012).
- [139] S. M. Brewer, J.-S. Chen, A. M. Hankin, E. R. Clements, C. W. Chou, D. J. Wineland, D. B. Hume, and D. R. Leibbrandt. “ $^{27}\text{Al}^+$  Quantum-Logic Clock with a Systematic Uncertainty below  $10^{-18}$ .” In: *Phys. Rev. Lett.* 123 (3 2019), p. 033201. DOI: [10.1103/PhysRevLett.123.033201](https://doi.org/10.1103/PhysRevLett.123.033201).
- [140] B. B. Blinov, D. L. Moehring, L.-M. Duan, and C. Monroe. “Observation of entanglement between a single trapped atom and a single photon.” In: *Nature* 428.6979 (2004), pp. 153–157. DOI: [10.1038/nature02377](https://doi.org/10.1038/nature02377).
- [141] L. J. Stephenson, D. P. Nadlinger, B. C. Nichol, S. An, P. Drmota, T. G. Ballance, K. Thirumalai, J. F. Goodwin, D. M. Lucas, and C. J. Ballance. “High-Rate, High-Fidelity Entanglement of Qubits Across an Elementary Quantum Network.” In: *Phys. Rev. Lett.* 124 (11 2020), p. 110501. DOI: [10.1103/PhysRevLett.124.110501](https://doi.org/10.1103/PhysRevLett.124.110501).
- [142] K. A. Fischer, K. Müller, K. G. Lagoudakis, and J. Vučković. “Dynamical modeling of pulsed two-photon interference.” In: *New Journal of Physics* 18.11 (2016), p. 113053. DOI: [10.1088/1367-2630/18/11/113053](https://doi.org/10.1088/1367-2630/18/11/113053).
- [143] P. Müller, T. Tentrup, M. Bienert, G. Morigi, and J. Eschner. “Spectral properties of single photons from quantum emitters.” In: *Phys. Rev. A* 96 (2 2017), p. 023861. DOI: [10.1103/PhysRevA.96.023861](https://doi.org/10.1103/PhysRevA.96.023861).
- [144] T. Legero, T. Wilk, M. Hennrich, G. Rempe, and A. Kuhn. “Quantum Beat of Two Single Photons.” In: *Phys. Rev. Lett.* 93 (7 2004), p. 070503. DOI: [10.1103/PhysRevLett.93.070503](https://doi.org/10.1103/PhysRevLett.93.070503).
- [145] T. Wilk, S. C. Webster, H. P. Specht, G. Rempe, and A. Kuhn. “Polarization-Controlled Single Photons.” In: *Phys. Rev. Lett.* 98 (6 2007), p. 063601. DOI: [10.1103/PhysRevLett.98.063601](https://doi.org/10.1103/PhysRevLett.98.063601).
- [146] F. Kaiser, P. Vergyris, A. Martin, D. Aktas, M. P. D. Micheli, O. Alibart, and S. Tanzilli. “Quantum optical frequency up-conversion for polarisation entangled qubits: towards interconnected quantum information devices.” In: *Opt. Express* 27.18 (2019), pp. 25603–25610. DOI: [10.1364/OE.27.025603](https://doi.org/10.1364/OE.27.025603).

- [147] L. Lamata, D. R. Leibbrandt, I. L. Chuang, J. I. Cirac, M. D. Lukin, V. Vuletić, and S. F. Yelin. "Ion Crystal Transducer for Strong Coupling between Single Ions and Single Photons." In: *Phys. Rev. Lett.* 107 (3 2011), p. 030501. DOI: [10.1103/PhysRevLett.107.030501](https://doi.org/10.1103/PhysRevLett.107.030501).
- [148] B. Casabone, K. Friebe, B. Brandstätter, K. Schüppert, R. Blatt, and T. E. Northup. "Enhanced Quantum Interface with Collective Ion-Cavity Coupling." In: *Phys. Rev. Lett.* 114 (2 2015), p. 023602. DOI: [10.1103/PhysRevLett.114.023602](https://doi.org/10.1103/PhysRevLett.114.023602).
- [149] M. Steiner, H. M. Meyer, C. Deutsch, J. Reichel, and M. Köhl. "Single Ion Coupled to an Optical Fiber Cavity." In: *Phys. Rev. Lett.* 110 (4 2013), p. 043003. DOI: [10.1103/PhysRevLett.110.043003](https://doi.org/10.1103/PhysRevLett.110.043003).
- [150] M. Lee, M. Lee, S. Hong, K. Schüppert, Y.-D. Kwon, T. Kim, Y. Colombe, T. E. Northup, D.-I. D. Cho, and R. Blatt. "Microelectromechanical-System-Based Design of a High-Finesse Fiber Cavity Integrated with an Ion Trap." In: *Phys. Rev. Applied* 12 (4 2019), p. 044052. DOI: [10.1103/PhysRevApplied.12.044052](https://doi.org/10.1103/PhysRevApplied.12.044052).
- [151] H. Takahashi, E. Kassa, C. Christoforou, and M. Keller. "Strong Coupling of a Single Ion to an Optical Cavity." In: *Phys. Rev. Lett.* 124 (1 2020), p. 013602. DOI: [10.1103/PhysRevLett.124.013602](https://doi.org/10.1103/PhysRevLett.124.013602).
- [152] Y. T. Chen. "Use of single-mode optical fiber in the stabilization of laser frequency." In: *Applied Optics* 28.11 (1989), p. 2017. DOI: [10.1364/ao.28.002017](https://doi.org/10.1364/ao.28.002017).
- [153] H. Jiang, F. Kéfélian, P. Lemonde, A. Clairon, and G. Santarelli. "An agile laser with ultra-low frequency noise and high sweep linearity." In: *Optics Express* 18.4 (2010), p. 3284. DOI: [10.1364/oe.18.003284](https://doi.org/10.1364/oe.18.003284).
- [154] K Takahashi, M Ando, and K Tsubono. "Stabilization of laser intensity and frequency using optical fiber." In: *Journal of Physics: Conference Series* 122 (2008), p. 012016. DOI: [10.1088/1742-6596/122/1/012016](https://doi.org/10.1088/1742-6596/122/1/012016).
- [155] T. Walker, S. V. Kashanian, T. Ward, and M. Keller. "Improving the indistinguishability of single photons from an ion-cavity system." In: *Physical Review A* 102.3 (2020), p. 032616. DOI: [10.1103/physreva.102.032616](https://doi.org/10.1103/physreva.102.032616).
- [156] K. Mølmer and A. Sørensen. "Multiparticle Entanglement of Hot Trapped Ions." In: *Physical Review Letters* 82.9 (1999), pp. 1835–1838. DOI: [10.1103/physrevlett.82.1835](https://doi.org/10.1103/physrevlett.82.1835).
- [157] M. Canteri. "Single-atom-focused laser for photon generation and qubit control." MA thesis. University of Innsbruck, 2020.

- [158] N. Sangouard, C. Simon, H. de Riedmatten, and N. Gisin. "Quantum repeaters based on atomic ensembles and linear optics." In: *Reviews of Modern Physics* 83.1 (2011), pp. 33–80. DOI: [10.1103/revmodphys.83.33](https://doi.org/10.1103/revmodphys.83.33).
- [159] P. Schindler. "Frequency synthesis and pulse shaping for quantum information processing with trapped ions." Diplomarbeit. University of Innsbruck, 2008.
- [160] D. Heinrich. "Ultrafast coherent excitation of a  $^{40}\text{Ca}^+$  ion." PhD thesis. University of Innsbruck, 2019.



## COLOPHON

This document was typeset using the typographical look-and-feel `classicthesis` developed by André Miede and Ivo Pletikosić. The style was inspired by Robert Bringhurst's seminal book on typography "*The Elements of Typographic Style*". `classicthesis` is available for both  $\LaTeX$  and  $\text{L}\text{\AA}\text{X}$ :

<https://bitbucket.org/amiede/classicthesis/>

*Final Version* as of May 21, 2022 (`classicthesis v4.6`).